CHEMICAL REACTIVITY OF SIZE-SELECTED SUPPORTED CLUSTERS: COMBINED TPD/XPS STUDIES AND APPARATUS DEVELOPMENT

by
Linjie Wang

A dissertation submitted to Johns Hopkins University in conformity with the requirements for the degree of Doctor of Philosophy

Baltimore, Maryland
July 2021

Abstract

There has been a sustained research interest in the unique reactivities of ultra-small metal and metal oxide clusters. Numerous studies have highlighted the capability of the cluster deposition method to explore the catalytic reactivity of ultra-small clusters with different sizes, stoichiometries, and substrates. In this thesis, two beam line coupled surface analytical apparatus are introduced. The newly constructed one is an upgraded version of the previous one with better mass selection capability and improved geometries for combined temperature-programmed desorption (TPD) and X-ray photoelectron spectroscopy (XPS) analysis. Two combined TPD and XPS studies, which were performed on the previous apparatus, are presented, including ligation and decomposition of 1,6-hexanedithiol, and decomposition of dimethyl methylphosphonate (DMMP) by size selected copper and copper oxide clusters. Several crucial troubleshooting processes for the new apparatus are discussed, and some preliminary experimental results are presented.

Acknowledgement

First, I would like to thank my research advisor, Dr. Kit H. Bowen. If it were not for him, I would not have had this opportunity. He was always there guiding me through challenges and obstacles. He always asked me to defend my thoughts, propose plans and anticipate results before I moved forward. He also gave me enough trust in handling some projects on my own. By training in this way for six years, I have become a better scientist who can manage projects with wise decision making.

Next, I want to thank my mentor, Dr. Zachary A. Hicks. If it were not for him, I would never imagine I can be involved in rebuilding a scientific apparatus from zero to completion. Zach has a sharp mind from an engineering perspective, which I was lacking when I first joined this lab. I always learned something new by working with him on a daily basis. At the end, he really guided me through how to understand a complicated apparatus from inside out.

I would also like to thank the other members in our surface machine subgroup. If it were not for them, I would never have had overcome so many challenges. Nicolas Blando is always optimistic and encouraged to get things done. He also has a sharp mind in trouble shooting mechanical and electrical problems. He always fixed things in a fast and efficient way I could never imagine. Michael Denchy is one of the most careful and thoughtful people that I know. He always managed to think outside the box and carried things forward with creative solutions. If it were not for him, some of the obstacles on the new apparatus in the last two years would still have not had been overcome yet. Ben Bilik is very hardworking and has special attention to details. Thanks to a few great catches by him, some problems were spotted at very early stages. Lucas Hansen has a solid background in physical chemistry; I am sure he will make his contributions to some great work on the new apparatus.

I would also like to thank the others I have worked with throughout my time in the Bowen lab. Xin Tang for first introducing the surface apparatus to me. Gaoxiang Liu and Sandy Ciborowski for showing me how the RET apparatus works. Evan Collins, and Xinxing Zhang for showing me how the PIPES apparatus works. Mary Marshall, Zhaoguo Zhu, Moritz Blankenhorn and Rachel Harris for always allowing me to go through their instrument's parts looking for the one part that I needed. They are also always there when I run into any problems with the apparatus.

I would also like to thank my graduate research committee, Dr. Harris Silverstone, and Dr. Howard Fairbrother. I would like to thank Dr. Howard Fairbrother for always offering help on our XPS repairment and allowing us to borrow parts from his lab.

I would also like to thank Dr. Gerd Gantefoer for providing us the original apparatus and for his help on the apparatus construction process.

My undergraduate research adviser Dr. Fengyan Wang, and summer research program advisor, Dr. Samy El-Shall, who showed me there was more to chemistry than glassware and stirred reactors.

My parents for always supporting me.

Table of Contents

List of Table

List of Figures

1. Introduction

1.1 Background

Exploring and understanding the catalytic reactivities of small metal clusters is of great significance not only in academia but also in industry. Small metal clusters, which have high surface to volume ratios and a high percentage of low-coordinated metal atoms on the surface, have unique physical and chemical properties that are distinct from their macroscopic counterparts. No better example is the unique activities of small gold nanoclusters, which are able to catalyze a range of oxidation reactions, whereas bulk gold is inert. Although the origin of the activities of small gold nanoclusters together with the size effects of other metal clusters remain an area of intense experimental and theoretical study, most of the explanations essentially rely on the electronic properties and high density of low coordinated sites, which are unique to very small clusters. These studies have maintained a sustained interest in exploring the unique properties of small metal, as well as metal containing (e.g. metal oxide, metal carbide), clusters for catalytic applications.

In this prospective, it is of great significance that the number of atoms within the deposited clusters is precisely known during the preparation of model supported clusters. Numerous studies have highlighted the ability of the cluster deposition method to explore the reactivity of ultra-small clusters with different sizes, contents, and substrates. Pioneering work on size selected Au_n and Pt_n clusters deposited on a Si(100) wafer by the Exxon group marked the emergence of this cutting-edge research field.[1] From then on, a lot of studies have focused on size-selected noble metals such as Pt_n,[2-5] Pd_n,[6-7] and Au_n,[8-9] and a wide range of catalytic reactions have been investigated such as CO oxidation,[2, 10-14] dehydrogenation,[4, 15] methanol synthesis[16] and so on.

In this work, all the supported clusters sample are made through the cluster deposition method. Depending on the experimental conditions, the reactants are usually introduced into the system through different methods. The reactivities of the as-deposited clusters are analyzed by combined

TPD and XPS measurements. By varying the size and content of the clusters, as well as other experimental conditions, such as dosing amounts, oxygen conditions, and temperatures, reaction mechanism insights can be obtained.

1.2 Experimental

The focus of this section is on the preparation of model supported cluster samples, in which the size, coverage and stoichiometry of deposited clusters are precisely controlled by gas phase cluster ion sources, ion beam transport, mass spectrometry, soft-landing and differential pumping techniques. This approach is especially effective in studying ultra-small clusters in the size range of 2-200 atoms (or < 2 nm), where the physical and electronic structures evolve quickly with increasing sizes. Once a supported size-selected clusters sample has been prepared, various surface sensitive characterization techniques can then be applied.

1.2.1 Cluster Ion Sources

The cluster ion source is one of the most important components of a cluster deposition surface analytical apparatus. It is crucial to have a cluster ion source with great tunability to optimize the clusters ions of interest, along with sufficient ion intensity that can persist for a reasonable time period. Otherwise, the experiments after the deposition can be very hard to carry out consistently. There are three commonly used cluster ion sources namely, magnetron sputtering, laser vaporization and pulsed arc clusters ionization. Magnetron sputtering is the only ion source that has proven to work routinely thus far on the two apparatuses involved in this work. Some efforts have been made to install the other two sources physically into the source chamber, but a lot more work still needs to be done to make them fully functional.

The basic idea of magnetron sputtering is shown in Figure 1.1. Strong electric and magnetic fields are utilized to confine charged plasma particles close to the surface of the sputter target. In a

magnetic field, electrons follow helical paths around magnetic field lines. In this way, gaseous neutrals can undergo more ionizing collisions near the target surface. The sputter gas is typically an inert gas such as argon. Collisions cause an electrostatic repulsion which ‘knock off’ electrons from the sputtering gas atoms, causing ionization. The positive sputter gas atoms can then be accelerated towards the negatively charged cathode, leading to high energy collisions with the surface of the target. As the target material is depleted, a "racetrack" sputtering profile appears on the surface of the target (Figure 1.2).

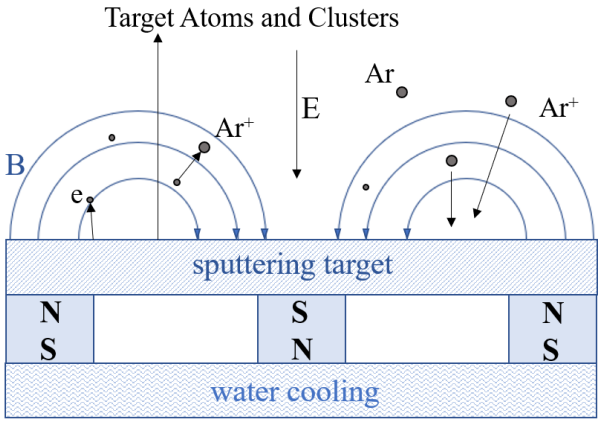

Figure 1.1 Scheme of magnetron sputtering.

Figure 1.2 Tungsten sputtering target with a clear "racetrack" sputtering profile.

1.2.2 Surface Characterization Methods

Temperature-programmed desorption/reaction (TPD/R)

TPD is the method of observing desorbed molecules from a surface when the surface temperature is increased. It is an important method for determination of kinetic and thermodynamic parameters of desorption processes.[17] When surface reactions that occur during the desorption process are the main interest, it is also called TPR.[18]

For a typical TPD/R experiment, the sample is heated with a temperature program $\beta(t) = dT/dt$, in which the temperature T is usually a linear function of the time t. During the temperature ramp, the partial pressures of atoms and molecules evolving from the surface of the sample are measured by mass spectrometry.[19] In surface science studies under UHV conditions, the samples are usually well-defined surfaces of single-crystalline samples[20], thin films[21], clusters[4], or single atoms[22] supported on well-defined surfaces. There is usually a dwell time when the sample is maintained at certain temperatures and reactants are dosed onto the sample. Mass spectrometry in these experiments usually involves a quadrupole mass spectrometer with high sensitivity and high data acquisition speed, often called a residual gas analyzer (RGA). The RGA consists of three components, (1) the ion source, (2) the actual quadrupole analyzer consisting of four cylindrical rods, and (3) the ion detector (electron multiplier). Ions are generated by electron impact ionization. Free electrons are formed by thermal emission from an electrically heated tungsten filament. The emitted electrons are accelerated by a potential difference of 70 V.

Since most organic molecules display complex fragmentation patterns in their electron ionization mass spectra with significant signals for multiple m/e values, it is usually necessary to deconvolute the cracking patterns from the raw TPD data in order to identify the desorption peaks for each product. When studying a new system via TPD, the first thing that needs to be done is to identify the potential products to be followed. This can be done by obtaining survey TPD data with

chemical intuition. The trial experiments on the earlier stage usually provides clues on what products may be forming in the TPD experiments. On one hand, each TPD peak, with its unique shape and position, can represent the desorption of one product or it can be a combination of multiple products. On the other hand, the same species may desorb in more than one temperature regime, and those peaks seen in different traces may also correspond to the same species. Therefore, it is important to compare the peak shape and position of features among the traces of different m/e. If a peak for one m/e can be superimposed to another peak for a different m/e with a scaling factor, it is possible that both peaks correspond to the same species. Comparison of the scaling factors to what have been reported in the literature using the same ionization energy can help identify the nature of that product. The confirmation of a compound usually requires at least two deconvoluted traces to follow each other with a scale factor comparable to what has been reported in the literature.

Once all desorbing products have been identified, a narrower set of m/e values can be chosen to carry out the remaining of the TPD experiments in order to explore the effect of other parameters such as coverage, adsorption temperatures, physi-desorption temperatures and so on. For clusters deposition experiments on highly oriented pyrolytic graphite (HOPG), it is recommended that three background TPD experiments should be done in advance using the same experimental protocol: (a) without reactant or clusters; (b) without reactants but with clusters; (c) without clusters but with reactants. For (a) and (b), there is usually a rising background for common gases such as carbon monoxide, carbon dioxide, oxygen, and water. Sometimes, there may be very weak peaks for reactants or products in (b) experiment, indicating there may be some residual reactant remaining in the UHV system which needs to be removed by bake out, or some other residual contamination species. For (c), one may see physi-desoprtion or chemi-desorption peaks from the substrate and the sample holder, which should coexist with other products' peaks in the TPD experiment with both reactants and clusters.

Once consistent TPD results have been obtained, one can use it as the starting point of a 'story line'. The story line starts with the clusters of interest, the oxidation states, sizes, and stoichiometries of which can be varied in more TPD experiments for parallel story lines. For each cluster, variations in coverage and adsorption temperature, titration of surface species, as well as TPD experiments with probing molecules can be designed to gain more insights about the reaction mechanism. The fact that changes in adsorption temperatures can have great effects on TPD results has been well exemplified by CO oxidation experiments.[10] Titration TPD experiments usually involve introducing another reactant to interact with the speculated surface intermediates before the temperature ramp. The effects that those titration molecules can have on the later on TPD results can help provide more insights about the reaction mechanism. For example, hydrogen atom titration is used to confirm that the rate of bipheny1 evolution above 300 K is determined by the rate of phenyl coupling as opposed to the rate of biphenyl desorption.[23] A similar titration experiment has also been designed to support the proposed reaction mechanism in Chapter 2.[24] Probe molecule TPD is usually used to analyze the surface binding sites or reactive sites. Common probing molecules include carbon monoxide[25], oxygen[26], methanol[27-29], and so on. Additionally, isotopic labeling TPD experiments can also provide valuable insight into reaction pathways when materials are available.[29-30]

X-ray photoelectron spectroscopy (XPS)

XPS is a surface-sensitive quantitative spectroscopic technique based on the photoelectric effect that can identify the elements on the surface of a sample as well as their chemical state. XPS is accomplished by irradiating a sample with monoenergetic soft X-rays and analyzing the kinetic energies and intensity of the detected electrons. Mg Kα (1263.6 eV) or Al Kα (1486.6 eV) X-rays are usually used via a twin anode X-ray source. These photons interact with atoms, causing electrons to be emitted by the photoelectric effect.[31] The emitted electrons have measured kinetic energies given by:

$$E_{kinetic} = E_{photon} - E_{binding} - \phi_s$$

where E_{photon} is the photo energy, $E_{binding}$ is the binding energy of the atomic orbital from which the electron originates, ϕ_s is the spectrometer work funciton.[31] Because each element has a unique set of core electron binding energies, XPS can be used to identify and determine the concentration of the elements on the surface.

XPS is also very useful in analyzing the chemial state of an element since the changes in the chemial bonding of that element can cause changes in binding energy of a core electron of the element, which is also called chemical shift. Chemical shift can be altered by the electrostatic shielding of the nuclear charge from all other electrons in the atom including valence electrons, as well as removal or addition of electronic charges resulting from changes in oxidation states.

For cluster deposition experiments, XPS can be applied to analyze the cleanliness of the substrates, the chemical compositions of the deposited clusters, the physiosorbed reactants, and the chemistry between the clusters and the reactants. XPS can also be applied after the sample is heated to certain temperatures to thermally induce reactions and desorption. Therefore, XPS and TPD can be applied synergetically in clusters deposition and surface analysis studies.

For a new system (size-selected clusters of interest with certain reactants) to be studied, XPS is usually carried out first to verify the composition of the as-deposited clusters. It should be noted that size effects, clusters-support interactions, clusters agglomeration and aggregation mechanism can lead to shifts in binding energies and changes in the shape of spectra.[32-34] Therefore, binding energies and spectra shape reported in the literature for macroscopic samples, which are usually done on single crystals[35-36] or polycrystalline particles[37-38], cannot be directly used for interpretation of the spectra. XPS should also be applied on multilayers of a reactant frozen on the substrate at cryogenic temperature, so that binding energies for molecular form of the reactant can

be obtained for comparison.[39] Once major gaseous reaction products have been identified by TPD experiments, several critical temperatures can be decided to carry out temperature-dependent XPS.

In short, the use of TPD and XPS together is a synergetic combination, providing chemical characterization of reaction products in gas phase as well as on the surface that result from thermally induced reactions between clusters and reactants.

1.2.3 Apparatus Development

This section explains firstly the old apparatus on which all the previous works were done. Then, the new apparatus is introduced briefly, with a focus on the major improvements over the old machine. More importantly, how these improvements can broaden our capabilities to study more supported size-selected clusters is explained.

Previous Beam Line Couple Surface Apparatus

As illustrated schematically in Figure 1.3, the previous apparatus consisted of a magnetron sputtering ion source, several vacuum chambers for differential pumping purposes, a magnetic sector for mass selection, a deposition chamber for sample preparation as well as TPD measurements, and an analysis chamber for in-situ or ex-situ XPS measurements. There was a horizontal transfer arm which could transfer the sample from the load-lock chamber into the deposition chamber, then further into the analysis chamber, and finally into the STM chamber.

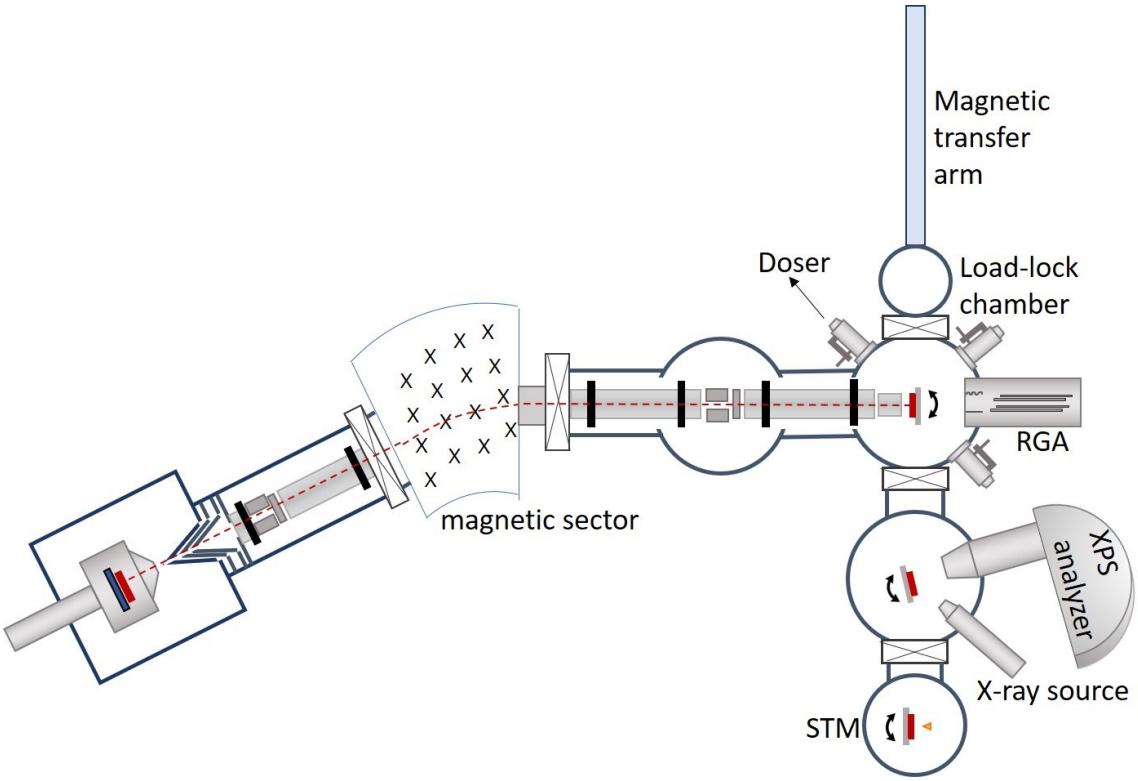

Figure 1.3 Previous beam line coupled surface analytical apparatus.

The magnetron setup consisted of a sputtering target placed in a magnetic field and biased to -500V where a mixture of argon and helium was introduced. Argon was ionized to create argon cations, which sputtered the metal target to produce a plasma. The added helium served to cool and transport the cluster anions down the beamline. Metal oxide, metal carbide, and metal sulfide clusters could be generated by adding oxygen, methane, and hydrogen sulfide respectively together with helium and argon. The cluster anions were then electrostatically accelerated before entering a magnetic sector mass spectrometer (25° sector magnet with resolution of $m/\Delta m = 20$). By tuning the magnetic field strength, a beam of cluster anions was mass-selected and focused by ion optics into the deposition chamber, where they were soft-landed (<1eV per atom) onto a piece of freshly peeled and annealed HOPG. The resulting sample could be cooled down to approximately 100 K by liquid nitrogen (LN_2) or heated up via resistive heating up to 800 K. The temperature of the sample was monitored by a K-type thermocouple spring loaded to the back of the HOPG.

Usually, it takes hours to prepare a sample due to the low ion intensity of the ion beam deposition method. However, reactants are usually introduced into the system within a relatively shorter time window. In fact, the reactant can be introduced into the system before, during[40] or after[16] a sample is made. In most studies on supported size-selected metal clusters, defect rich surfaces or metal oxide thin films that can interact strongly with the as-deposited metal clusters are chosen as substrates.[41] This is because they can offer preferred metal cluster binding sites, effectively pinning the clusters to the surface and inhibiting agglomeration as well as aggregation.[9, 42-43] It should be noted that in these studies, the reactants are generally introduced into the system after the sample preparation. However, in the previous studies done on the old apparatus, the inert and super flat HOPG surface was chosen to reduce cluster-substrate interactions. To also reduce the cluster-cluster interactions and promote the cluster-reactant interactions, size-selected clusters were deposited into a frozen matrix of reactants (such as 1,6-hexanedithiol and DMMP) formed on the HOPG substrate at 100K. This method was originally inspired by the common experimental technique used in the matrix isolation infrared spectroscopy.[44] Generally, noble gases such as argon are chosen to form a hosting matrix because of their inert nature as well as broad optical transparency. Using this matrix isolation technique, short lived, highly-reactive species can be trapped and analyzed by spectroscopic means.[45-46] This method was later adopted to probe the activities of metals or metal oxides towards a reactive matrix.[47-49] For instance, $(MoO_3)_3$ or $(WO_3)_3$ clusters were deposited into a reactive matrix of ethanol to study the clusters' dehydration and oxidation properties toward ethanol.[50] In those previous studies, we adopted a similar idea by freezing a reactive matrix of 1,6-hexanedithiol (chapter 2) as well as DMMP (chapter 3) onto an inert HOPG substrate, and we denoted this method as the Liquid Nitrogen Matrix Deposition method (LNMD method).

Newly built apparatus

The new apparatus was designed and constructed under the leadership of Dr. Zachary Hicks. All the details about the new apparatus were described in his thesis.[51] There are several major improvements in the new apparatus (Figure 1.4). First, the source chamber is compatible with three different ion sources such as magnetron sputtering, laser vaporization and pulsed arc cluster ionization source (PACIS). Compared to the old apparatus, which had magnetron sputtering as the only ion source, the new apparatus has a broader research scope with its capability of generating various clusters via three different cluster ion sources.

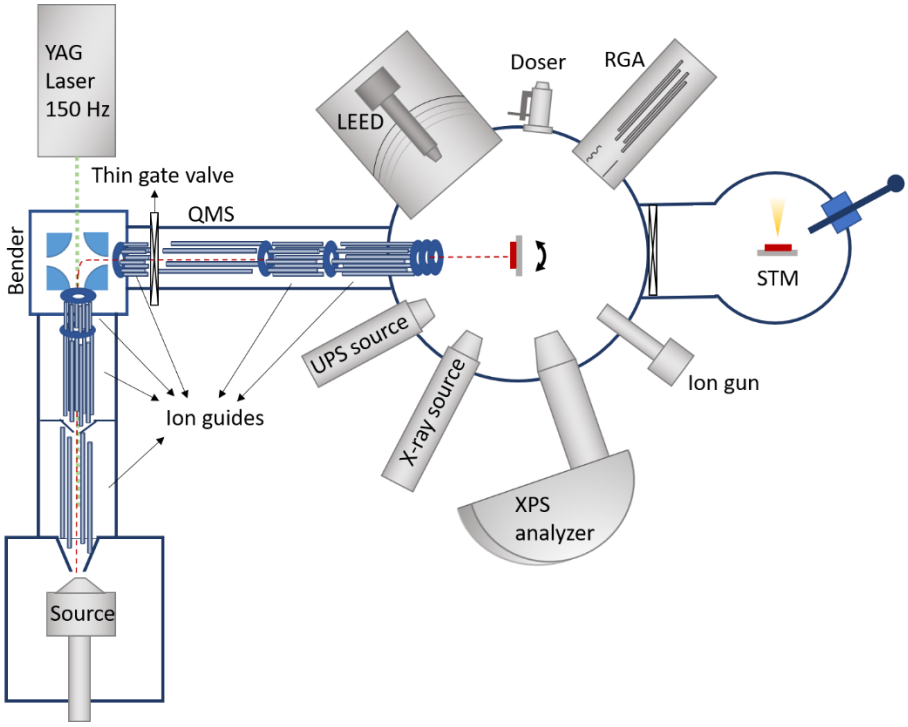

Figure 1.4 Scheme of the newly constructed apparatus.

The second improvement is the mass selection method. On the previous apparatus, the whole beam line needed to be floated to 500 to 1500 V since the cluster anions need to be accelerated to a certain kinetic energy to pass the magnetic sector for mass selection purposes. For a certain lead voltage value, the magnetic sector needs to be calibrated by Au_n^-. However, in the current set up, quadrupole mass spectrometry (QMS) serves as the mass selection tool. Therefore,

the cluster ions are guided through the whole beamline via quadrupole and octupole ion guides with relatively low kinetic energies.

The QMS also has higher accuracy and resolution than the magnetic sector. For example, Figure 1.5 shows a typical mass spectrum from the previous apparatus. It is clear that the magnetic sector can only differentiate the number of tungsten atoms but not the number oxygen atoms. For lighter elements such as copper, the mass spectrum usually looks like a big blob with all the peaks blur together. As is shown in Figure 1.6, the QMS is able to resolve oxygen atoms and it is clear that overoxidized tungsten oxide clusters are being made in the magnetron source.

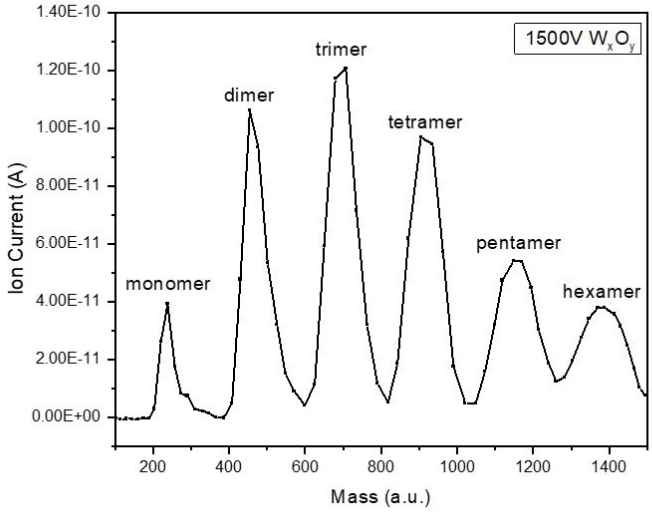

Figure 1.5 Mass spectrum for tungsten oxide clusters taken on the previous apparatus via a magnetic sector.

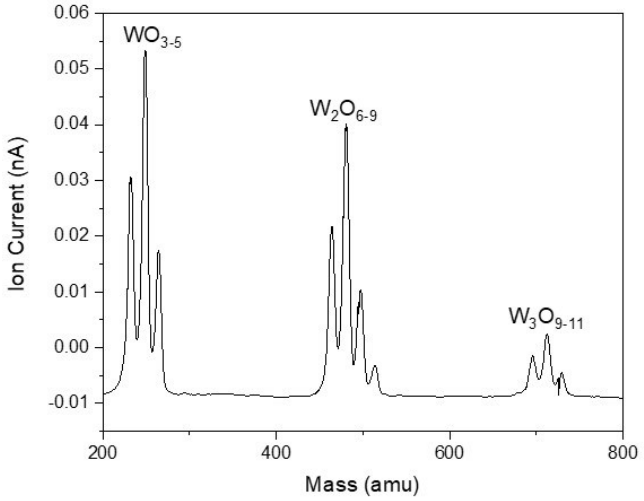

Figure 1.6 Mass spectrum for tungsten oxide clusters taken on the new apparatus via a quadrupole mass filter.

Another major improvement is the configuration of all the surface analytical equipment. In the previous apparatus, since the old TPD sample holder was not transferable, it was impossible to do in-situ XPS and LNMD TPD on the same sample. To mitigate that problem, TPD was carried out through the LNMD method using the TPD sample holder, and in-situ XPS was done by co-deposition of the reactant (DMMP) at relatively higher partial pressure.[40] However, in the new apparatus, the TPD and XPS are set up in the same chamber, therefore the TPD sample just needs to be transferred vertically to undergo all the measurements. Furthermore, the old transferable sample holder does not allow liquid nitrogen cooling, meaning that an XPS measurement could not be taken below room temperature. This problem can be overcome if the TPD holder can also be used for in-situ XPS as in the new apparatus. This improvement is very important because the reaction temperature is a decisive factor for the dominant reaction pathway. Specifically, XPS cannot be carried out on molecular DMMP on the previous apparatus since DMMP is usually chemically adsorbed or partially decomposed at room temperature. However, on the new apparatus, XPS for molecular DMMP can be taken at cryogenic temperatures when multilayers of DMMP are frozen on the HOPG substrate. In chapter 3, although almost all the data were acquired on the old

apparatus, the XPS spectrum for molecular DMMP (Figure 3.6) was obtained on the new apparatus, which provides a good binding energy reference for phosphorus.

The sample cleaning process has also been made much easier on the new apparatus. Since the old TPD sample holder was not transferable, cleaning the HOPG substrate using scotch tape exfoliation required breaking vacuum and taking the whole manipulator out. This was the case because the old apparatus was not originally designed for TPD experiments. The RGA and the TPD sample holder were features added later on to the old apparatus. The new apparatus, however, was designed to carry out TPD experiments on a daily basis. Therefore, a differentially pumped sliding seal has been designed and installed between the surface analysis chamber and the load-lock chamber. The sample can be cleaned at the bottom in the load-lock chamber while the pressure in the analysis chamber can still be maintained at low 10^{-9} torr. More details about the slide seal are described elsewhere.[51] Even though the original intention of adding the slide seal was great, its usage caused some unexpected issues later on. Those issues are discussed in chapter 4.

2. Ligation and Decomposition of 1,6-Hexanedithiol on Size-Selected Copper Clusters

ABSTRACT: Ligation and decomposition of 1,6-hexanedithiol on copper clusters have been studied by means of temperature-programmed desorption (TPD) and X-ray photoelectron spectroscopy (XPS). Copper cluster anions were first made via magnetron sputtering, then size selected and soft landed into a frozen matrix of 1,6-hexandithiol on HOPG maintained at 100K. After warming up to 298K, a combination of TPD and XPS were performed to characterize the newly deposited sample. TPD data shed light upon the adsorption and decomposition pathways of 1,6-hexanedithiol molecules on copper clusters. Based on the TPD data, two different binding motifs are proposed: the dangling motif is with one sulfur atom binding to a copper cluster, and the

bidentate motif is with both sulfur atoms binding to a copper cluster. Different decomposition products were observed for each binding motif. A series of hydrogen atom titration experiments were designed to provide further evidence for the proposed decomposition mechanism. XPS measurements at varied temperatures agree well with the TPD profile by confirming the formation of dithiol ligated copper clusters though Cu-S bond formation, and the decomposition of them via C-S bond scission. How well the dithiol ligand can protect the copper clusters from being oxidized is discussed and the ligand number per cluster is estimated.

2.1 Introduction

Exploring and understanding the catalytic properties of ultra-small metal clusters are of great significance not only in academia but also in industry. Ultra-small metal clusters, which have high surface to volume ratios and a high percentage of low-coordinated metal atoms on the surface, have unique physical and chemical properties that are distinct from their macroscopic counterparts. Numerous studies have highlighted the ability of the cluster deposition method to explore the catalytic reactivity of ultra-small clusters with different sizes, contents, and substrates.[41] Pioneering work on size selected Au_n and Pt_n clusters deposited on a Si(100) wafer by the Exxon group marked the emergence of this cutting-edge research field.[1] From then on, a lot of studies have been focusing on size selected noble metals such as Pt_n,[5, 52] Pd_n,[6-7, 53] Ag_n,[42, 54-55] and Au_n[8-9, 13, 56]. Copper, a readily available and less expensive catalyst, also served as a promising candidate in this field. For example, size-selected Cu_4 clusters supported on Al_2O_3 thin films have demonstrated promising catalytic activity towards the activation of CO_2 and its hydrogenation to methanol.[16]

Atomic sulfur is well known to poison the surface of many catalysts.[57-59] Adsorption studies of sulfur-containing molecules on different transition metal surfaces are of great interests to both catalytic and surface chemists.[60] There have been comprehensive adsorption studies for alkanethiols, especially the simplest methanethiol, on different metal single crystal surfaces.[61-67] There have also been studies of longer carbon chain monothiols especially on Cu single crystal surfaces.[68-69] However, studies on interactions between ultra-small copper clusters and alkanethiols using surface science techniques under ultra-high vacuum (UHV) are rare. Moreover, studies on bifunctional and longer carbon chain alkanethiols, such as 1,6-hexanedithiol, interacting with ultra-small copper clusters are even rarer.

Using inorganic synthesis and material science approaches, long alkanethiols, as well as complex thiol group containing organics, have been effectively used as capping agents for various nanoparticles.[70-73] It is reasonable to expect that the alkanethiols may behave differently with copper

clusters in a wet chemistry solution phase than in a surface science UHV environment. Only recently, J. E. Whitten et. al., have carried out a comparison study between colloidal copper oxide particles and oxidized copper single crystal surfaces, exploring the adsorption of thiols and reduction of copper oxides.[74] However, studies on the formation and decomposition of alkanethiol ligated copper clusters from a surface science perspective are still rare.

In this study, we use the size-selected cluster deposition method to study the interactions between ultra-small copper clusters of desired size and 1,6-hexanedithiol molecules. 1,6-hexanedithiol is chosen because of its bifunctional and six-membered carbon chain structure, which may result in unique adsorption and decomposition properties. In most studies on the catalytic properties of size-selected metal clusters, defect rich surfaces or metal oxide thin films that can interact strongly with the as-deposited metal clusters are chosen as substrates, because they can offer preferred metal cluster binding sites, effectively pinning the clusters to the surface and inhibiting agglomeration.[9, 41-43] However, in this study, the inert and super flat HOPG surface is chosen to reduce cluster-substrate interactions. To also reduce the cluster-cluster interactions and promote the cluster-ligand interactions, size-selected copper clusters are deposited into a frozen matrix of 1,6-hexanedithiol formed on the HOPG substrate maintained at 100K. This method is originally inspired by the common experimental technique used in the matrix isolation infrared spectroscopy.[75] Generally, noble gases such as argon are chosen to form a hosting matrix because of their inert nature and also broad optical transparency. Using this matrix isolation technique, short lived, highly-reactive species can be trapped and analyzed by spectroscopic means.[45-46, 76] This method was later adopted to probe the activities of metals or metal oxides towards a reactive matrix.[47-49, 77-78] For instance, $(MoO_3)_3$ or $(WO_3)_3$ clusters were deposited into a reactive matrix of ethanol to study the clusters' dehydration and oxidation properties toward ethanol.[50] A graphene thin film over Pt(111) was chosen as an inert substrate not only for its unreactivity toward alcohols, but also to minimize the substrate's effects on the acidic and redox properties of those metal oxide

clusters.[50] In this study, we adopt a similar idea by freezing a reactive matrix of 1,6-hexanedithiol onto an inert HOPG substrate. After deposition, the HOPG substrate was warmed up to 298K, when dithiol ligated copper clusters were believed to form. Then, temperature-programed desorption (TPD) and X-ray photoelectron spectroscopy (XPS) measurements were carried out to characterize and understand the adsorption and decomposition properties of 1,6-hexanedithiol on copper clusters.

2.2 Experimental Methods

Copper clusters Cu_n^- were prepared as negative anions by a magnetron sputtering source. After acceleration, mass selection and deceleration, they were then deposited (soft-landed) onto a highly-ordered pyrolytic graphite (HOPG, Bucker, ZYB grade, $1.2 \cdot 1.2$ mm^2, 2 mm thickness) substrate in ultra-high vacuum (base pressure $1 \cdot 10^{-9}$ torr). The whole setup has been described in detail elsewhere.[79]

The magnetron setup consisted of a copper sputtering target (99.99%) placed in a magnetic field and biased to -500V when a mixture of argon (Airgas, 99.999%) and helium (Airgas, 99.999%) was introduced. The argon gas was ionized to create argon cations, which sputtered the metal target to produce a plasma. The added helium served to cool and transport the cluster anions down the beamline, where they were then electrostatically accelerated before entering a magnetic sector mass spectrometer (25^o sector magnet with resolution of $m/\Delta m = 20$). By tuning the magnetic field strength, a beam of Cu_n^- (for Cu_{100}^-, n=100±5) cluster anions was mass-selected and focused by ion optics into the deposition chamber, where they were soft-landed (<1eV) onto a freshly peeled and annealed HOPG surface. The resulting sample could be cooled down to approximately 100K by liquid nitrogen (LN_2) or heated via resistive heating to 720K by passing current through a piece of HOPG. The temperature of the sample was monitored by a K-type thermocouple spring loaded to the back of the HOPG.

Dithiol ligated copper clusters were made via the Liquid Nitrogen Matrix Deposition method (LNMD method). HOPG samples were cleaved in air right before being transported into the vacuum chamber and then annealed at 720K for 30 minutes before use. 1,6-hexanedithiol(96%) purchased from Sigma Aldrich was degassed by three freeze-pump-thaw cycles before being introduced into the vacuum chamber through a UHV compatible leak valve. For the LNMD method, the dithiol was dosed into the chamber when the HOPG had already been cooled down to and held at 100K, forming multilayers on the HOPG surface. The dose of the dithiol was monitored by a pressure gauge and a residual gas analyzer (RGA) (Hiden HAL/3F PIC quadrupole mass spectrometer (QMS)). And the dose amount was given in Langmuir (L, 10^{-6} torr·s). After dosing, size selected copper clusters were deposited into that pre-made frozen dithiol matrix. During deposition, the deposition current was monitored by a picoammeter, and the coverage of the as-deposited clusters was given in current (ampere, A) integrated over time (second, s). For each deposition, the average deposition current was about 70 pA, corresponding to an average deposition speed of $4 \cdot 10^{8}$ clusters per second; and the final deposition amount was controlled to be 1·10-6 A·s, corresponding to the total amount of $6 \cdot 10^{12}$ clusters on a 1.2·1.2 centimeter square substrate. After deposition, the sample was ramped up from 100K to 298K by resistive heating.

Once warmed up to 298K when the dithiol ligated copper clusters were believed to have formed, temperature-programmed desorption (TPD) was used to characterize dithiol decomposition properties on copper clusters. Desorption products were detected and identified by a QMS which was positioned normal to the plane of the substrate at a distance about 5 mm, also the entrance of the QMS is covered by a glass shroud with a 6 mm diameter hole cut in the center, both of which can help to minimize the contribution from background gases and maximize the sensitivity toward the species desorbing directly from the substrate. For the custom TPD sample holder, two small pieces of tantalum foil are wrapped on two copper power rods respectively for resistive heating purpose, and a piece of HOPG is held between them.

The as-prepared dithiol ligated copper clusters were also characterized via ex-situ XPS with non-monochromatic Mg Kα-rays (1253.6 eV), and the kinetic energies of ejected electrons were analyzed via a high energy hemispherical analyzer. To accomplish this, the sample needed to be taken out of the deposition chamber and then transferred into an adjacent chamber dedicated to XPS. For XPS measurements at varied temperature, the sample was heated in-situ via e-beam heating to the desired temperatures and then cooled back down to about 300K, at which XPS spectra were recorded. All the XPS spectra were calibrated by graphite carbon 1s at 284.5eV.[80] Sulfur XPS spectra were numerically fitted with the Gaussian broadened Lorentzian function (LF(1,1,25,280)) after a Shirley background subtraction in CasaXPS (CasaXPS, Casa Software Ltd.). S 2p spin-orbital splitting doublets composed of two components separated by 1.18eV with an integrated area ratio of 1:2.[65] Full width at half maximum (FWHM) were controlled in a range of 3.5-4 eV depending on the surface species when using a pass energy of 178.95 eV. For each oxidation state, same binding energy range constrains, intensity ratio and FWHM were set for spectra obtained under different annealing temperatures.

2.3 Results and Discussion

2.3.1 1,6-hexanedithiol Reaction Pathway on Copper Clusters

The reaction pathways of 1,6-hexandithiol on copper clusters were studied via TPD. HOPG has been used as an inert carbon substrate to study the desorption energetics of alkane derivatives as well as the catalytic reactivity of clusters through TPD.[81-83] There are also STM and AFM studies on self-assembly of organic molecules using HOPG as an inert substrate.[84] However, there are not many TPD studies of alkanethiols on HOPG. The LNMD method requires formation of a dithiol matrix; however, most of the dithiols are just physi-adsorbed on the HOPG surface due to the low intensity of the cluster deposition. Therefore, the physi-desorption properties of 1,6-hexanedithiol on HOPG without copper clusters was studied via TPD initially.

Figure 2.1 shows the TPD profile of 1,6-hexandithiol desorption from HOPG without copper clusters. Figure 2.1 (a) shows the TPD spectra of intact dithiol (m/e=150) with varied dose amount. For a dose larger than 0.2L, there are apparently three features, each of which is associated with dithiol molecules desorbing from a different surface layer. At the lowest temperature (230K), there is an intense, sharp peak due to multilayers' desorption; a broad peak lies in a slightly higher temperature range (~260K) representing the monolayer; also note that there is a less intensive shoulder possibly coming from the sample holder at a slightly higher temperature (~310K). As the dose amount decreases, the first two peaks shift to lower temperatures with lower intensity, suggesting a 0^{th} order desorption indicative of physi-adsorption. Also note that even when the dose is decreased to 0.05L, the multilayer peak still exists and that for increasing dose amounts, the monolayer peak does not seem to be saturated when the multilayer peak is already very strong. These two features suggest that the adsorbates may grow according to a Volmer-Weber mechanism rather than a layer-by-layer mode.[85] In other words, multilayers tend to form when a monolayer hasn't formed completely. The similar mechanism has also been proposed to explain acetone adsorption on HOPG based on experimental and theoretical investigations.[86]

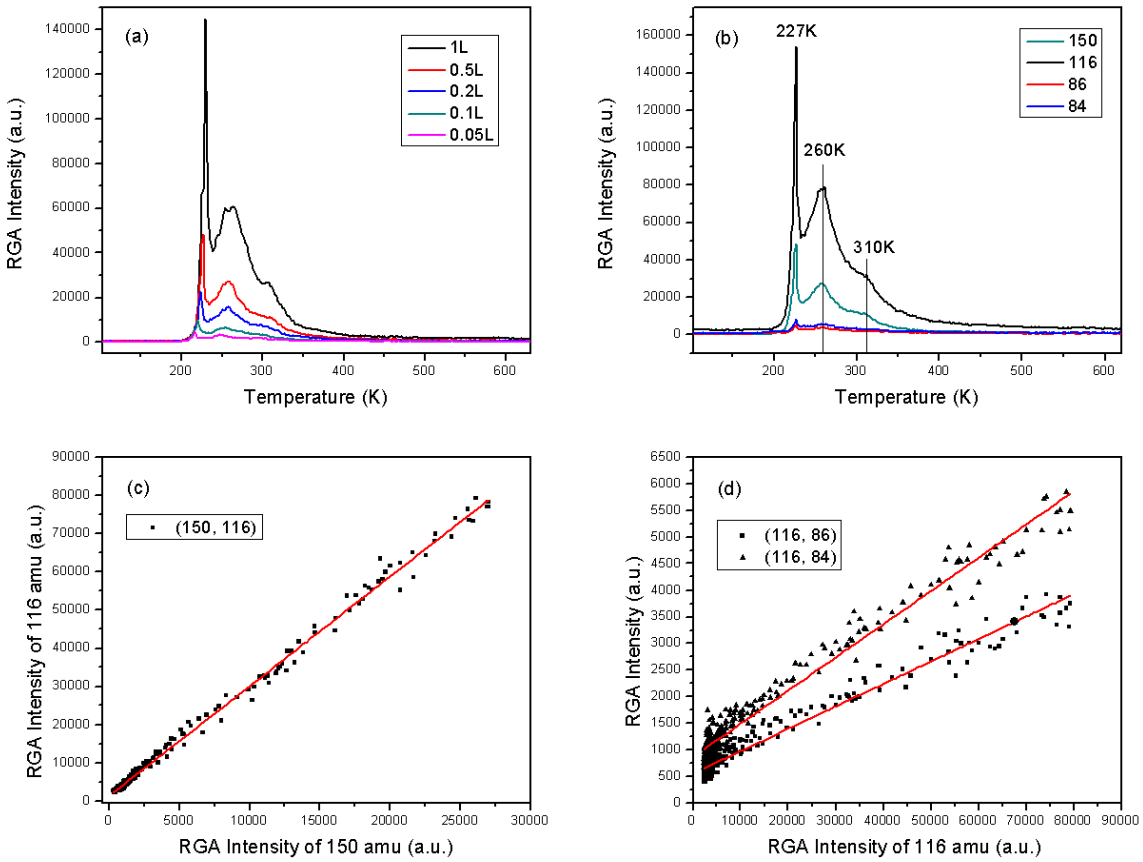

Figure 2.1 TPD profile of 1,6-hexanedithiol physi-desorption on HOPG substrate. (a) TPD scans of molecular dithiol (m/e=150) as a function of dose amount; (b) Composite TPD scans of 0.5L dose: molecular dithiol (m/e=150), monothiol (m/e=116), hexane (m/e=86) and cyclohexane (m/e=84); (c) ■: RGA intensity of the monothiol plotted to that of the molecular dithiol, red line is the linear fitting (slope: 2.97±0.01, intercept: 1380±80, R^2: 0.996); (d) ■: RGA intensity of hexane plotted to that of the monothiol and the corresponding linear fitting (slope: 0.0422±0.0005, intercept: 553±11, R^2: 0.96) ▲:RGA intensity of cyclohexane plotted to that of the monothiol and the corresponding linear fitting (slope: 0.0648±0.0006, intercept: 866±14, R^2: 0.97)

The dose amount was maintained at 0.5L for the rest of the TPD experiments for better consistency. Figure 2.1 (b) shows a composite TPD scan collected from a dose of 0.5L. Monothiol of m/e=116 is one of the major fragments of 1,6-hexanedithiol through desulfurization, while

hexane (m/e=86) and cyclohexane (m/e=84) are not the major fragments based on the relatively low RGA intensity. Linear fittings shown in Figure 2.1 (c) and (d) by RGA intensity of the fragments versus that of the intact dithiol reveal that the fragmentation pattern remains constant for the whole desorption process, indicating that neither the HOPG substrate nor the sample holder causes obvious decomposition of the dithiol molecules.

For an experimental TPD scan, data cannot be collected from 100K all the way to 700K, because the intensive physi-desorption signal will overwhelm the desorption peaks caused by the copper clusters. A compromising solution is to ramp up to 298K first, then remain there for 30 min to remove any physi-absorbed dithiol, then collect the TPD spectra from 298K to 700K. As is shown in Figure 2.2 (a), it is identified that monothiol (m/e=116), hexane (m/e=86) and cyclohexane (m/e=84) are the major volatile products that desorb upon heating. There are three desorption temperature regions: a low temperature region in the 350-420K range, a medium temperature region in the 460-540K range, and a high temperature region in the 540-600K range. In each region, there is a different combination of the three desorption products. It should be mentioned that before each deposition, a background scan was carried out to make sure that there was no obvious peak in the 350-600K temperature region, and also to obtain the fragmentation ratios which were later on used to subtract the contributions due to ionization fragmentation of the intact dithiol molecules.

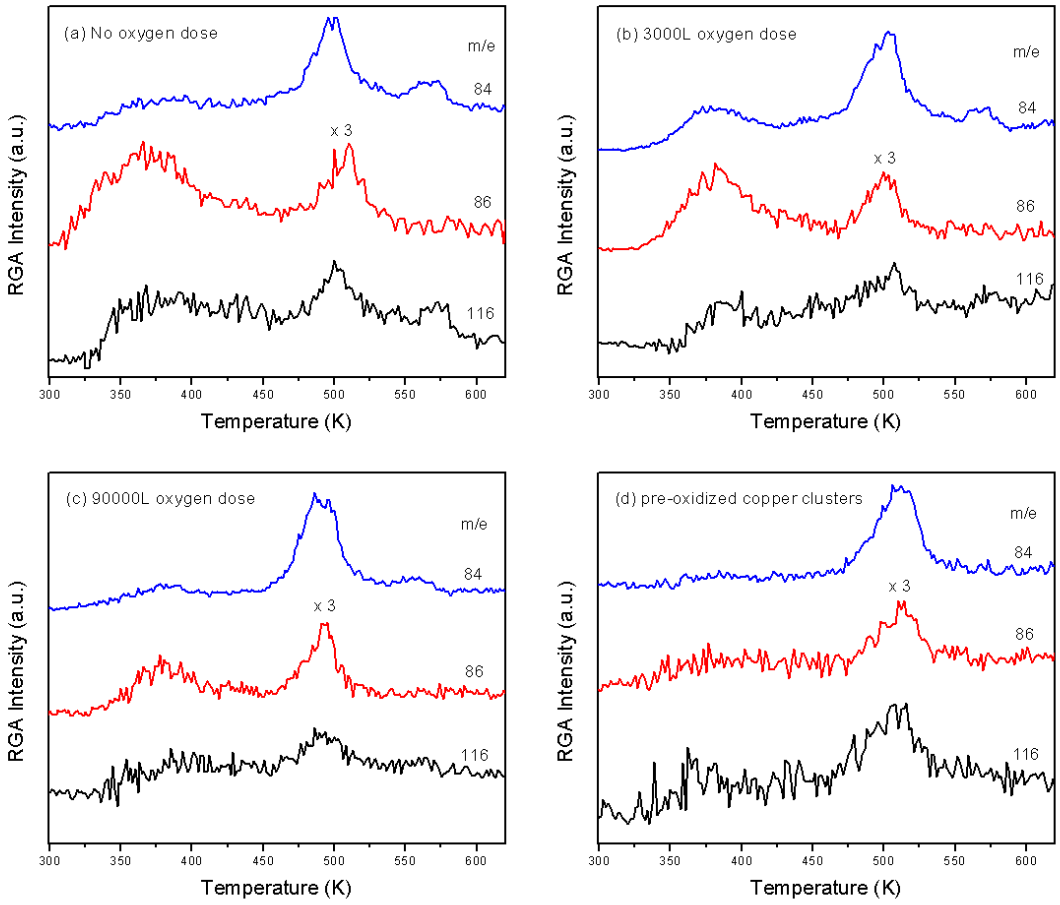

Figure 2.2 Composite TPD of dithiol ligated clusters under different oxygen conditions: (a) Cu100 without dosing oxygen; (b) Cu100 with 3000L oxygen dosing; (c) Cu100 with 90000L oxygen dosing; (d) (CuO)80 without dosing oxygen.

In the low temperature region, hexane is the major desorption product. There is also a rising terrace for the monothiol, part of which may be due to a rising background. However, the cyclohexane peak is too weak to be discernable from the background. In the medium temperature range, all three decomposition products are observed, among which cyclohexane is the major product. In the high temperature region, there is no peak for hexane, but two small peaks for cyclohexane and monothiol. Comparing these three temperature regions and their respective three desorption species, the following can be established: 1. The medium temperature region is the

major desorption region because of the higher intensity of desorption peaks, especially for cyclohexane, as well as the certain existence of all three decomposition species; 2. Monothiol is the only species that desorbs in all three temperature regions; 3. Both hexane and cyclohexane evolve in two consecutive temperature regions; 4. Hexane is likely to form in a relatively low temperature range, while cyclohexane tend to evolve in a relatively high temperature range; 5. Every temperature region has at least two desorption species, the peak positions of which coincide with each other very well.

Monothiol (m/e=116) can get fragmented to produce an ion with an m/e of 86 or 84 by electron bombardment in the ionization zone of a QMS. However, the evolutions of m/e=86 and m/e=84 do not really follow that of m/e=116 as is shown in Figure 2.2 (a). Moreover, as the linear fitting in Figure 2.1 (d) illustrates, the percentages of m/e=116 that can fragment into ion species of m/e=86 or m/e=84 due to electron bombardment are very limited (less than 7% percent). Based on these two facts, even though the peaks of m/e=86, 84 and 116 appear coincident, the evolutions of m/e=86 and 84 are from decomposition of dithiol on copper clusters instead of fragmentation of m/e=116 in the ionization zone.

The proposed adsorption and decomposition mechanism of 1,6-hexanedithiol is shown in Figure 2.3. First, size selected copper clusters (Cu_n^-, n=100±5) are deposited into a pre-made 1,6-hexanedithiol frozen matrix. Secondly, while ramping up to room temperature, dithiol molecules either chemisorb to the copper clusters via S-H bond scission and Cu-S bond formation, or physi-desorb from HOPG. Since a 1,6-hexanedithiol molecule has two thiol groups, it can anchor to a copper cluster with one end forming a dangling dithiol (equation (1)) or with both ends forming a bidentate dithiol (equation (2)). Thirdly, during a TPD ramp, the chemisorbed dithiol molecules undergo decomposition via C-S bond scission. A dangling dithiol will lose one sulfur after C-S bond scission and form a six-carbon monothiol (equation (3)), while a bidentate dithiol will either recombine with two absorbed hydrogen atoms to form hexane (equation (4)) or undergo

intramolecular coupling to form cyclohexane (equation (5)). Finally, only atomic sulfur atoms remain on the copper clusters.

$$HSC_6H_{12}SH\ (a) \rightarrow HSC_6H_{12}S\ (a) + H\ (a) \quad (1)$$

$$HSC_6H_{12}SH\ (a) \rightarrow SC_6H_{12}S\ (a) + 2H\ (a) \quad (2)$$

$$HSC_6H_{12}S\ (a) \rightarrow HSC_6H_{12}\ (g) + S\ (a) \quad (3)$$

$$SC_6H_{12}S\ (a) + 2H\ (a) \rightarrow C_6H_{14}\ (g) + 2S\ (a) \quad (4)$$

$$SC_6H_{12}S\ (a) \rightarrow C_6H_{12}\ (g) + 2S\ (a) \quad (5)$$

$$2H\ (a) \rightarrow H_2\ (g) \quad (6)$$

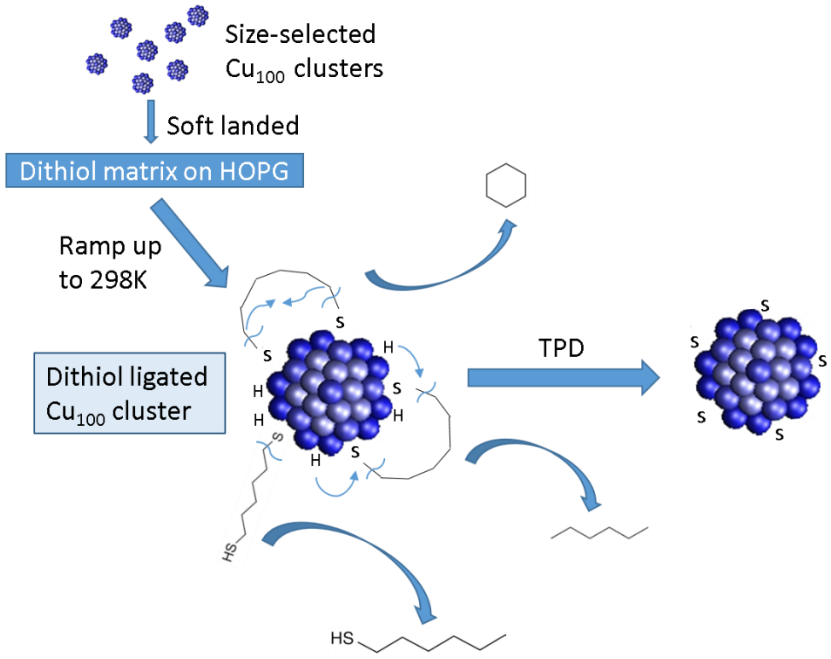

Figure 2.3 Diagram of the formation of 1,6-hexanedithiol ligated copper clusters and the decomposition of dithiol on copper clusters.

This decomposition mechanism is proposed based on the TPD spectra of our supported copper clusters system and also the literature on monothiol copper single crystal system. From the point of view of surface science studies, the simplest monothiol, methanethiol, has been the starting point

of studies on interactions between thiols and copper single crystal surfaces.[19] Adequately high resolution XPS measurements and HREELS spectra have identified the main surface species as an intact, physi-adsorbed molecule at the lowest temperature (~80K); a surface thiolate, i.e. methyl mercaptide, produced by deprotonation at slightly higher temperatures (still lower than room temperature); the formation of atomic sulfur via C-S bond scission and the evolution of hydrocarbon products occur at temperature higher than 300K.[60, 64] Combined TPD studies have identified the evolution of methane formed via recombination of adsorbed hydrogen, ethane formed via intermolecular coupling, ethene formed via coupling and C-H bond scission, as well as H_2 formed via adsorbed hydrogen atoms recombination.[60, 65-66]

Compared to single crystal studies, hexane observed in our system is speculated to evolve through the similar hydrogen recombination reaction pathway. In terms of coupling reactions, Hung et.al. have found that intermolecular coupling of alkyl groups is not observable for C_2H_5SH and C_4H_9SH, in contrast with CH_3SH.[65] They attribute that to the possibility that longer alkyl groups might diffuse along the surface with greater difficulty, or the molecular orientation for coupling may be restrictive.[65] In our system, instead of undergoing intermolecular coupling, ideal carbon chain length and bifunctional nature make it more feasible for 1,6-hexanedithiol to form a stable six-membered ring via intramolecular coupling. With both sulfur atoms binding to copper clusters through a bridge structure, the two ends are forced to stay close to each other for facile coupling without necessary diffusion process.

As explained above, ionization induced fragmentation has been ruled out for causing the coincidence of desorption peaks. Also note that thermal induced C-S scission is the elementary reaction step involved in the evolution of each desorption product. Hence, it is reasonable to speculate that C-S scission is the rate-limiting step for the evolution of all three desorption products.

2.3.2 Adsorbed Hydrogen Atom Titration.

As was summarized for Figure 2.2 (a) previously, hexane is likely to evolve in a relatively low temperature range, while cyclohexane tends to desorb in a relatively high temperature range. Considering the hydrogen recombination mechanism for the evolution of hexane, it is speculated that this phenomenon is caused by the fact that the amount of absorbed hydrogen decreases during the ramp. In the low temperature region, there are plenty of absorbed hydrogen, resulting in preferential formation of hexane; in the medium temperature region, when there is significantly less absorbed hydrogen, cyclohexane becomes prevalent; in the high temperature region, the absorbed hydrogen atoms have all undergone either C-H formation (equation (4)) or H-H formation (equation (6)), making it impossible for hexane to evolve, but still possible for cyclohexane or monothiol to evolve.

To provide more evidence for this proposed mechanism, a series of hydrogen atom titration experiments have been designed. For a typical titration TPD scan, the sample was held at 298K and oxygen was background introduced into the vacuum chamber via a UHV compatible leak valve. The purpose of this titration experiment is to use dosed oxygen to react and then remove the adsorbed hydrogen atoms at 298K. The effects of this titration process should be revealed in the TPD ramp afterwards. Background experiments have also been done with the same amount of oxygen dosing but no deposited copper clusters, and there is no obvious peak in the 350-600K range (data not shown here), which is very similar to the TPD with dosing only the dithiol molecules.

Qualitative changes in the TPD spectra were observed when 3000L of oxygen was background dosed at 298K. As is shown in Figure 2.2 (b), the major change occurred in the low temperature region, namely, the appearance of a small, broad peak of cyclohexane coinciding with that of hexane. Figure 2.4 (a) and (b) show a better comparison between the runs without and with dosing oxygen for solely cyclohexane. A reasonable explanation for this phenomenon is that the dosed oxygen can titrate some of the adsorbed hydrogen atoms. As a result, in the low temperature region,

not all of the bidentate dithiols have a chance to recombine with hydrogen atoms then form hexane. Hence, some of the dithiol species will undergo intramolecular coupling and form cyclohexane. In other words, dosing 3000L of oxygen at 298K can titrate the absorbed hydrogen atoms partially, thus making hydrogen recombination and intramolecular coupling the two competing reaction pathways for bidentate dithiol binding motif in the low temperature region.

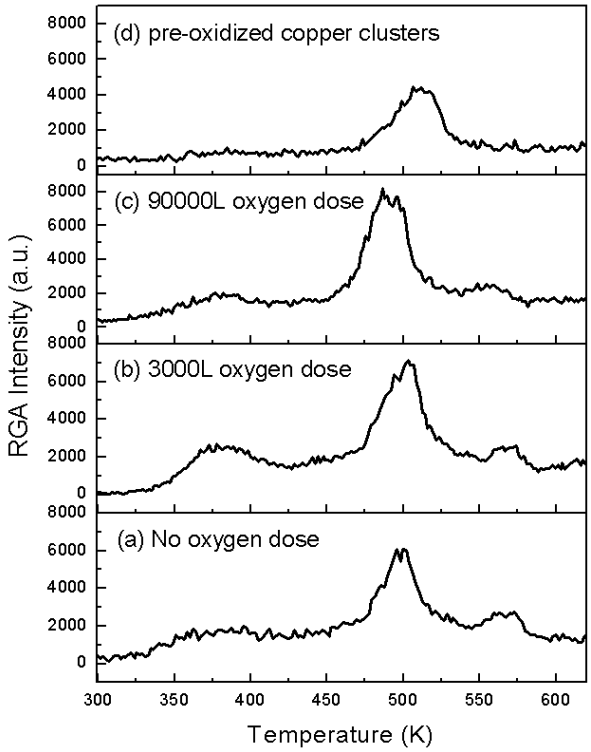

Figure 2.4 TPD scans of cyclohexane (m/e=84) collected from 1,6-hexanedithiol ligated clusters supported on HOPG as a function of different oxygen conditions.

If we follow this idea, it seems reasonable to expect that increasing the amount of dosed oxygen can eventually titrate almost all of the absorbed hydrogen atoms such that hexane may disappear from the TPD spectra. However, it turned out not to be the case. Figure 2.4 (c) shows that, after a significantly larger amount of oxygen (900000L) being background dosed into the chamber, the low temperature peak for cyclohexane becomes weaker compared to that in Figure 2.4 (b). In fact,

it almost disappears and becomes comparable to the peak from the TPD spectrum without an oxygen dose shown in Figure 2.4 (a). Also note that the medium temperature peak for cyclohexane gets larger and broader, while the high temperature peak becomes less discernable from the background. Additionally, for hexane, the low temperature peak gets weaker compared to the medium temperature peak. In general, a larger oxygen dose causes a redistribution of desorption products from the low and high temperature regions to the middle temperature region.

In fact, dosed oxygen can not only titrate absorbed hydrogen but also form chemisorbed oxygen on copper clusters. With a relatively small amount of oxygen (3000L), the main effects revealed in the TPD spectra is its partial titration effects. However, with a larger amount of oxygen (90000L), after some adsorbed hydrogen atoms being titrated, the copper clusters can start to become oxidized. Small clusters, such as Cu_{100}, can have their chemical properties and electronic structure perturbed as a result of oxidation on the surface. And these perturbations can have discernible influences in the TPD spectra. The evolution of desorption peaks from Figure 2.2 (b) to Figure 2.2 (c) indicates that the effects stemming from oxidation of copper clusters with a large oxygen dose may overwhelm the effects of partial hydrogen titration, which should be revealed with a relatively small amount of oxygen otherwise. To gain more evidence to support this uncertain statement, a pre-oxidation experiment was carried out. Unlike the titration experiment, in which oxygen was introduced after the ligation process; for this pre-oxidation experiment, we made copper oxide cluster anions by introducing oxygen into the magnetron source, then $(CuO)_{80}^-$ (same m/e as Cu_{100}^-) was mass selected, and finally deposited into the frozen dithiol matrix. Therefore, copper clusters were oxidized first, and then got ligated by dithiol molecules.

As is shown in Figure 2.2 (d), the $(CuO)_{80}$ dithiol TPD spectrum has only one desorption region, which is close to the medium temperature region shown in Figure 2.2 (a), (b) and (c). This means that, unlike Cu_{100}, which has three very different groups of binding sites; on $(CuO)_{80}$ clusters, there is only one group of binding sites, the sulfur binding energies of which are similar to that of the

binding sites corresponding to the medium temperature region for Cu_{100}. Moreover, the peaks of the three major desorption species coincide with each other very well, indicating that C-S bond scission is also the rate limiting step for decomposition and desorption of the adsorbed dithiol on $(CuO)_{80}$ clusters.

As for now, there is a series of TPD experiments with different oxygen effects: without oxygen, a small amount of oxygen, a large amount of oxygen and pre-oxidation. Since the pre-oxidation one is with oxidized copper clusters, it can be seen as the maximum dosing amount of oxygen. For the three desorption products, Figure 2.4, Figure 2.5 and Figure 2.6 show the evolution of each species under different oxygen conditions, sorted (bottom to top) in order of increasing oxygen amount. As oxygen amount increase, the changes occur mainly in the low temperature region for hexane and cyclohexane. For hexane, the intensity of the peak in low temperature region gradually decreases until finally disappears. For cyclohexane, a weak and broad peak appears with a small amount of oxygen, and then becomes weaker until finally disappears. Based on the evolution of TPD spectra of hexane and cyclohexane, it is likely that with a small oxygen dosing amount such as 3000L, the TPD spectra reveal the partial hydrogen titration effects, and that with a larger oxygen dosing amount such as 90000L, the TPD spectra reveal mainly the oxidation effects.

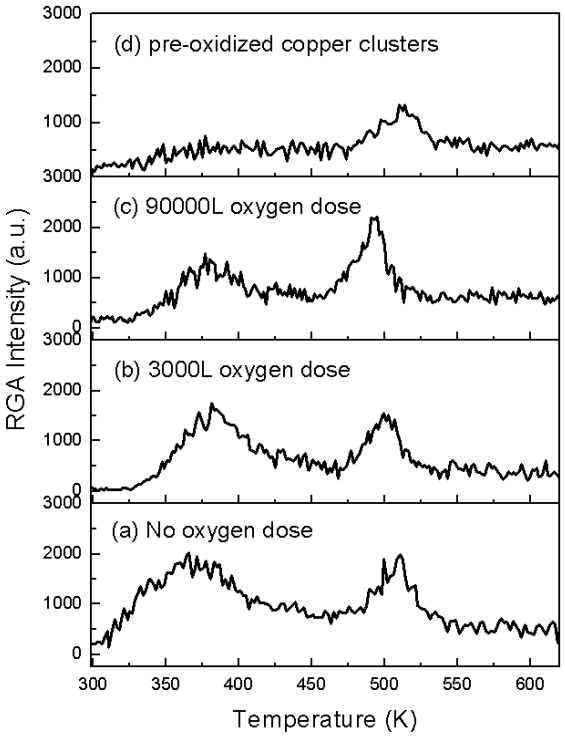

Figure 2.5 TPD scans of hexane (m/e=86) collected from 1,6-hexanedithiol ligated clusters supported on HOPG as a function of different oxygen conditions.

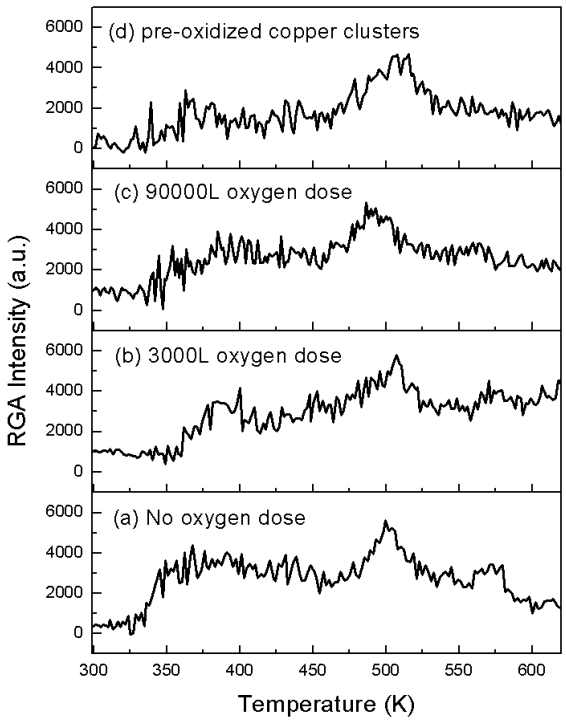

Figure 2.6 TPD scans of the monothiol (m/e=116) collected from 1,6-hexanedithiol ligated clusters supported on HOPG as a function of different oxygen conditions.

2.3.3 XPS Characterization.

Surface species formed upon ligation and left behind after annealing on Cu clusters were identified chemically using XPS. Figure 2.7 shows the spectra of S 2p sorted (bottom to top) in order of increasing annealing temperature. In the case of 298K, the binding energy of S $2p_{3/2}$ is observed predominantly at 162.6 eV, which is attributed to the thiolate group (Cu-S-R). The higher binding energy peak at 167.3 eV indicates that some thiol groups get oxidized when exposed to air. No obvious oxidation state at around 164-165eV is observed, which should be assigned to intact thiol groups. It is speculated that some thiol groups from the dangling ligands may be oxidized or chemisorbed to the oxidized copper clusters.

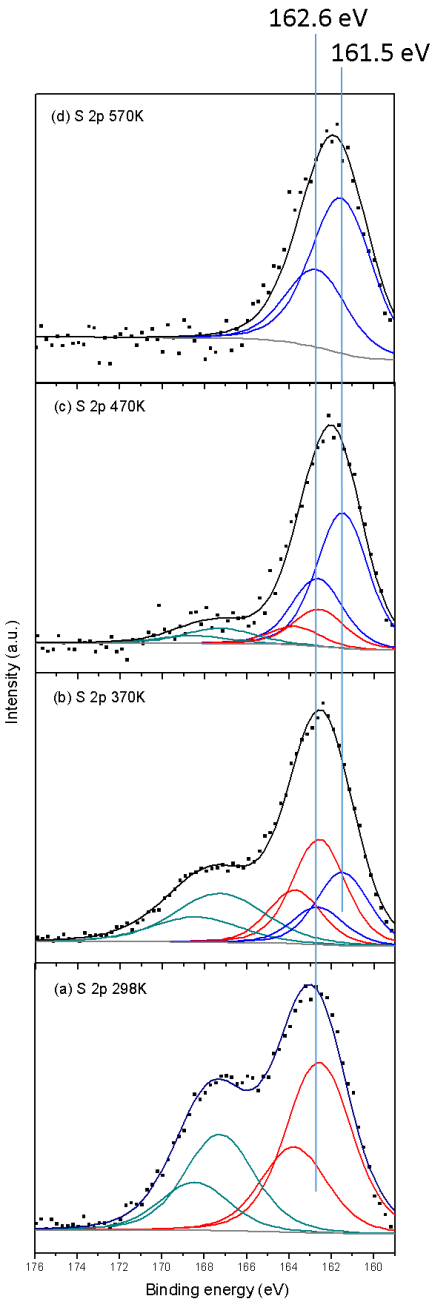

Figure 2.7 XPS spectra for S 2p from dithiol ligated copper clusters supported on HOPG at varied temperature: (a) 298K; (b) 370K; (c) 470K; (d) 570K. Black dots are the experimental data. Different deconvoluted oxidation states are marked with different colors. Each oxidation state has two spin-orbital splitting components with a same color. The black line is the overall fitting curve. The light blue vertical lines mark the binding energies of the two critical oxidation states.

As is shown in Figure 2.7 from (a) to (d), the major envelope peak position gradually shifts to lower binding energy. Deconvoluted peaks reveal three different oxidation states: 161.5 eV, 162.6 eV and 167.3eV, refer to sulfur oxidation states in Cu-S, Cu-S-R and SO_2, respectively. From 298K to 570 K, the peak of S $2p_{3/2}$ at 162.6 eV due to Cu-S-R gradually disappears as a result of C-S bonds scission. Meanwhile, the peak of S $2p_{3/2}$ at 161.5eV increases, indicating the formation and accumulation of atomic sulfur atoms on the copper clusters. At 570 K, no obvious 162.6eV component exists, implying that all the Cu-S-R species have decomposed and that the atomic sulfur that bind to copper is the only version of sulfur left behind. In this dithiol copper clusters system, the evolution of sulfur oxidation states agree with the studies of different thiols' adsorption and decomposition on copper single crystal surfaces.[65-66] In those studies, similar binding energies were identified for different sulfur species, such as Cu-S-R at 162.4 eV and Cu-S at 161.5 eV. Unlike the XPS analysis on single crystals, the C 1s signal from the carbon chain is not shown here, because it is overwhelmed by the strong graphene carbon signal due to the HOPG substrate.

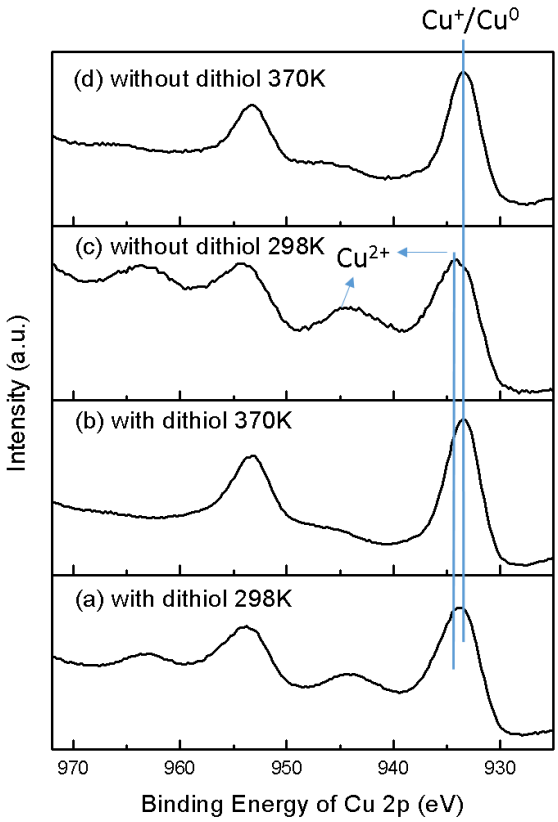

Figure 2.8 XPS spectra for Cu 2p from dithiol ligated copper clusters and bare copper clusters at varied temperature: (a) ligated clusters at 298K; (b) ligated clusters after being annealled at 370K; (c) bare clusters at 298K; (d) bare clusters after being annealled at 370K. The blue verticle lines mark the shift of peak position for Cu $2p_{3/2}$. The blue arrows mark the import features for Cu^{2+}.

It would be interesting to know how well 1,6-hexanedithiol can protect the copper clusters from oxidation under ambient environment. In fact, when exposed to air, the oxidation process can be partially hindered by the dithiol ligands, as demonstrated in Figure 2.8. The relatively lower intensity of satellite peaks and slightly lower binding energy for Cu 2p3/2 at 933.8 eV in Figure 2.8 (a) compared to Figure 2.8 (c) (Cu 2p3/2 at 934.2eV), confirm the reduced formation of CuO in the dithiol ligated clusters. Note also that the peak shape in Figure 2.8 (c) implies full oxidation to CuO. Since copper sulfur interaction is fairly strong, it is speculated that dithiol may occupy

most of the reactive sites on the copper clusters, thus increasing the reaction barrier for oxygen to oxidize the copper clusters afterwards. These results agree with the copper single crystal studies.[66] Davies et al. have demonstrated that oxygen chemisorption on Cu(110) occurs at low methyl mercaptide coverage but can be completely inhibited at high methyl mercaptide coverage under UHV.[66] Formed via LNMD method, dithiol ligated copper clusters in our system can be seen as alkanethiol chemisorbed to copper single crystal surfaces in the high coverage scenario. However, only partial, rather than complete, inhibition of oxidation was seen is likely due to: 1. 1,6-hexanedithiol has a long carbon chain, with both ends anchoring to a copper cluster and a relatively bulky bridge structure, preventing active sites from being fully saturated by dithiol; 2. Clusters as small as Cu_{100} are more reactive than copper single crystal surfaces in terms of oxidation reactions; 3. Exposure to ambient pressure is a more severe oxidative situation than dosing oxygen into a UHV chamber.

XPS measurements for Cu 2p at varied temperature are also shown in Figure 2.8. Unlike the gradual evolution of sulfur oxidation states from 298K to 570K, the major change for Cu happened immediately when heated up to 370K. By comparing Figure 2.8 (b) to Figure 2.8 (a), it is obvious that the satellite peaks of Cu^{2+} have almost disappeared upon heating. Moreover, the Cu $2p_{3/2}$ peak at 370K becomes narrower, implying fewer oxidation states; and shifts to a lower binding energy (933.5 eV), indicating the dominance of low oxidation states (Cu^{+} or Cu^{0}). Further annealing to 470K and then 570K only shifted the peak slightly to a lower binding energy of 933.4 eV (data not shown here). By comparing Figure 2.8 (d) to Figure 2.8 (c), it is apparent that, without dithiol ligands, Cu^{2+} still get reduced when heated up to 370K. In fact, heating under UHV is a quite reductive environment for many metal oxides. For example, White et al. have found that for partially oxidized Cu films, CuO gets reduced to Cu_2O at around 380K.[87] In this sense, the reduction shown in Figure 2.8 (b) is assigned to the thermally induced reduction instead of the ligation-induced reduction.

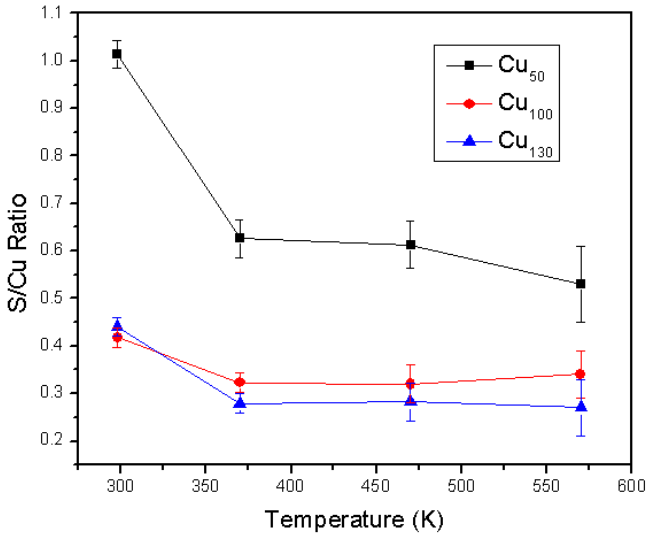

Figure 2.9 S/Cu ratios of varied cluster sizes and varied temperatures as implied in the graph.

Very similar evolutions of sulfur oxidation states and copper oxidation states were seen for varied sizes of copper clusters. Upon ramping to 298K, it is more likely that dithiol molecules are only ligated to the surface of the copper clusters to form dithiol ligated copper clusters. Therefore, it is expected that the S/Cu ratios should be different among varied cluster sizes. The S/Cu ratios were calculated using the integrated area and then normalized by relative sensitivity factors (sulfur: 0.668, copper: 5.321). As is shown in Figure 2.9, the smaller are the clusters, the larger are the S/Cu ratios. The S/Cu ratios of dithiol ligated Cu_{130} and Cu_{100} clusters are quite close to each other; however, when the cluster size decreases to 50, the S/Cu ratio increases dramatically. It is also worth noticing that no matter what size of the copper clusters, S/Cu ratios always decrease upon annealing, but not by more than half of the initial value. This is due to the bifunctional nature of 1,6-hexanedithiol. Recall the studies of monothiol on copper single crystal which showed that the sulfur XPS signal almost did not change after annealing.[66] This means that any sulfur atoms that have already bound to copper should not desorb upon heating and then cause the S/Cu ratio to decrease. In this sense, the dangling dithiol motif, which is believed to evolve monothiol based on

the TPD data should be the only source of sulfur loss. It should be also mentioned that some dangling thiol groups may be oxidized or bind to the partially oxidized copper clusters, as is indicated in Figure 2.7 (a). However, in neither of these two situations, the sulfur atoms directly bind to the copper atoms. In this sense, the unattached thiol groups on the dangling ligands, no matter they are oxidized or not, should eventually cause the S/Cu ratio to decrease. If the thiol groups are somehow oxidized and also attached to the partially oxidized copper clusters, the disproportionation reaction, which can happen upon heating, may also cause some fraction of sulfur being left on the copper clusters.[88] However, the overall differences in the evolution of S/Cu ratio between the Cu_{50} and the Cu_{100} are mainly caused by the ratio of sulfur atoms that actually bind to the surface of the copper clusters. Therefore, it is very likely that these differences are mainly caused by the size effect.

Table 1 Estimated ligand numbers of Cu_{50} and Cu_{100} clusters.

total number of copper atoms	50	100
total number of dithiol ligand	25	21
number of dangling dithiol ligand	24	8
number of bidentate dithiol ligand	1	13

Based on the initial and final S/Cu ratios and the assumption that dangling dithiol ligands should be the only source of sulfur loss, the numbers of dangling and bidentate dithiol ligands per copper cluster can be estimated. As is shown in Table 1 Estimated ligand numbers of Cu_{50} and Cu_{100} clusters., for the total numbers of dithiol ligands, it may be surprising that a Cu_{50} cluster has even more ligands than a Cu_{100} cluster. However, if we take a further comparison between the numbers of dangling and bidentate ligands, it is actually fairly reasonable. For Cu_{50}, nearly all of the dithiol ligands are dangling; however, for Cu_{100}, the majority of the dithiol ligands are bidentate. Unlike a dangling dithiol which needs only one binding site, a bidentate dithiol must occupy two binding

sites. Moreover, the bidentate dithiol ligands have a bridge structure with larger steric hindrance, thus likely blocking some of the binding sites. Additionally, it is likely that a smaller cluster, such as Cu_{50}, tends to have more dangling dithiol ligands, while a larger cluster, such as Cu_{100}, tends to have more bidentate dithiol ligands. As results, with more bidentate dithiol molecules binding to a Cu_{100} cluster, it ends up with fewer dithiol ligands compared to a Cu_{50} cluster. The structural properties of Cu_{50} and Cu_{100} clusters have also been reported using Monte Carlo simulations.[89] According to this study, there are 37 surface atoms for Cu_{50}, and 65 surface atoms for Cu_{100}.[89] Based on these numbers, the surface S/Cu ratio for Cu_{50} and Cu_{100} are estimated to be 70% and 50%, respectively.

2.4 Conclusion

This work highlights a unique method to synthesize and analyze small ligated metal clusters. The mass-selected soft-landing method makes it efficient to prepare small copper clusters of desired size. The LNMD method can limit the cluster-cluster interactions and maximize the opportunity for dithiol molecules to ligate to the copper clusters. The as-prepared dithiol ligated copper clusters supported on HOPG can be further analyzed though TPD and XPS.

This work has also filled a gap of cluster size in the field previously studied for the copper alkanethiol system. Copper single crystals have been serving as the model system to study copper thiol interactions, and simple short chain monothiols have been the major thiol candidates. This work focuses on the interactions between small copper clusters (i.e. Cu_{100}) and a six-membered bifunctional dithiol (1,6-hexanedithiol). The TPD profiles have shown interesting properties of how 1,6-hexanedithiol ligate and decompose on the small copper clusters. Two different binding motifs (dangling and bidentate) of dithiol ligands have been proposed. Upon heating, three different thiol or hydrocarbon products evolve though C-S bond scission. A monothiol is ascribed to evolve from the dangling motif. Hexane and cyclohexane are assigned to evolve from the bidentate motif though

hydrogen recombination and intramolecular coupling, respectively. Temperature varied XPS measurements have revealed a similar evolution of the sulfur oxidation states to that of the copper single crystal studies. XPS measurements have shown that after being exposed to air, the dithiol ligands can partially protect the small copper clusters from being oxidized.

This work offers a fundamental understanding of the interactions between small copper clusters and bifunctional 1,6-hexandithiol molecules, which may be useful in designing the building blocks of 2-D functional materials.

3. Decomposition of Dimethyl Methylphosphonate on Size-Selected Clusters

Abstract

Room temperature decomposition and thermal decomposition of dimethyl methylphosphonate (DMMP), a chemical warfare agent (CWA) simulant, on size-selected copper clusters have been studied via combined X-ray photoelectron spectroscopy (XPS) and temperature programmed desorption (TPD). Cu_{100} and $(CuO)_{80}$, which have the same nominal masses, were chosen to present a direct comparison between the reactivity of metallic copper and that of cupric oxide with DMMP. Room temperature XPS results have shown that most of the DMMP molecules decompose completely and reductively into atomic phosphorus on Cu_{100}, while almost all the DMMP molecules are only dissociatively adsorbed on $(CuO)_{80}$ as methyl methylphosphonate (MMP). XPS and TPD have been carried out to analyze the thermal decomposition of adsorbed DMMP by identifying the surface species after annealing to certain temperatures and the gaseous products evolved during linear temperature ramps, respectively. Methanol, formaldehyde, and methane are the three most significant gaseous products for DMMP decomposition on both Cu_{100} and $(CuO)_{80}$.

Methanol and formaldehyde, which evolve in the low temperature region, are believed to originate from surface methoxy species. Methanol, formaldehyde, and methane evolved in the high temperature region are related to further decomposition of the phosphorus-containing surface species. A set of methanol-probed TPD experiments have also been carried out, which suggest that methane evolution originates from the methyl group within DMMP instead of the surface methoxy species.

3.1 Introduction

Synthetic organophosphonates ubiquitous in the agricultural, chemical, and pharmaceutical industries.[90] One group of organophosphonates, which are especially notorious, are chemical warfare agents (CWAs).[91] Dimethyl methylphosphonate (DMMP) is a commonly used simulant for one of those highly toxic CWAs, i.e., sarin, and it has been used extensively during the development of sensors and the study of catalytic decomposition processes.[92-93] DMMP and many other similar pesticide molecules are also studied in the field of environmental chemistry.[94-96] Due to high perseverance, toxicity, and potential for bioaccumulation, their removal is imperative.[97] To this end, developing a more fundamental understanding of how DMMP decomposes on different surfaces is highly imperative.

The adsorption and decomposition chemistries of DMMP have been studied on an extensive library of metal oxide surfaces, such as Al_2O_3[98-101], SiO_2[102-104], TiO_2[105-112], CeO_2[113-115], WO_3[108, 116], MoO_2[117], MoO_3[40, 118-119], Fe_2O_3[101, 105, 113], CuO[120], Cu_2O[121] and so on. On most of these metal oxide surfaces, DMMP first adsorbs via its phosphoryl oxygen (P=O) at the coordinatively unsaturated metal ion sites or on surface hydroxyls at relatively low temperature (typically below room temperature).[93, 103, 105, 108, 112, 117] The P=O bond can convert to a bridging O-P-O moiety at near room temperature.[112, 115] Adsorbed DMMP can then undergo stepwise elimination of methoxy groups upon heating.[100, 108, 111] The formation of methyl methylphosphonate (MMP) and surface methoxy

species via P-OCH_3 bond scission is commonly seen as the first decomposition step on many metal oxides.[98, 108, 111, 117] The P-CH_3 bond usually stays intact before scission of the two P-OCH_3 bonds within one DMMP molecule[108]. However, exceptions have been reported for DMMP decomposition on CuO and Cu_2O surfaces, both of which have shown room temperature P-CH_3 scission.[120-121] In evidence that a small portion of adsorbed DMMP can decompose completely into atomic phosphorus on Cu_2O[121], but not on CuO[120], suggests that the oxidation states of metal ions in metal oxide materials can have significant effects on their reactivity towards DMMP.

Besides metal oxides, DMMP adsorption and decomposition studies have also been done on single crystal surfaces, such as Ni(111)[122], Pd(111)[122], Pt(111)[123], Rh(111)[124], and Mo(111)[125]. Metallic copper has been investigated in the form of copper clusters and films supported on TiO_2(110)[126], as well as Cu/TiO_2 composite aerogels[127]. However, the sample preparation procedures in these two studies may have produced a copper oxide layer on top of the metallic copper. As a result, these two studies have shown some similarities to the work done on pure CuO, Cu_2O and TiO_2 surfaces. Considering the fact that copper oxide surfaces have shown unique reactivities towards DMMP, while the actual reactivity of metallic copper remains unclear, a direct comparative study between metallic copper and copper oxide is desirable.

Ultrasmall clusters, which have high surface-to-volume ratios and a high percentage of low-coordinated metal atoms on the surface, have unique physical and chemical properties that are distinct from their macroscopic counterparts. Numerous studies have highlighted the ability of the cluster deposition method to explore the reactivity of ultrasmall clusters, with different sizes and composition, supported on a given substrate.[41] In this work, Cu_{100} and $(CuO)_{80}$ clusters were size-selected and deposited onto a highly oriented pyrolytic graphite (HOPG) substrate, where they were exposed to DMMP. Combined X-ray photoelectron spectroscopy (XPS) and temperature programmed desorption (TPD) characterizations were carried out to analyze the room temperature decomposition and thermal decomposition of DMMP, respectively. Based on this direct

comparison between metallic copper and cupric oxide in cluster forms, the rather significant effect that the metal oxidation state within the clusters can have on their reactivity towards DMMP is demonstrated and the unique reactivity of Cu_{100} is highlighted.

3.2 Experimental

3.2.1 Formation and Deposition of Clusters

Copper and copper oxide cluster anions were generated in a magnetron sputtering source. After acceleration, mass selection and deceleration, the clusters were then deposited (soft-landed, <1 eV/atom) onto an HOPG substrate (Bucker, ZYB grade, 12·12 mm^2, 2 mm thickness) under ultra-high vacuum (UHV, base pressure $5 \cdot 10^{-9}$ torr).

In the magnetron sputtering source, a copper sputtering target (Kurt J. Lesker Co, 99.99%) was placed in front of a circular magnet and biased by up to -500V, where a mixture of argon (Airgas, 99.999%) and helium (Airgas, 99.999%) with a ratio of 1:1-1.2 (Ar/He) was introduced. Argon gas was ionized to create argon cations, which sputtered the metal target to produce a plasma. Helium served to cool and transport the cluster anions down the beamline. Anionic clusters were first electrostatically accelerated to 500 eV and then entered a magnetic sector mass filter (25° sector magnet with resolution of $m/\Delta m = 20$). By tuning the magnetic field strength, a beam of Cu_n^- cluster anions of desired size was mass-selected. The size-selected cluster anions were then deflected and focused into the deposition chamber, where they were decelerated and finally soft-landed onto the HOPG substrate. $(CuO)_n^-$ clusters were generated, transported, and deposited in the same manner, with the addition of oxygen into the Ar/He mixture via a dosing valve (INFICON VDH016-x) with an oxygen (Airgas, 99.994%) backing pressure of 15 psi. By reducing the dosing to a negligible pressure and lowering the oxygen backing pressure to 5 psi, $(CuO_{1-x})_n^-$ clusters were generated for comparative experiments. Cu_n^- ($n=100\pm5$), $(CuO)_n^-$ ($n=100\pm4$), and $(CuO_{1-x})_n^-$, which all have the same atomic mass range, were selected via the magnetic sector with the same settings. Once

deposited on the surface, the anionic clusters lost their negative charges to form neutral species. For the convenience of expression, Cu_{100}, $(CuO)_{80}$, $(CuO_{1-x})_n$ are used in the rest of this article to denote these three groups of clusters with the same confined mass range.

During a deposition process, the deposition current was monitored by a picoammeter, and the coverage of the as-deposited clusters was given in current (ampere, A) integrated over time (second, s). For each deposition, the average deposition current was about 70 pA, corresponding to an average flux of $4 \cdot 10^8$ clusters per second; and the final deposition amount was controlled to be $1 \cdot 10^{-6}$ A·s, corresponding to a total amount of $6 \cdot 10^{12}$ clusters.

3.2.2 Temperature Programmed Desorption (TPD)

TPD experiments were carried out via the liquid nitrogen matrix deposition (LNMD) method. This method was originally inspired by the common experimental technique used in matrix isolation infrared spectroscopy.[44] It was then adopted to probe the activities of metals or metal oxides towards a reactive matrix.[50] In our lab, the LNMD method was successfully implemented in order to probe the ligation and decomposition process of 1,6-hexanedithiol on size-selected Cu_{100} clusters.[24]

Prior to cluster deposition, the HOPG substrate was cleaved under ambient conditions right before being transported into a load-lock chamber and then into a UHV chamber. The substrate was then annealed at 500ºC for 30 minutes. This preparation step was proven to be adequate to obtain a relatively low background in a control TPD run, in which no clusters were deposited while all the other experimental conditions remained the same. The as-prepared HOPG was then cooled down and maintained at -170ºC by a liquid nitrogen reservoir. DMMP (Sigma Aldrich, 97%) was degassed and purified by three freeze-pump-thaw cycles before being dosed into the vacuum chamber through a UHV compatible leak valve. The dose of DMMP was monitored by a pressure gauge and a residual gas analyzer (RGA) (Hiden HAL/3F PIC quadrupole mass spectrometer

(QMS)). The dose amount was $1x10^{-8}$ Torr for 100 seconds, i.e., 1 Langmuir (L, 10^{-6} Torr·s), which was sufficient to form a frozen multilayer matrix of DMMP on HOPG at -170 ºC. After dosing, size-selected clusters were deposited into the pre-made frozen DMMP matrix.

After cluster deposition, the sample was ramped from -170ºC to 25 ºC by resistive heating to remove the physi-adsorbed DMMP. Once warmed up to 25 ºC, DMMP had likely been irreversibly adsorbed by the clusters, while most unreacted DMMP had already been physi-desorbed. TPD was then carried out to characterize the thermal decomposition properties of DMMP on the size-selected clusters. The gaseous decomposition products were detected and identified via a residual gas analyzer (RGA), which was positioned normal to the plane of the substrate at a distance of about 5 mm. Moreover, the entrance of the RGA is covered by a glass shroud with a 6 mm diameter hole cut at the center. These two configurations can both help to minimize the contributions from background gases and maximize the sensitivity toward the species desorbing directly from the substrate. Regarding the customized TPD sample holder, two small pieces of tantalum foil are wrapped on two copper power feedthroughs to allow for resistive heating, where the HOPG substrate is held. A k-type thermocouple joint is spring-loaded to the back of the HOPG for temperature measurement and ensuring a linear heating ramp.

3.2.3 X-ray photoelectron spectroscopy (XPS)

The method by which DMMP binds and decomposes on copper and copper oxide clusters was characterized via XPS with non-monochromatic Mg Kα-rays (1253.6 eV), and a hemispherical analyzer (Perkin-Elmer PHI 5100 10-360). For XPS measurements at varied temperatures, the sample was heated to certain critical temperatures and then cooled back down to room temperature, at which point XPS spectra were acquired. All the XPS spectra were calibrated by graphite C 1s at 284.5eV.[128]

The cluster source, beam line, cluster deposition and surface instrumentation are all within one vacuum system separated by gate valves. The sample can be transferred between two vertical manipulators by a horizontal magnetic transfer arm. More details about this apparatus are described elsewhere.[79]

3.3 Results

3.3.1 Room temperature XPS characterization

XPS measurements were carried out at room temperature on bare clusters as well as DMMP-adsorbed clusters to elucidate how DMMP reacts differently between copper and copper oxide clusters. Figure 3.1 (a) shows Cu $2p_{3/2}$ XPS spectra for the bare clusters. Specifically, the spectrum for $(CuO)_{80}$ has a broad main peak at around 934.2 eV and a strong satellite feature in the range of 940-950 eV, which confirms the majority of the Cu atoms should be in Cu^{2+} oxidation state. Whether or not a small amount of Cu^0 or Cu^{1+} also exists is not clear based on Cu $2p_{3/2}$ XPS spectrum alone. By contrast, the spectrum for Cu_{100} has a much narrower peak with a lower binding energy at around 933.7 eV, indicating a Cu^0 or Cu^{1+} oxidation state. Moreover, the spectrum in the middle, which has no obvious satellite peak, confirms no evident existence of a Cu^{2+} oxidation state above the detection limit. Additionally, the black vertical line in Figure 3.1 (a), which marks the approximate peak positions for Cu_{100}, indicates that the clusters corresponding to the middle spectrum may have an intermediate oxidation state between what have been observed for (CuO_{80}) and Cu_{100}, respectively. This argument is made not solely based on the Cu 2p spectrum, but also with consideration of the clusters synthesis procedures as well as the P 2p spectra, which are discussed later on. Since there is no further evidence on whether or not the clusters exhibit purely Cu^{1+} or a mixture of different oxidation states, it is therefore denoted as $(CuO_{1-x})_n$ in this work.

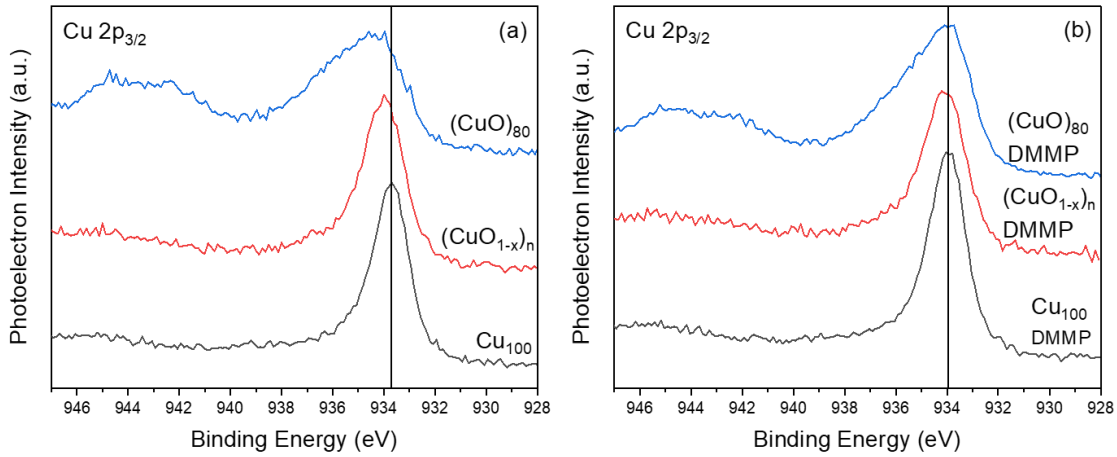

Figure 3.1 Cu $2p_{3/2}$ XPS on bare clusters and DMMP-adsorbed clusters. (a) Cu $2p_{3/2}$ XPS on bare $(CuO)_{80}$ (blue), $(CuO_{1-x})_n$ (red), and Cu_{100} (black). (b) Cu $2p_{3/2}$ XPS on DMMP absorbed $(CuO)_{80}$ (blue), $(CuO_{1-x})_n$ (red), and Cu_{100} (black).

How DMMP reacts differently among these three clusters with varied copper oxidation states is shown by comparing Figure 3.1 (b) to (a) for each cluster. First, the spectrum for DMMP-adsorbed $(CuO)_{80}$ in Figure 3.1 (b) shows a slightly narrower main peak and a weaker satellite feature compared to the one in Figure 3.1 (a), implying partial reduction of Cu^{2+} to Cu^{1+}. The possibility of Cu^{2+} reduction cannot be excluded here as it was done by Trotochaud et al.[120] due to low signal to noise ratio and lack of other characterization methods. Second, for DMMP-adsorbed $(CuO_{1-x})_n$, there is no obvious binding energy shift for Cu $2p_{3/2}$ relative to the bare cluster. Third, for DMMP-adsorbed Cu_{100}, the Cu $2p_{3/2}$ peak shifts to a slightly higher binding energy, suggesting an oxidative effect of DMMP on the copper metal clusters as compared to the copper oxide clusters. Furthermore, the two vertical lines, which mark the approximate peak positions for Cu_{100} in Figure 3.1 (a) and (b), show that the binding energy trends are different before and after DMMP adsorption. It is clearly shown that the Cu $2p_{3/2}$ binding energies from Cu_{100} to $(CuO)_{80}$ bare clusters exhibit an increasing trend (Figure 3.1 (a)). However, this increasing trend is apparently weakened for DMMP-adsorbed clusters, possibly due to oxidative effects that DMMP may have on metallic

copper clusters, as well as reductive effects that DMMP may have on cupric oxide clusters. In brief, as a result of DMMP adsorption, the binding energies of Cu $2p_{3/2}$ from these three clusters become much closer to each other. However, based on Cu $2p_{3/2}$ XPS spectra alone, no further conclusions can be drawn.

Other than Cu $2p_{3/2}$ XPS, P 2p XPS measurements of DMMP absorbed clusters can give further evidence as to how DMMP reacts differently between Cu_{100} and $(CuO)_{80}$, with $(CuO_{1-x})_n$ representing an intermediately oxidized state. As is shown in Figure 3.2 (a-c), the three P 2p spectra contain two main groups of phosphorus species marked by two vertical lines. The one with higher binding energy, centered at around 133.5 eV, is assigned to adsorbed phosphonate species. The other one, with a binding energy below 130 eV, is assigned to adsorbed atomic phosphorus. As is shown in Figure 3.2 (a), the phosphorus species on Cu_{100} are almost exclusively atomic phosphorus with only a very small amount of phosphonate species. In this sense, most of the DMMP molecules adsorbed on Cu_{100} have decomposed completely. By contrast, there is no obvious signal for any atomic phosphorus on $(CuO)_{80}$ (Figure 3.2 (c)). Instead, DMMP mainly undergoes cleavage of one P-OCH_3 bond and forms adsorbed methoxy and methyl-methylphosphonate (MMP), which is a partial decomposition process. For $(CuO_{1-x})_n$, which has an intermediate copper oxidation state, an intermediate state is also observed in P 2p XPS measurements. As is shown in Figure 3.2 (b), $(CuO_{1-x})_n$ has a fair amount of both adsorbed phosphonate species and atomic phosphorus, with the phosphonate species as the dominant adsorbate. In brief, room temperature XPS measurements have shown that Cu_{100} can lead to the complete breakdown of DMMP into atomic phosphorus while $(CuO)_{80}$ can only cause partial dissociation of DMMP into adsorbed phosphonate species.

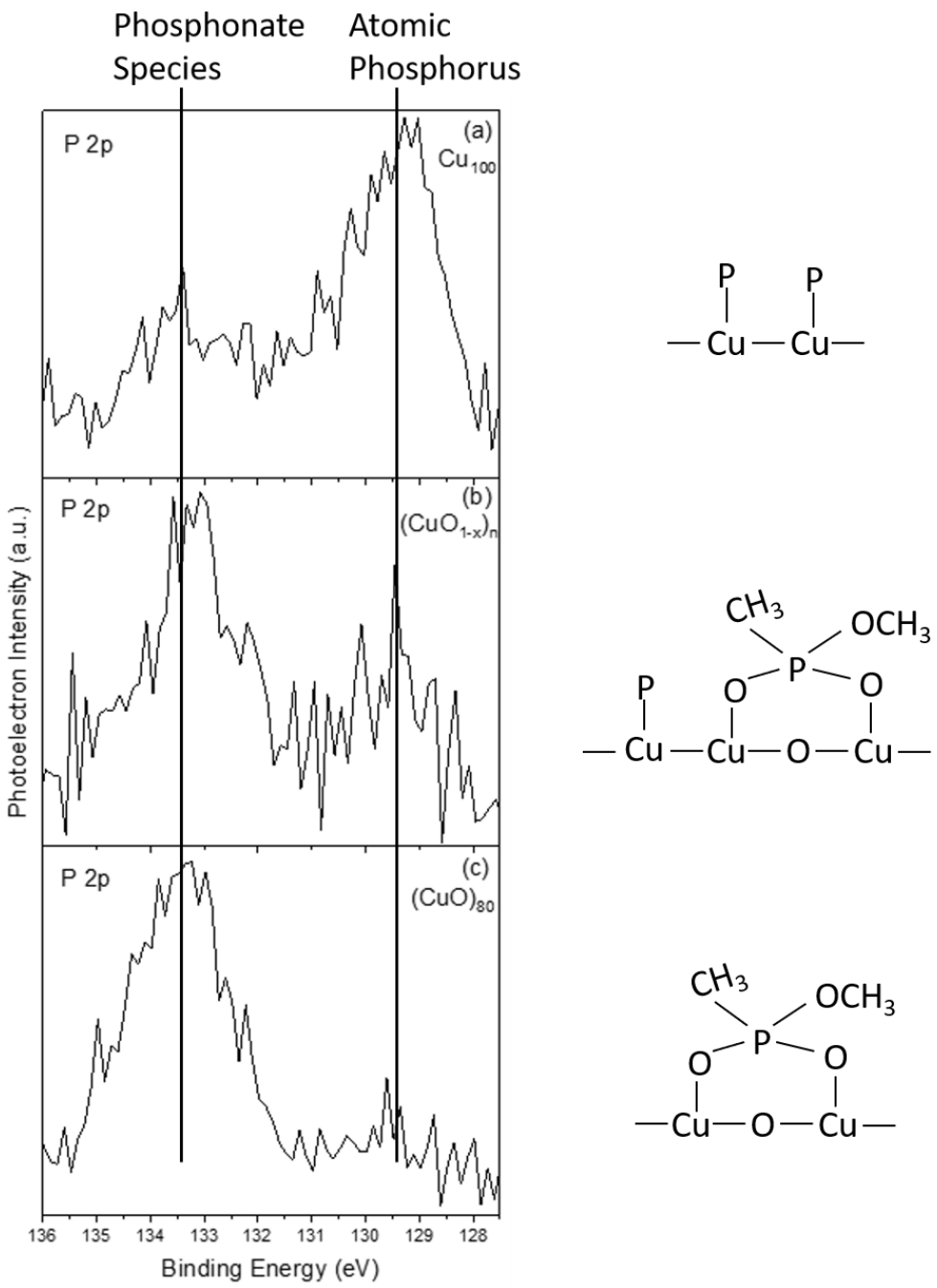

Figure 3.2 P 2p XPS on DMMP-adsorbed clusters: (a) Cu_{100}, (b) $(CuO_{1-x})_n$, (c) $(CuO)_{80}$. The two vertical lines mark the two main groups of phosphorus-containing species, which are phosphonate species and atomic phosphorus. The corresponding diagrams are shown on the left for each cluster.

3.3.2 XPS characterization after heating to certain temperatures

It is known that DMMP can undergo further decomposition at elevated temperature. Therefore, XPS spectra, which were collected after heating the sample to certain temperatures and then cooling back down to room temperature, are shown here to compare the thermal decomposition processes of DMMP on Cu_{100}, and $(CuO)_{80}$.

For the Cu $2p_{3/2}$ spectra, after heating to 200 °C or beyond, there is no obvious change in either peak position or peak shape (Figure 3.3 (a)). For $(CuO)_{80}$, the major change only occurs when annealed to 200 °C (Figure 3.3 (b)). The facts that the satellite features disappear and that the main peak becomes narrower and shifts to a lower binding energy indicates the reduction of the majority of Cu^{2+} to Cu^{1+}. Similarly, there is no obvious change after annealing to 300 °C and 400 °C.

For the P 2p spectra, the major difference between Cu_{100} and $(CuO)_{80}$ remains in the low binding energy region from 128 eV to 131 eV. As is shown in Figure 3.3 (c), the vertical line marks the low binding energy area, which is mainly atomic phosphorus on Cu_{100} for all four annealing temperatures. By contrast, there is no obvious atomic phosphorus peak for $(CuO)_{80}$ (Figure 3.3 (d)). As for the high binding energy region from 131 eV to 135 eV, the P 2p peaks for both Cu_{100} and $(CuO)_{80}$ share a similar trend with incremented temperatures, despite a great difference in peak intensity. As is shown in Figure 3.3 (c) and (d), the two diagonal lines mark the two similar rising binding energy trends with incremented temperatures. Because of the abundance of phosphonate species on $(CuO)_{80}$, it is clearly shown that the major binding energy shift happens upon heating to 200 °C. After heating to 300 °C, there is no obvious change in the peak position. Even so, given that the peak position shifted to the highest binding energy for 400 °C, the overall trend in binding energy shift is still an increase with incremented temperatures. Similarly, the weak phosphonate peaks for Cu_{100} also shift to higher binding energies after annealing (Figure 3.3 (c)).

In short, XPS measurements after heating to certain temperatures have shown that atomic phosphorus formed due to complete decomposition of DMMP is only observed for Cu_{100}, and that phosphonate species formed due to partial dissociation of DMMP is observed in a large extent on $(CuO)_{80}$ and only a minor extent on Cu_{100} at room temperature, with further decomposition observed at elevated temperatures.

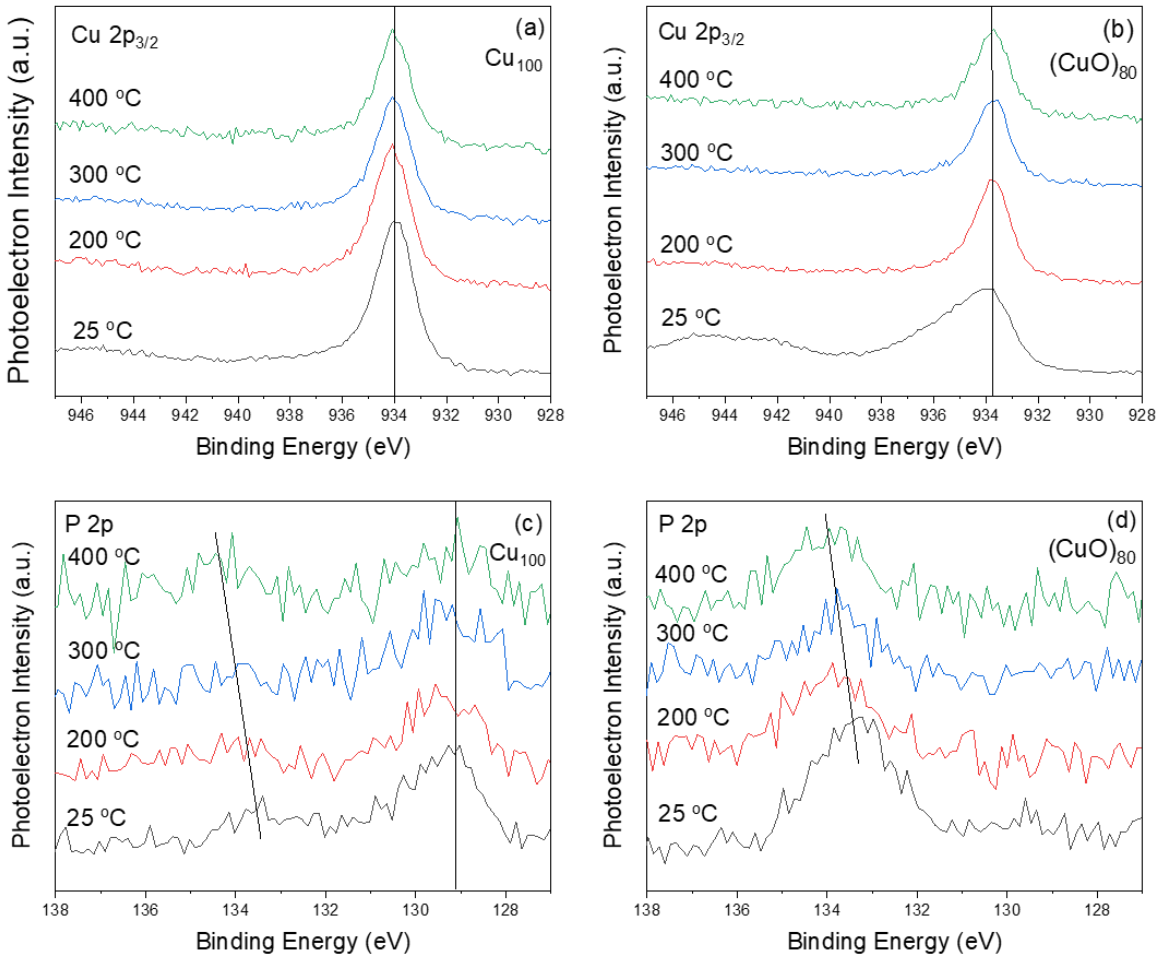

Figure 3.3 XPS of Cu $2p_{3/2}$ and P 2p for DMMP-adsorbed Cu_{100} and $(CuO)_{80}$ clusters at 25 °C and after heating to 200 °C, 300 °C, and 400 °C: (a) Cu $2p_{3/2}$ XPS for DMMP-adsorbed Cu_{100}; (b) Cu $2p_{3/2}$ XPS for DMMP-adsorbed $(CuO)_{80}$; (c) P 2p XPS for DMMP-adsorbed Cu_{100}; (d) P 2p XPS for DMMP-adsorbed $(CuO)_{80}$. For all four graphs, spectra are presented from bottom to top in order of increasing temperature, which are color coded as 25 °C (black), 200 °C (red), 300 °C (blue), 400 °C (green). Vertical and diagonal

lines in all the graphs, which mark the approximate peak positions, show the binding energy shifting trends with incremented temperatures.

3.3.3 Temperature-programmed desorption (TPD)

The gaseous products formed during the thermal decomposition processes of DMMP on Cu_{100} and $(CuO)_{80}$ clusters were studied via TPD. Several DMMP fragments and likely reaction products were monitored. The three major products are plotted in Figure 3.4 after being corrected for fragmentation. More details on the correction process are described in the Supporting Information (SI).

As is shown in Figure 3.4 (a) and (b), methanol, formaldehyde and methane are the three major gaseous products for both Cu_{100} and $(CuO)_{80}$. There are apparently two desorption regions: the low temperature region from 120 ºC to 220 ºC, and the high temperature region from 220 ºC to 320 ºC. For Cu_{100}, the methanol spectrum has a rising shoulder feature culminating in a peak, which coincides with formaldehyde in the low temperature region. In the high temperature region, methane evolves at a slightly lower temperature than that of the second peak of formaldehyde. For $(CuO)_{80}$, the peaks of all three products occur in the high temperature region, with methanol and formaldehyde having rising shoulder features in the low temperature region. By comparison, both Cu_{100} and $(CuO)_{80}$ have a methane peak and a formaldehyde peak in the high temperature region, while the major differences lie in the low temperature region, where Cu_{100} has a significant peak for both formaldehyde and methanol but $(CuO)_{80}$ only has broad shoulder features for each species.

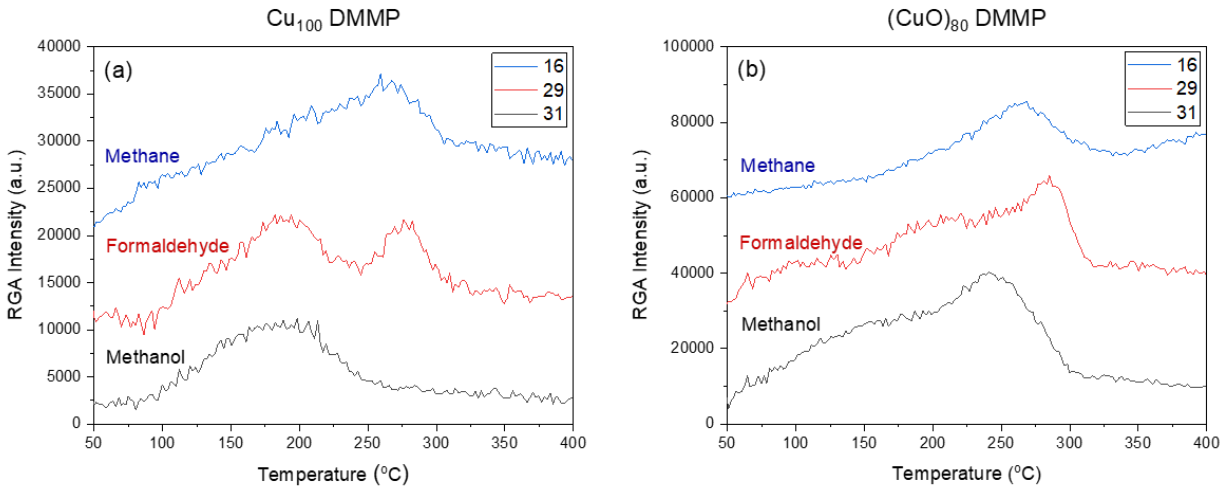

Figure 3.4 DMMP decomposes into methanol (black), formaldehyde (red) and methane (blue) on Cu_{100} and $(CuO)_{80}$ in TPD experiments. Methanol, formaldehyde, and methane are tracked by m/e of 31, 29 and 16, respectively. The traces are offset for clarity, and data has been corrected for fragmentation patterns.

3.4 Discussion

The results presented here demonstrate the unique reactivity of Cu_{100} with DMMP at room temperature when compared to that of $(CuO)_{80}$. Specifically, the fact that DMMP mainly decomposes into atomic phosphorus on Cu_{100} at room temperature is quite exceptional. At elevated temperatures, XPS and TPD offer greater details on the thermal decomposition process of DMMP on Cu_{100} and $(CuO)_{80}$. Here, we will start our discussion with the assignment of features in the XPS spectra and its limitations in identifying surface species in this study. Next, a set of methanol-probed TPD experiments will be presented to provide further insights regarding the origin of the gaseous products. Finally, a proposed reaction scheme considering both the XPS and TPD results will be discussed.

3.4.1 Assignment of features in XPS spectra

A formal peak fitting process has not been applied to the P 2p spectra due to low signal-to-noise ratio. Since size-selected cluster deposition experiments generally have prepared samples with low cluster coverage, and phosphorus has a low relative sensitivity factor, it is expected that the signal intensity for P 2p XPS should be very low. Therefore, no specific binding energy for phosphorus species has been reported here to avoid overinterpretation of the data. Instead, rational speculations have been drawn for the low (128-130 eV), middle (130-133 eV), and high (133-135 eV) binding energy range. It is generally accepted that phosphorus species with fewer oxygen-containing coordinated groups tend to have lower P 2p binding energies.[31] Accordingly, those phosphorus species, which have no coordinated oxygen, usually have the lowest binding energies. For example, a binding energy of 128.5 eV was reported for atomic phosphorus on copper clusters supported on TiO_2(110).[126] Similarly, the low binding energy peak is assigned as mostly atomic phosphorus on Cu_{100}. Moreover, Lai et al. demonstrated a stepwise dealkylation of PR_3 (R is methyl or ethyl) on Cu(110), showing that PR_3, PR_2 and PR have P 2p binding energies of 131.6 eV, 130.8 eV and 129.6 eV, respectively.[129] Considering that DMMP only has one methyl group to begin with, even though there is no discernable peak feature in the middle binding energy area, it is speculated that there may be some surface -PCH_3. Furthermore, a surface-bound phosphinate group [O=PH(OCH_3)O-Cu] with a binding energy of 132.5 eV was identified for DMMP decomposition on polycrystalline cuprous oxide surfaces at room temperature.[121] Even though there is no discernable feature in the middle binding energy area, it is speculated that there may be an analogous phosphinate group. These arguments are discussed further in the following sections.

DMMP physisorbed on different metal oxides was reported to be in the range of 134.0-135.0 eV, while chemisorbed DMMP was reported to have a slightly lower binding energy.[121] In this work, the binding energy of P 2p for molecular DMMP was also measured in the form of a frozen DMMP matrix on HOPG without any clusters. As is shown in Figure 3.6, intact DMMP has a binding

energy of 134.2 eV, while the peak positions in the high binding energy range shown in Figure 3.3 (c) and (d) are clearly below 134 eV. Methyl methylphosphonate (MMP), which is a dissociative adsorption product of DMMP, was identified on metal oxides with binding energies lying in the range of 132.8-133.8 eV.[40, 120-121] Moreover, extensive IR studies have provided direct evidence for the formation of MMP and surface-adsorbed methoxy groups at or below room temperature on other metal oxide surfaces.[112] Therefore, the peak feature in the high binding energy area at room temperature is assigned to mostly MMP.

Upon heating to 200 ºC, there is no obvious change in low and middle binding energy range. In the high binding energy range, the peak position shifts to an even higher binding energy. It is speculated that the decomposition of both phosphinate and MMP may contribute to the formation of PO_x through P-O bond and P-C bond scission, which has been proposed in a study of DMMP decomposition on a Cu_2O surface.[121] Moreover, potential surface-bound -PCH_3 is speculated to decompose into atomic phosphorus via P-C bond cleavage upon heating to 200 ºC. However, this phenomenon was not observed at all in the work on Cu_2O. In fact, atomic phosphorus disappeared completely on Cu_2O after heating to 160 ºC.[121] In this sense, the abundance and accumulation of atomic phosphorus in this work are attributed to the unique reactivities of metallic copper in Cu_{100}.

Once annealed to 300 ºC, the two peaks lying within the low and high binding energy range seem to be more ambiguously separated from each other, indicating other types of phosphorus-containing species may have formed in the middle binding energy range. It is speculated that oxidative decomposition of -PCH_3 and oxidation of atomic phosphorus can both give rise to the increased signal intensity detected in the middle binding energy range. This may seem contradictory, because -PCH_3 is believed to partially decompose into atomic phosphorus after heating to 200 ºC, which is a reductive process. A reasonable explanation is that the residual water and oxygen in the chamber can cause oxidation during the heating and cooling processes for XPS experiments, which usually last several hours. The higher the ultimate temperature attained, the

longer the experiment has lasted, thus leading to the higher degree of oxidation. This can also explain why the atomic phosphorus peak is further weakened, and the PO_x peak becomes even stronger at 400 ºC. It is also reasonable to speculate that the surface phosphorus species lying in the middle binding energy range at 300 ºC may undergo further oxidation into PO_x during the heating process from 300 ºC to 400 ºC. After annealing to 400 ºC, only PO_x and atomic phosphorus are present due to their relatively higher thermodynamic stability.

Unlike Cu_{100}, there is no obvious peak in the low binding energy range for $(CuO)_{80}$. At room temperature, the main peak in the high binding energy range is assigned to MMP, which has also been identified on polycrystalline CuO surfaces.[120] The very weak peak feature in the low binding energy range can be explained by the existence of a small amount of atomic phosphorus or the satellite features for Cu 3s. Recalling the fact that both Cu_{100} clusters and polycrystalline Cu_2O can give rise to complete decomposition of DMMP into atomic phosphorus at room temperature, the presence of a trace amount of atomic phosphorus here indicates that some residual Cu^0 or Cu^{1+} may have played a role within the size-selected $(CuO)_{80}$ clusters. It should be noted that the main peak of a typical Cu 3s spectrum lies in the range of 123.0-124.0 eV, and that Cu 3s spectra in Cu^{2+} compounds have satellite features that lie in the range of 3 to 10 eV higher in binding energy relative to the main peak. In this sense, the satellite features of Cu 3s in the $(CuO)_{80}$ Cu 3s spectrum can overlap with the P 2p peak region, especially the low binding energy range for atomic phosphorus. Due to the limitation of low signal-to-noise ratio, neither of these two explanations can be ruled out.

After heating to 200 ºC, it is clearly shown that the low binding energy feature has vanished and the MMP peak has shifted slightly to higher binding energy. It should be mentioned that Cu^{2+} in bare $(CuO)_{80}$ clusters can be reduced completely to Cu^{1+} upon annealing to 200 ºC under UHV (Figure 3.3 (b)). Moreover, multiple studies have shown that lattice oxygen in CuO can participate in dissociative adsorption and oxidative decomposition processes at room temperature and elevated

temperatures for many organic molecules such as DMMP[120], methanol[130-131], and alkanethiols.[24, 74] Therefore, the disappearance of low binding energy feature can be ascribed to the oxidative effects on potential atomic phosphorus from the activated lattice oxygen within $(CuO)_{80}$ as well as the loss of satellite feature of Cu 3s due to reduction of Cu^{2+} into Cu^{1+} upon heating to 200 ºC.

As for the peak in the high binding energy range, which is persistent from 200 ºC to 300 ºC with only a minor shift in binding energy, it is speculated to arise from phosphorus oxide species with one methoxy or methyl group. The fact that the peak at 200 ºC seems broader than the one at room temperature indicates the co-existence of multiple similar surface-bound species at 200 ºC. Since these surface species are likely to have binding energies very close to each other, it is impossible to differentiate them from each other via peak fitting process. It has been reported that accumulation of a phosphate layer with a stoichiometry similar to P_2O_5 occurs after the removal of all carbonaceous species via annealing of polycrystalline Cu_2O.[121] Considering the TPD results which have shown all carbonaceous products evolve in the temperature range of 120 ºC to 320 ºC, the peak for 400 ºC, which is located at around 134 eV, is assigned as PO_x.

3.4.2 Insight into the reaction mechanism from TPD experiments

Stepwise elimination of methoxy and methyl groups has been reported to be a common feature in the DMMP decomposition pathway.[91] It is usually the case that these groups leave the surface in the gas phase as, for example, methanol, formaldehyde, methane, and/or dimethyl ether.[40, 115, 126, 132-133] In this work, methanol, formaldehyde and methane are all identified as gaseous products upon heating for both Cu_{100} and $(CuO)_{80}$. The frozen matrix of DMMP sublimes from HOPG at -110 ºC, and the monolayer desorbs at around -50 ºC (Figure 3.7). Background TPD experiments as well as the Cu/P ratio calculated from XPS spectra both indicate that there is no obvious phosphorus-containing species desorbed from the clusters. More details are addressed in the SI.

In the low temperature region for Cu_{100}, the coincidence of methanol and formaldehyde at around 180 °C is attributed to the disproportionation reaction of surface methoxy (Figure 3.4 (a)). The low temperature shoulder feature for methanol suggests that the methoxy groups tend to desorb as methanol by reacting with surface hydroxyls before the disproportionation reaction becomes a competitive pathway. Unlike Cu_{100}, $(CuO)_{80}$ has no obvious peak in the low temperature region. Instead, both methanol and formaldehyde have broad rising features, which are likely due to the convolution of multiple desorption peaks. It is known that lattice oxygen in CuO can be activated to oxidize surface adsorbates such as methanol into formaldehyde.[28] In this study, it is shown that the Cu^{2+} within $(CuO)_{80}$ are reduced to Cu^{1+} upon heating to 200 °C. During this process, the lattice oxygen can also be involved in the oxidation of adsorbed methoxy groups. Considering the multiple reaction pathways as well as the drastic changes in structure and composition of the $(CuO)_{80}$ clusters, it is reasonable to expect some broad rising features for methanol and formaldehyde in the TPD spectrum for $(CuO)_{80}$.

In the high temperature region, both Cu_{100} and $(CuO)_{80}$ have discernable peaks for methane and formaldehyde. It is speculated that methane and formaldehyde evolve from further decomposition of MMP instead of adsorbed surface methoxy. In order to obtain more evidence to support this claim, a set of methanol TPD experiments were performed. Methanol, which is known to undergo dissociative adsorption on a variety of metal oxides to form surface methoxy intermediates, has been successfully employed as a 'smart' surface probe to quantify surface active sites.[28] In this study, methanol is used as a probe by forming surface methoxy, which should also exist when DMMP decomposes into MMP. As is shown in Figure 3.9, there is no obvious peak for methane, which indicates that surface methoxy cannot evolve into methane under the experimental conditions in this study. Moreover, methanol has a strong desorption peak at around 50 °C for both Cu_{100} and $(CuO)_{80}$, suggesting an undissociated adsorption form for most of the detected methanol. It should be noted that the methanol peak for Cu_{100} is much broader with a long tail extending above

100 °C. This can be reasonably explained by a reversibly dissociative adsorption form, through which the methanol should desorb at a relatively higher temperature compared to the undissociated adsorption form. This reversibly dissociative adsorption form may also exist on $(CuO)_{80}$; however, the oxidation of surface methoxy can be a competing reaction pathway. As a result, formaldehyde evolves at around 80 °C, and the signal from methanol decreases drastically after peaking at 50 °C. The lattice oxygen within $(CuO)_{80}$ is believed to participate in the formation of formaldehyde, while the lack of lattice oxygen makes Cu_{100} almost inert toward methanol. These results generally agree with the single crystal studies in the literature.[36, 134-136]

3.4.3 Proposed reaction scheme based on XPS and TPD results

Combined XPS and TPD is a powerful approach to study the decomposition processes of organic molecules on size-selected clusters of interest. TPD can offer evidence on the evolution of gaseous products during the temperature ramping, while XPS acquired after heating the sample to several critical temperatures can elucidate residual species on the surface. Our group has successfully applied this method to shed light on the decomposition mechanism of several organic molecules, including DMMP, on size-selected metal and metal oxide clusters.[24, 40] Similarly, the decomposition process of DMMP on Cu_{100} and $(CuO)_{80}$ clusters has been analyzed and compared via combined XPS and TPD in this study. As is shown in Figure 3.5, a plausible DMMP decomposition scheme is presented with all the surface species and gaseous products described in the previous sections. Several important interpretations which can be mutually rationalized by both the XPS and TPD results are discussed as well.

First, insights obtained from the XPS results can explain why methanol has a different leading edge but a comparable signal intensity between Cu_{100} and $(CuO)_{80}$ in the low temperature region of the TPD spectra. Specifically, the room temperature XPS shows that the major

phosphorus-containing species on Cu_{100} is atomic phosphorus, from which no gaseous product can evolve during a TPD ramp. The weak XPS peak for MMP indicates a small amount of surface methoxy groups on Cu_{100} at room temperature. By contrast, $(CuO)_{80}$ has surface-bound MMP almost exclusively, indicating a fair amount of surface methoxy groups at room temperature. Therefore, the difference in the initial amounts of surface methoxy groups between Cu_{100} and $(CuO)_{80}$ explains why $(CuO)_{80}$ has a stronger rising shoulder feature for methanol in the low temperature region compared to that of Cu_{100}, as is shown in Figure 4. Moreover, considering that the decomposition of both phosphinate and MMP may contribute to the formation of PO_x after heating to 200 ^oC, it is reasonable to speculate that the decomposition of these two surface species may contribute to the methanol and formaldehyde formation in the low temperature region for Cu_{100}. This also helps to explain why the signal intensity of methanol and formaldehyde for Cu_{100} in the low temperature region is comparable to that of $(CuO)_{80}$, despite the fact that Cu_{100} should have much less surface methoxy groups to begin with at room temperature.

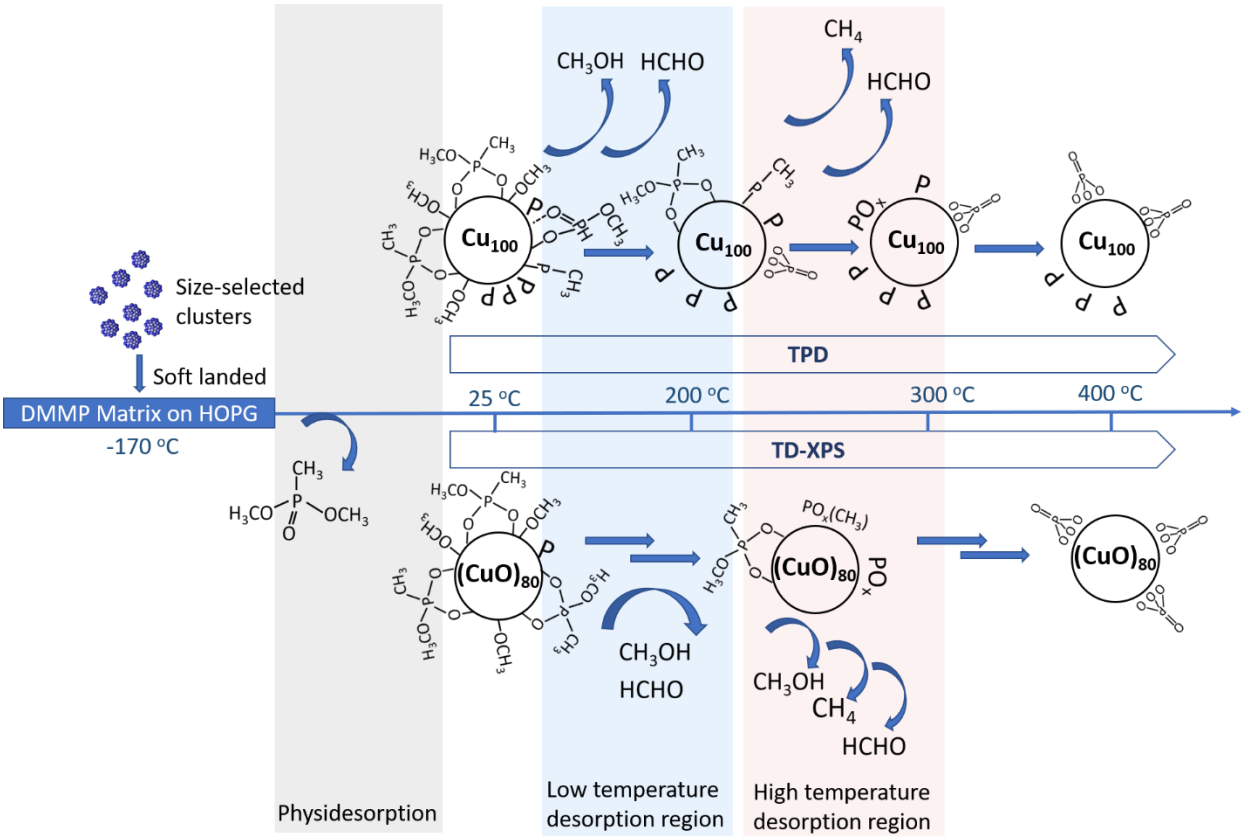

Figure 3.5 Proposed reaction scheme of DMMP decomposition on Cu_{100} and $(CuO)_{80}$.

Moreover, the differences in C 1s XPS between Cu_{100} and $(CuO)_{80}$ agree with the fact that the overall TPD signal intensity for $(CuO)_{80}$ is stronger than Cu_{100}. As is shown in Figure 3.8, for $(CuO)_{80}$, the obvious shoulder feature in the range of 286-287 eV is a strong indication for methoxy groups. The shoulder feature decreases with incremented temperatures, suggesting that those methoxy groups may evolve into gaseous products and leave the surface. By contrast, neither the shoulder feature nor its decreasing process is obviously discernable for Cu_{100}. It has been reported that the C 1s for the methoxy group within MMP is largely indistinguishable from that of methoxy groups absorbed on CuO[120]; however the methoxy group on clean Cu(110) may have a slightly lower C 1s binding energy.[135] Therefore, the C 1s XPS spectra not only provide additional evidence for the abundance of methoxy groups on $(CuO)_{80}$, but also agrees with the fact that $(CuO)_{80}$ has

stronger RGA signals for methoxy-originated gaseous products, such as methanol and formaldehyde.

Furthermore, broad peaks are expected in both XPS and TPD spectra based on fundamental considerations. Theoretical studies have shown that dynamic fluxionality can cause supported clusters to populate many distinct structural and stoichiometric states under reaction conditions.[137] Hence, the reaction interface should be viewed as an evolving statistical ensemble of many structures.[138] This theory has been exemplified by size-selected cluster catalysis experiments, in which the size-dependent properties are explained by different compositions of thermal ensembles.[4, 15] In this study, it is believed that the support (HOPG) and the absorbate (DMMP) can affect the structure of the clusters, causing the ensembles to change for all reaction intermediates. The structural dynamics can become even more complex during the heating process, when reaction intermediates can follow different reaction pathways and the lattice oxygen within $(CuO)_{80}$ is activated. Since both XPS and TPD can only provide the ensemble-average information, it is reasonable to expect that the XPS peaks are broader at elevated temperatures; and that the TPD peaks are more broadened for $(CuO)_{80}$ in the low temperature region.

Although all of the above discussion shows that our overall reaction scheme is reasonable considering the mutual agreement between the XPS and TPD results, it should be realized that the XPS results cannot be directly mapped to the TPD results. The reason is that TPD is the result of continuous measurements during a programmed linear temperature ramp, while XPS is taken at room temperature, which is a relatively thermodynamically stable state reached after prolonged heating of the sample at certain critical temperatures. The P 2p XPS does show well-separated peaks for certain surface species, especially for atomic phosphorus on Cu_{100}. However, the presence of broad peaks and low signal-to-noise ratio in the heating data makes it very hard to conclusively assign peaks. Moreover, the unresolved peaks in the TPD data also make it difficult to relate every surface species to their corresponding gaseous products. Additional characterizations, such as FT-

IR, isotopic labelling, and computational work would further validate more details in the proposed reaction scheme; however, these efforts are outside the scope of the study presented here.

3.5 Conclusions

In this work, we use combined XPS and TPD to investigate the room temperature decomposition and thermal decomposition of DMMP on size selected Cu_{100} and $(CuO)_{80}$ clusters supported on HOPG. Cu_{100} has shown remarkable reactivities towards DMMP, which is drastically different from $(CuO)_{80}$. At room temperature, the XPS results show that most of the adsorbed DMMP molecules decompose completely into atomic phosphorus on Cu_{100}, while phosphine, phosphinate and phosphonate groups may exist in only small amounts. By contrast, DMMP mainly dissociates into surface-bound MMP and methoxy species through P-OCH_3 bond scission on $(CuO)_{80}$ at room temperature, which is commonly seen on many other metal oxides. TPD results show evidence of two distinct desorption regions and that methanol, formaldehyde, and methane are the three main volatile products for both Cu_{100} and $(CuO)_{80}$. The differences between the TPD results can be correlated to the XPS results to some degree. A set of methanol probed TPD experiments, which show the desorption of formaldehyde from $(CuO)_{80}$ but not from Cu_{100} and no methane production for either cluster, suggest that lattice oxygen within $(CuO)_{80}$ is involved in thermal decomposition of DMMP and that methane originates from the methyl group within DMMP instead of the surface methoxy species.

This work highlights a unique method to synthesize small clusters and analyze their reactivities towards DMMP. The mass-selected soft-landing deposition method makes it efficient to prepare small copper and cupric oxide clusters of desired size on a prepared surface. Combined XPS and TPD offers a powerful approach to analyze the decomposition process of DMMP. The results not only add to the library of metal and metal oxide clusters studied for degradation of CWA simulants,

but also showcase how changing the metal oxidation states can affect the reactivity towards DMMP substantially. It should be emphasized that the remarkable reactivities of Cu_{100} towards DMMP at room temperature should motivate more work on metallic copper materials. Besides oxidative decomposition of CWAs, for which many metal oxide materials have been explored, reductive decomposition, which is exemplified by Cu_{100} in this work, may be another promising path.

3.6 Supporting Information

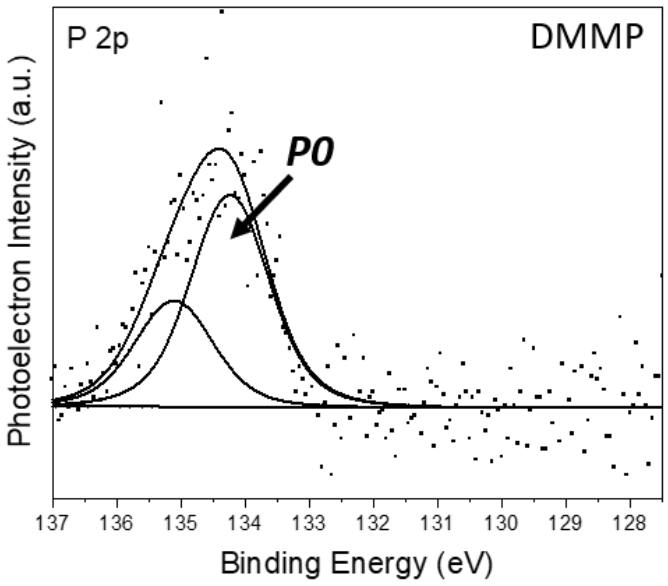

Figure 3.6 P 2p XPS of molecular DMMP in the form of a frozen matrix on HOPG at -170 °C. The P 2p3/2 peak is labeled as *P0* with a binding energy of 134.2 eV.

The data in Figure 3.6 was acquired on the newly rebuilt version of the original apparatus, on which the sample can be maintained at -170 °C for XPS measurements. The original apparatus, which was used to acquire the rest of the data in this work, was described in detail elsewhere.[79] The original apparatus can only take XPS measurements at room temperature. Since there is no obvious

sign for any physical adsorption of DMMP on HOPG without any clusters at room temperature, P 2p XPS cannot be obtained for molecularly adsorbed DMMP on the original apparatus. Since the data in Figure 3.6 was acquired on a multilayer of DMMP at cryogenic temperature, while the rest P 2p XPS in this work was done on less than 10% monolayer coverage, it is reasonable to expect that Figure 3.6 has much stronger signal intensity compared to the other P 2p spectra.

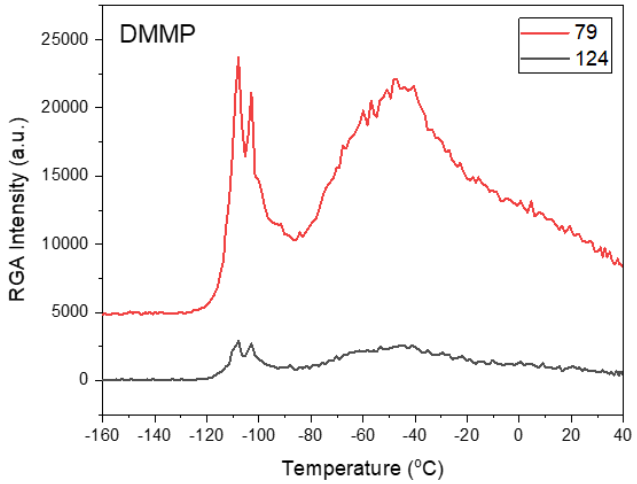

Figure 3.7 TPD spectrum of physi-desorption of a DMMP frozen matrix adsorbed on HOPG measured by m/e 124 (parent DMMP ion), and 79 (major fragment ion). The frozen matrix of DMMP consists of a DMMP multilayer. The multilayer sublimes at around -110 °C, and the remaining monolayer adsorbed on HOPG desorbs at around -50 °C.

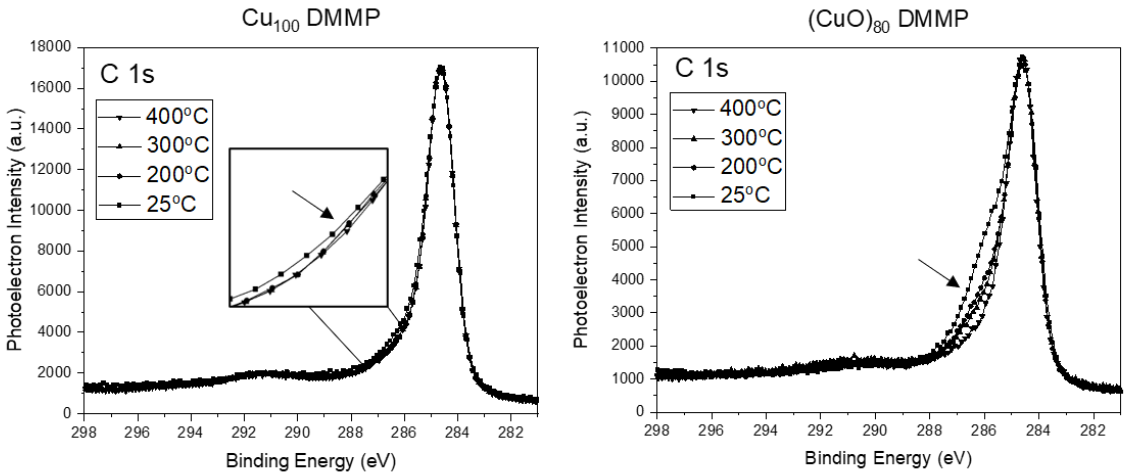

Figure 3.8 C 1s XPS for DMMP adsorbed Cu_{100} and $(CuO)_{80}$. The arrows show the direction, in which the spectra shift with incremented temperatures. The inserted picture shown in the left graph is an enlargement of the binding energy area from 286 eV to 287 eV. Data points for different temperatures are marked by different symbols: 25 ºC (■), 200 ºC (♦), 300 ºC (▲), 400 ºC (▼).

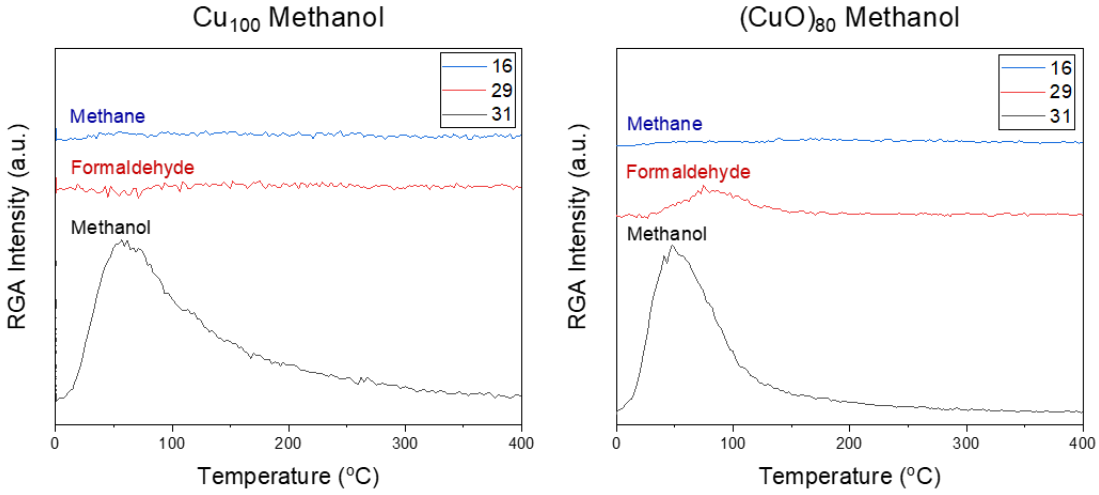

Figure 3.9 Methanol TPD experiments on Cu_{100} and $(CuO)_{80}$. Methanol (black), formaldehyde (red) and methane (blue) are tracked by m/e of 31, 29 and 16, respectively. The traces are offset for clarity and data has been corrected for fragmentation pattern.

A1. Fragmentation correction and background subtraction.

The products are identified with the QMS by considering the fragmentation pattern and the background from the sample holder. Monitored masses for the experiments with DMMP are m/e = 124, 79, 32, 31, 30, 29, 16, 15; with methanol are m/e = 32, 31, 29, 30, 16, 15. Methanol is identified by m/e of 32, 31, 30, and 29. formaldehyde are identified by m/e of 30 and 29. Methane is identified by 16.

As is described in the experimental section, the sample must be annealed to 25 ºC first, before it is brought directly in front of the RGA for a TPD run. Even though 25 ºC is believed to be high enough to remove all of the physi-adsorbed DMMP on the HOPG surface, there is still a small amount of DMMP that can desorb at around 90 ºC, possibly from the sample holder or the defects on HOPG, as is shown in Figure 3.10. Even though m/e of 32, 31, 30 and 29 also have peaks at around 90 ºC, based on the fact that they follow the trend of m/e of 79, it is believed that there is no obvious evidence for methanol or formaldehyde.

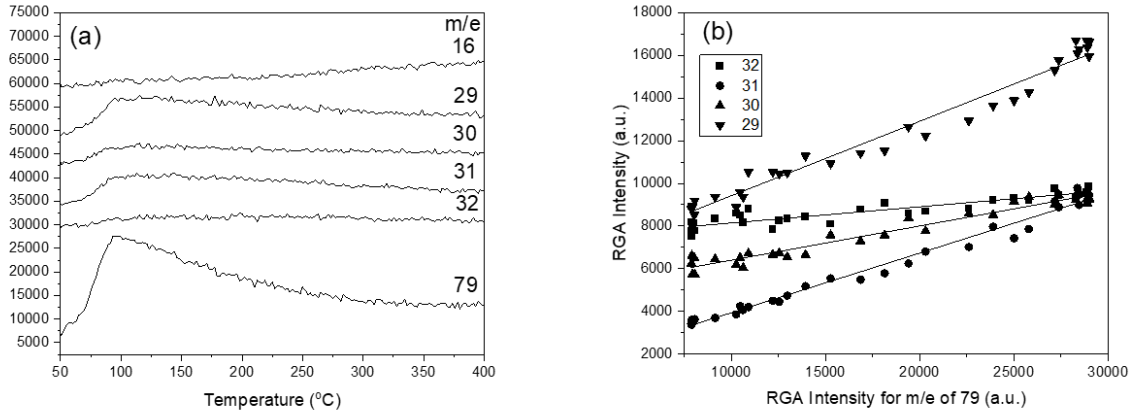

Figure 3.10 (a) Background TPD spectra obtained after annealing the sample at 25 ºC to remove all the physisorbed DMMP. No cluster was deposited in this case. (b) Linear fitting for m/e of 32, 31, 30, and 29 to m/e of 79 in the low temperature range from 50 ºC to 90 ºC.

The raw data for experimental TPD as is shown in Figure 3.11 (a), which is taken after cluster deposition into the frozen matrix of DMMP, also have low temperature peaks analogous to

the background experiment. In the low temperature region from 50 ºC to 90 ºC, m/e of 32, 31, 30, and 29 are well linearly fitted to m/e of 79. Therefore, the spectra for m/e of 32, 31, 30, 29 are corrected by m/e of 79 using the ratio determined in the linear fitting. The TPD spectrum for $(CuO)_{80}$ DMMP is also corrected in the same way. The ratios tend to deviate among experiments carried out in different days, which is possibly due to some slight change in the filament conditions and differential pumping conditions in the RGA.

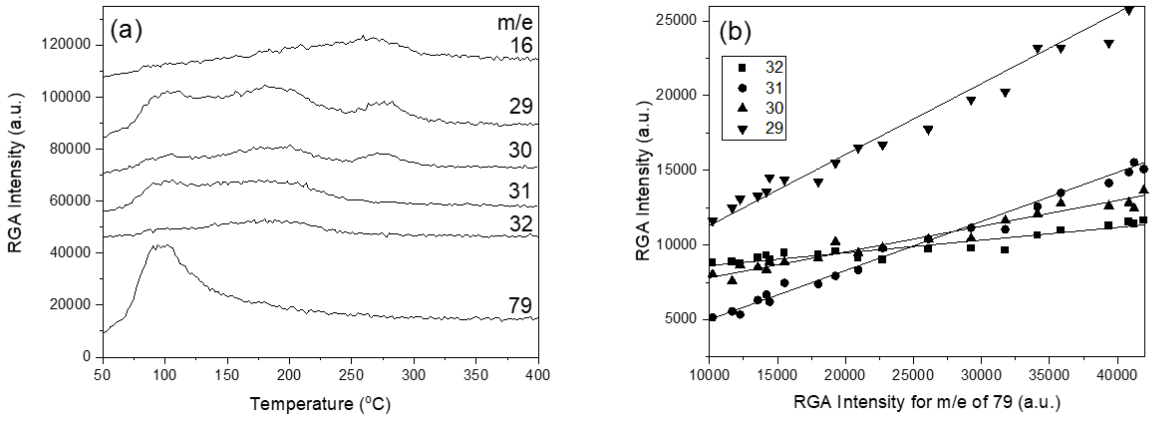

Figure 3.11 (a) Raw TPD spectrum for Cu_{100} DMMP. (b) Linear fitting for m/e of 32, 31, 30, and 29 to m/e of 79 in the low temperature range from 50 ºC to 90 ºC.

It should be noted that DMMP, methanol and formaldehyde all contribute to m/e of 30 and 29. As is shown in Figure 3.11, DMMP only has its contribution below 150 ºC, but methanol has its contribution extending to 250 ºC. The correction for m/e of 30 and 29 were done using the ratio determined by the methanol TPD experiments. Since the signal intensity for m/e of 30 and 29 are relatively stronger compared to that for m/e of 32 and 31, this correction does not change the spectrum in a qualitative manner.

For the methanol TPD experiments, the correction for m/e of 30 and 29 can make a huge difference. As is shown in Figure 3.12 (a) and (c), it is not obvious to see the difference between

Cu_{100} and $(CuO)_{80}$ in terms of methanol decomposition. However, when plotting m/e of 31, 30 and 29 to 32, it is apparent that there is formaldehyde desorption for $(CuO)_{80}$ but not for Cu_{100}.

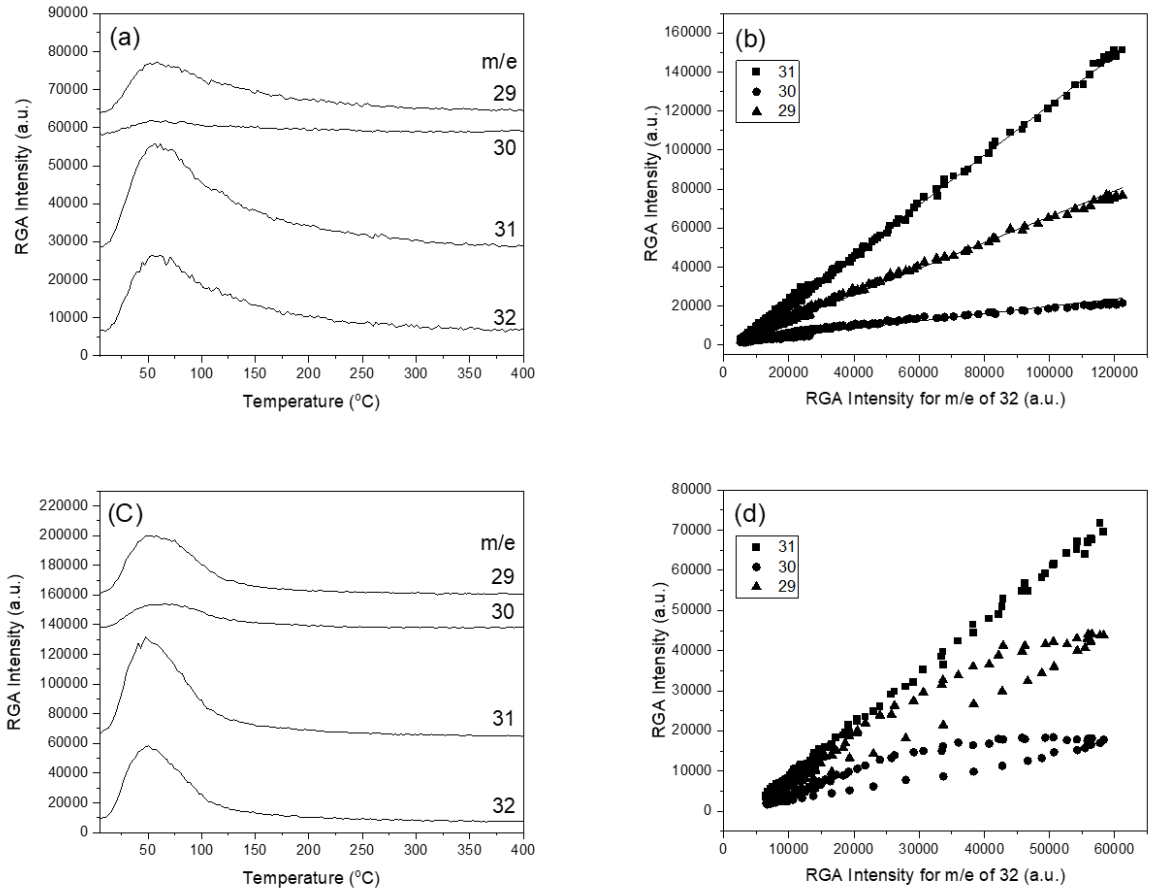

Figure 3.12 Methanol TPD raw data and linear fittings for m/e of 31, 30 and 29 to 32. (a) Methanol Cu_{100} TPD spectrum without fragmentation correction. (b) Linear fitting for m/e of 31, 30 and 29 to 32. (c) Methanol $(CuO)_{80}$ TPD spectrum without fragmentation correction. (d) Plotting for m/e of 31, 30 and 29 to 32.

A2. P/Cu ratio

Figure 3.13 shows the P/Cu ratios at all four temperatures for Cu_{100} and $(CuO)_{80}$. The relative sensitivity factors used for P 2p and Cu $2p_{3/2}$ are 0.486 and 3.547.[31] The P/Cu ratios

generally remain at around 0.1. Since there is no obvious decreasing in the P/Cu ratios, it is believed that the DMMP desorption below 100 °C is not from the clusters but from the sample holder.

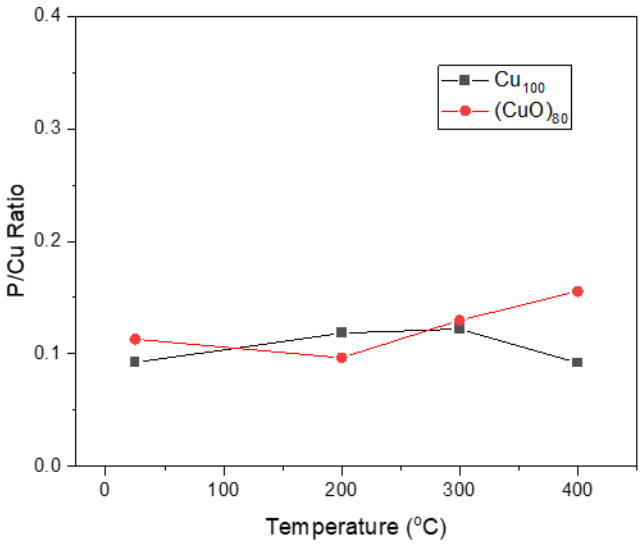

Figure 3.13 P/Cu ratio for Cu_{100} and $(CuO)_{80}$ at 25 °C, 200 °C, 300 °C, 400 °C.

4. Testing and Troubleshooting of the New Apparatus

Besides installing every component physically, testing and troubleshooting a newly constructed apparatus also take tremendous efforts. This section discusses a few major improvements and troubleshooting processes that have been made to bring the new apparatus to be fully functional.

4.1 Magnetron Sputtering Source Modification

A stable ion source which can generate the clusters of interest with high enough ion intensity is the first requirement for consistent and reliable clusters deposition experiments.

On the new apparatus, copper cooling coils have been added to the aggregation region of the magnetron sputtering source (Figure 4.1). VCO fittings have been used for easy uninstallation. With water cooling for each deposition process, the ion intensity, as well as the size distribution, seem to be more stable compared to without water cooling and using a stainless-steel aggregation column. Liquid nitrogen cooling was also tried for making zirconium oxide clusters; however, no significant changes were observed compared to water cooling. Nevertheless, it is still worth trying liquid nitrogen cooling with other systems. It should be noted that Teflon O-rings should be used for liquid nitrogen cooling, and they should be replaced every time after the cooling lines are uninstalled, otherwise they may start to leak during the cooling process.

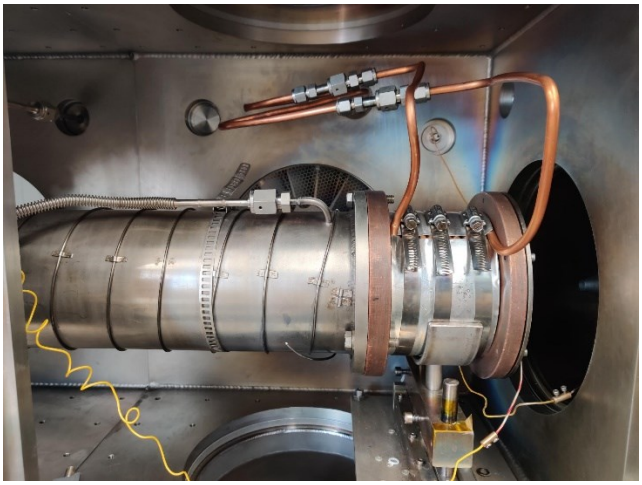

Figure 4.1 Aggregation region for magnetron sputtering source.

Another issue that has been fixed for the magnetron is the gas line. As is shown in Figure 4.2, the rigid gas line has been changed with flexible bellows tubing. Even though the U-shape of the rigid gas line has some degree of flexibility, it was not good enough for easy installation. Moreover, restricting the rigid tubing towards the center could easily cause the weld to break since it was the weakest part in the gas line.

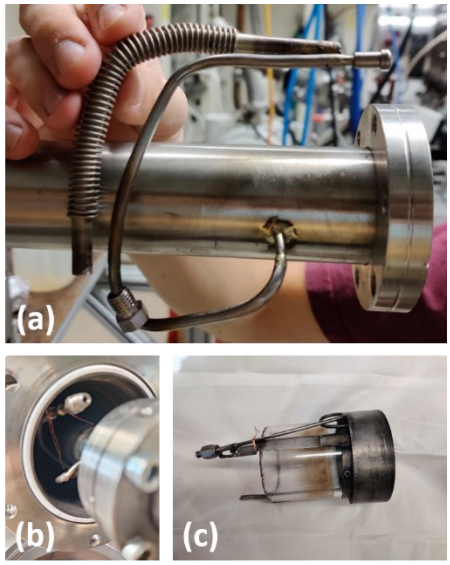

Figure 4.2 Magnetron source gas line. (a) Replacing the rigid U-shape gas line into flexible bellow tubing. (b) (c) Flexible tubing has been restricted towards the center to prevent rubbing again the housing wall during operation.

Once the cooling line and gas line problems have been fixed, the next important factor to ensure stable operation are the two sealing surfaces: one is between the copper aggregation region and the front plate, the other one is between the copper aggregation region and the back column. One may assume that the seals may not matter that much since the diameter of the iris is as large as 1-1.5 centimeter. However, they are very important to ensure high ion intensity and high signal stability. On the new apparatus, it is usually the case that the pressure in the inner source is 1.0-1.4 torr while the pressure in chamber 1 is 1.0×10^{-4} - 1.0×10^{-3} torr. If the pressure in chamber 1 is already close to 1.0×10^{-3} torr, while the inner source pressure is still below 1.0 torr, it is very likely that the two seals are not maintained very well. In this scenario, the two sealing surfaces need to be checked or the O-rings need to be replaced.

It is usually the case that the ion intensity for the clusters of interest drops significantly during the deposition period of a few hours. For a decent deposition process, the signal intensity

should still remain at least more than 50% of the starting point with almost no change in the source and only a few adjustments on the ion optics. This was rarely the case on the old apparatus; however, it has been achieved routinely on the new apparatus.

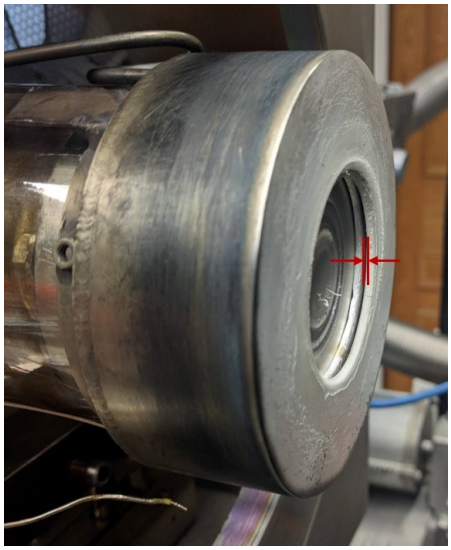

Figure 4.3 Gas column installed on the magnetron head with a limited and controlled distance of 0.5-1 mm.

Based on the experience on the old apparatus, it appeared to the author that the distance between the gas column and the target holder (Figure 4.3) is very important for stable and intense ion signal. For a typical deposition process on the old machine, the ion intensity often dropped to less than half of what it was at the beginning before enough clusters were deposited. Then, the source conditions and ion optics needed to be adjusted. Sometimes, the deposition needed to be paused, and the ion signal needed to be tuned up on the last few ion optics. There were also some days when the ion signal was stable, and the source conditions did not require any adjustment during the deposition. The author realized that the distance between the gas column and the target holder was maintained at a small distance for those good depositions, and the gas column became crooked or slipped away from the target holder during deposition for those bad depositions. This was the case because the U-shaped rigid gas line always carried some tension, and the three screws for the gas column sometimes did not have enough friction force to hold the gas column in place,

especially during operation when everything was heated up. On the new apparatus, after replacing the magnetron head with a stronger magnet, the slots on the gas column have also been precisely readjusted so that the largest distance is now controlled by the slots instead of relying on the frictions between the screws and the slots. In this case, the distance between the gas column and the target holder has now been controlled reliably at a small distance (0.5-1 mm) for every reassembly of the source as well as during every deposition process. The resistance between the gas column and the metal target is usually in the range of 0.5-5 MΩ if the gas column is installed right. As a result, the magnetron has been working much more consistently on the new apparatus.

A few parameters can be adjusted within the magnetron source such as the pressure of helium, argon, oxygen, sputtering current, sputtering voltage, and the aggregation distance. The sputtering current and voltage can be controlled by a programmable DC power supply (KEPCO KLN 600-1.25). The constant current mode has been proven to be better for stable ion intensity. Adjusting oxygen content under constant current mode can cause the sputtering voltage to change dramatically from 200-400V, therefore, it is recommended that one should adjust the oxygen in small amount and wait for a few minutes for the sputtering voltage to stabilize. If the ion intensity drops dramatically, the iris and the big skimmer voltages should be adjusted accordingly first. For the pressure of argon, it is usually related to the sputtering current and the material being sputtered. The optimized argon pressure is usually not dramatically different among different systems. For helium and aggregation distance, it is usually the case that larger clusters prefer higher helium pressure and longer aggregation distance.

It should be noted that the inner pressure range is more limited on the new apparatus (<1.5 torr) than what it was on the old apparatus (< 4 torr), due to the pressure limit in chamber 1 ($1x10^{-3}$ torr) since it is pumped primarily by a VHS-6 diffusion pump. This is the case because the multi-stage skimmers (Figure 1.3) for differential pumping have not been inherited onto the new apparatus. However, based on the experience on both the old and new apparatus, it is believed that

the pressure limit may be the main reason why larger clusters cannot be easily made on the new machine.

4.2 Laser Vaporization Sources

A laser vaporization disk sources was designed by Dr. Zachary Hicks by taking inspiration of another pioneering laser vaporization disk sources design[139] in Dr. Ulrich Heiz's lab. Similar in effect to Heiz's hypocycloidal gear setup, a planetary gear setup was applied so that the laser shot traces could cover the whole area of a 2 -inch-diameter target disk as is shown in Figure 4.4. More details are described in Dr. Hicks's thesis.[51]

Figure 4.4 Petaled rose curve laser ablation traces on zirconium target.

Even though the planetary gear system allows for a petaled rose curve ablation pattern on the disk target, the mechanical integrity of the gear system turns out to be not strong enough to press the target holder up against the front plate to create a seal. As is shown in Figure 4.5, some green light is leaking through from the upper side of the target holder, where there should also be a huge leak for helium and oxygen gases. During the rotating process, the leakage between the target holder and the front plate is constantly changing due to the uneven force from the square peg

pressed into one of the planet gears. As a result, the ion intensity is also changing dramatically. It should be noted that the ion intensity is always higher when there is no obvious green light leakage, therefore the seal is believed to be one of the most critical factors for the laser vaporization disk source to be working for cluster deposition experiments. Unfortunately, solving this problem by modifying the current design or redesigning the mechanical structures completely is beyond the author's experience and knowledge.

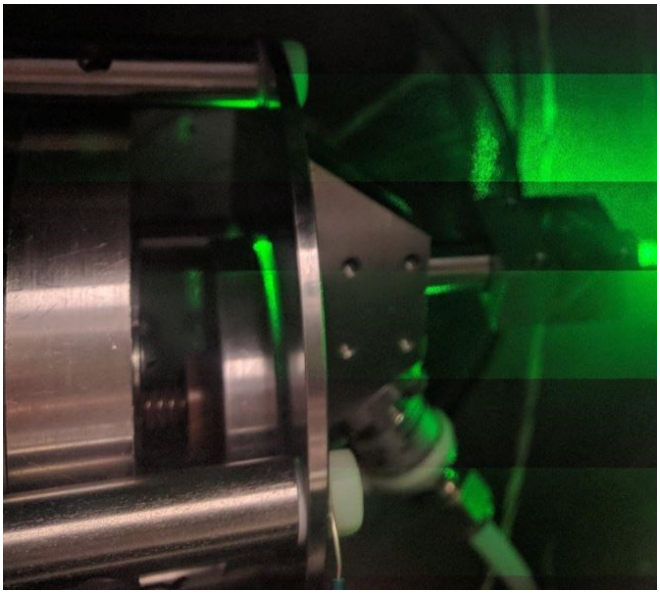

Figure 4.5 Laser vaporization disk source.

4.3 Tuning and measuring of the deposition ion signal

Besides stable cluster ion sources, an efficient beam line with high transmission and good stability is the next key factor for routine cluster deposition experiments. On the new apparatus, the clusters ions remain collimated in the xy-axis as they travel down the z-axis from aperture to aperture by one quadruple ion guide and multiple octupole ion guides. A 90° beam bender is placed before the QMS to filter out neutral clusters and ions of the undesired polarity. More details about the beam line are described elsewhere.[51]

In the early stage of tuning up the beam line, SIMION, which is an ion trajectory simulation software, can help provide approximate electrostatic voltage ranges that are needed to be applied on the first a few ion optics. An electrometer (Keithley 6514) is connected through a BNC cable to the feedthroughs for every ion optics (mostly ion guides) to measure the ion intensity while all the voltages applied before that ion optic are being tuned. It is usually very easy to get several nanoamps of ion current on the thin aperture 1 as long as the voltage polarities applied onto the quadrupole ion guide and the first octupole ion guide are right. The voltages for the iris and the big skimmer depend largely on the source conditions and how long the source has been running without cleaning out metal oxide deposit.

Table 2 Voltages for ion optics (the unit is V).

Ion Optics in Sequence	$Cu_xZr_yO_z^+$	$Cu_xZr_yO_z^-$	Pt $Nb_xO_y^-$
Iris	9	0	0
Big Skimmer	28	0	-24
Quadrupole	24	-2	-23
Small Skimmer	1	0	-20
Octupole	-122	24	30
Thin Aperture 1	-160	69	148
Bender Inlet Octupole	-62	56	109
Bender Aperture 1	-220	175	136
Bender Aperture 2	-276	278	306
Bender Aperture 3	10	93	306
Bender Aperture 4	10	93	306
Bender Rods 1, 3	-276	290	264
Bender Rods 2, 4	53	-48	-58

Bender Outlet Octupole	-45	39	69
Thin Gate Valve	-67	55	66

Once, several nanoamps of ion signal can be measured on the thin aperture 1, it is not necessary to stay on it for tuning up the ion intensity. Instead, it is recommended to move on to the thin gate valve. It should be noted that the thin gate valve is grounded when it is fully closed and is completely out of the way when it is fully open. Therefore, the thin gate valve should be halfway open while measuring ion signal on it. As is shown in Table 2, with one set of voltages for positive ions and two sets of voltages for negative ions, it is expected that the positive and negative cluster ions need the opposite polarity of voltages on the bender. The signal intensity is most sensitive to the voltages applied on bender rod 1, 3 and 2, 4; less sensitive to that on bender aperture 1, and 2; and least sensitive to that on bender aperture 3, and 4. More time can be devoted to tuning up the ion signal on the thin gate valve until the ion intensity reaches tens of nanoamps.

Once a set of voltages has been figured out, for example, the set of voltages for PtNbxOy- clusters shown in Table 2, for similar systems, such as PtMxOy- (M = Zr, Ti, and Mo), one should be able to turn on the beam line and immediately detect ion signal of decent intensity on the deposition octupole under unselected mode of the QMS. Then, a few mass spectra of different resolutions and ranges can be acquired in order to decide which clusters are to be mass selected. At last, all the voltage conditions and sources conditions should be fine-tuned to maximize the ion intensity for the selected size of clusters.

When there is no ion current at all, here are some troubleshooting steps to be followed: 1. Check if the electrometer is connected right (including the continuity across the RC filter box); 2. Check the source conditions, such as the pressures, sputtering current, and what the interior source region looks like when viewing down through the beam line via the laser inlet window (especially color and consistency); 3. Check all the DC voltages and verify the correct outputs are being applied;

4. Check the RF oscillator boxes. All the RF boxes are home-built based on the literature[140], the high voltage power supplies of which should usually output ~400V with 90-120 mA. When there is no current, it is usually the case that the capacitors C4 or C5 has blew out. C4 and C5 provide a low-impedance path for radio frequencies but block the plate dc voltage.[140] Typically a blown capacitor in an RF box will produce a subtle, but noticeable smell of burning plastic. The value of these capacitors is not critical, as long as they are equal and large compared to the capacity of the load. Therefore, C4 and C5 have to be replaced at the same time for repairment even through it is usually the case that only one of them blows out. When the current is higher than normal, it is usually the case that one of the alligator clips has detached from the potentiometer coils within the RF box. It should be easy to fix by repositioning the two alligator clips so that the same number of coils are connected into the circuit.

It should be noted that the tunability of voltages applied on all the ion optics are limited by the voltage that can be applied to float the QMS, due to the fact that the housing shield of the QMS has been designed to be grounded through flange mounting of the housing. The housing should had have been designed to mount in such a way that it is electrically isolated and can be floated. The float voltage of the QMS can be applied through the LabVIEW program by setting the value for Pole Bias from -5 to 5 scaled to -200 to 200 V.[51] When operating with quadrupole pole bias different from quadrupole housing potential of more than 10 V, sensitivity can diminish by more than an order of magnitude and peaks can split because the housing potential can assert itself into the quadrupole, which causes octupolar and dodecapolar non-linear resonances.[141] On the current apparatus, since the housing is grounded, the quadrupole pole bias should be set to within -10 to 10 V. In practice, the voltage range can be expanded to -15 to 15 V while the quality of the mass spectra is still maintained. If the housing of the QMS is modified to be electrically isolated and floated, the whole beam line will probably achieve better efficiency.

4.4 Fluorine Contamination

The fluorine contamination originated from the use of Apiezon 501 grease, which was applied on the three slide seal spring-energized Teflon O-rings due to a gross misconception that O-rings always need grease to create a better seal. However, Teflon is a self-lubricating material, which can create a transfer film on the mirror polished stainless steel rod.[142] In fact, the energized Teflon O-rings work better unlubricated, compared to when used with grease.

Apiezon 501 grease is advertised as a chemically inert, low vapor pressure (1.3×10^{-12} Torr at 25 ^{o}C), high temperature lubricant, that can be used in oxygen rich or UHV environments. However, the vapor pressure is as high as 10^{-5} Torr at 200 ^{o}C. What is worse is that the grease can break down into toxic and corrosive gases above 300 ^{o}C. Furthermore, it is not suitable for cryogenic applications. Lastly, the composition of Apiezon 501 is a mixture of perfluoropolyether (PFPE) and polytetrafluoroethylene (PTFE) which are susceptible to degradation by X-rays.[143-145] Unfortunately, in the surface analytical region of the new apparatus, where there are local high temperature regions and X-rays, Apiezon 501 grease was unavoidably decomposed into HF and other organofluoride species with higher vapor pressures.

When there was still a macroscopic level of grease in the chamber, the TPD results for DMMP decomposition were inconsistent and of very low signal intensity (data not shown here). The TPD experiments with and without clusters had almost similar peak intensity, which was very likely caused by the extensive fluorine contamination. After the macroscopic level of grease was cleaned out, the results of DMMP TPD experiments seemed to be more consistent but the signal intensity was still extremely low compared to the old apparatus. For example, Figure 4.6 shows two TPD spectra for DMMP decomposition on $ZrCu_{2\text{-}3}O_n$ clusters with a very week peak for all the products as compared to the results obtained on the old apparatus (Chapter 2, and Chapter 3).

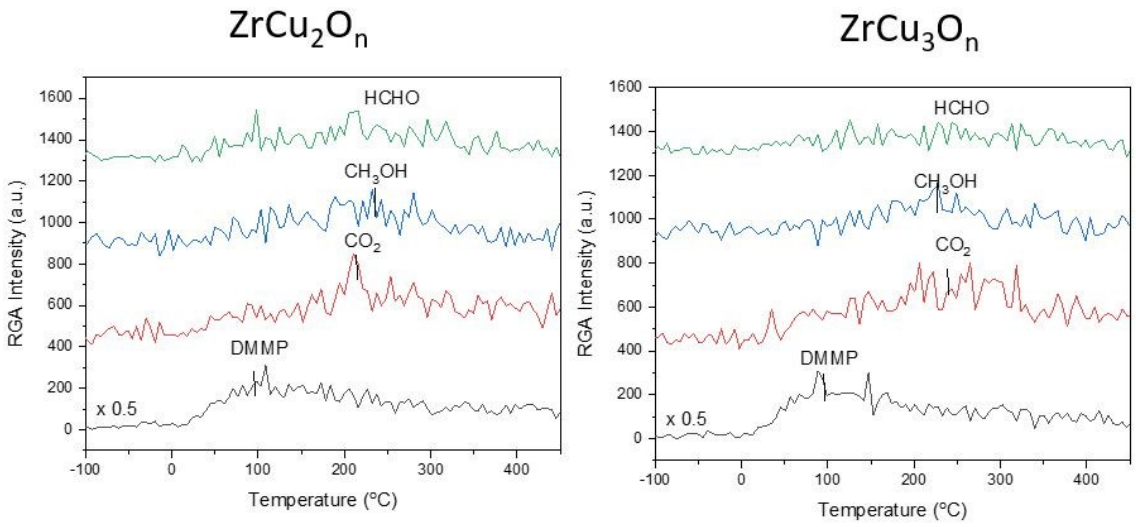

Figure 4.6 Figure 4.5 DMMP TPD results for $ZrCu_2O_n$ and $ZrCu_3O_n$.

The macroscopic level of grease was cleaned out by a high vapor pressure perfluorinated solvent followed by acetone. Then the fluorine contamination level was estimated via XPS and RGA. As is shown in Figure 4.7, freshly peeled HOPG could collect organofluoride species immediately after being transferred into the analysis chamber. After annealing to 400 ºC for 10 minutes, the F 1s signal intensity increased moderately.

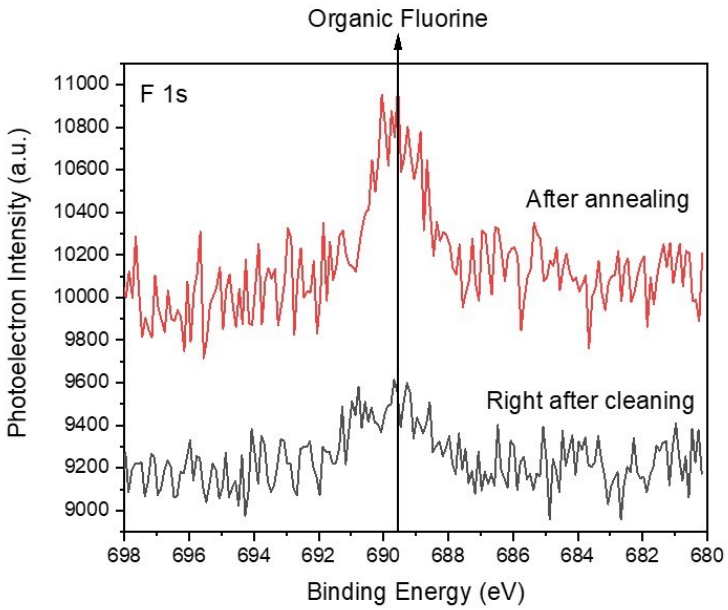

Figure 4.7 F 1s XPS for freshly peeled HOPG.

When 3×10^{13} $ZrCu_3O_{4\text{-}6}$ clusters were deposited onto the HOPG at room temperature, F 1s signal intensity increased significantly (Figure 4.8). After annealing to 400 ^{o}C for 10 minutes, F 1s shifted to higher binding energy indicating the organofluoride species could have decomposed or reacted with the clusters.

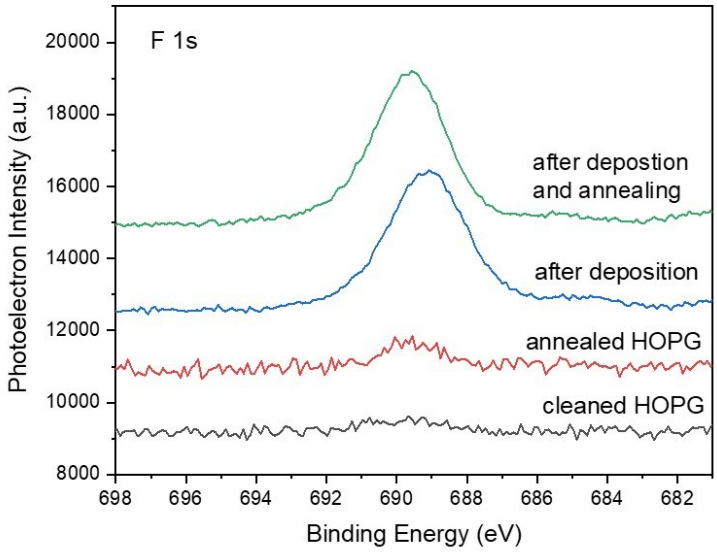

Figure 4.8 F 1s XPS for $ZrCu_3O_{4-6}$ supported on HOPG before and after annealing.

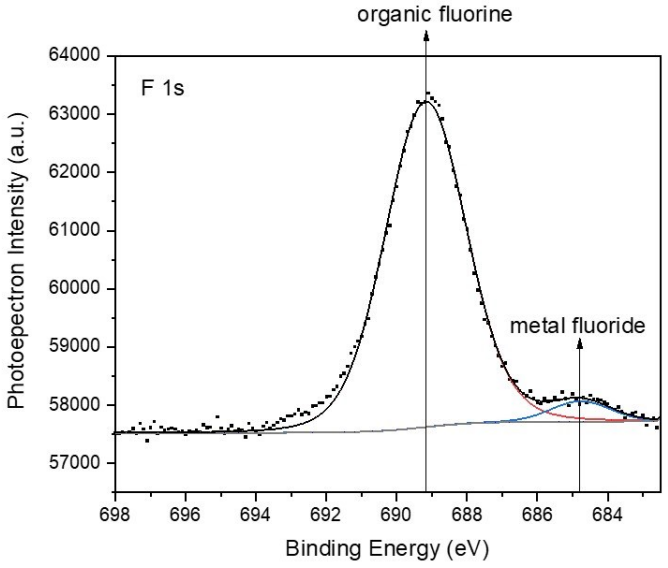

Figure 4.9 Peak fitting of F 1s XPS for freshly deposited $ZrCu_3O_{4-6}$ supported on HOPG.

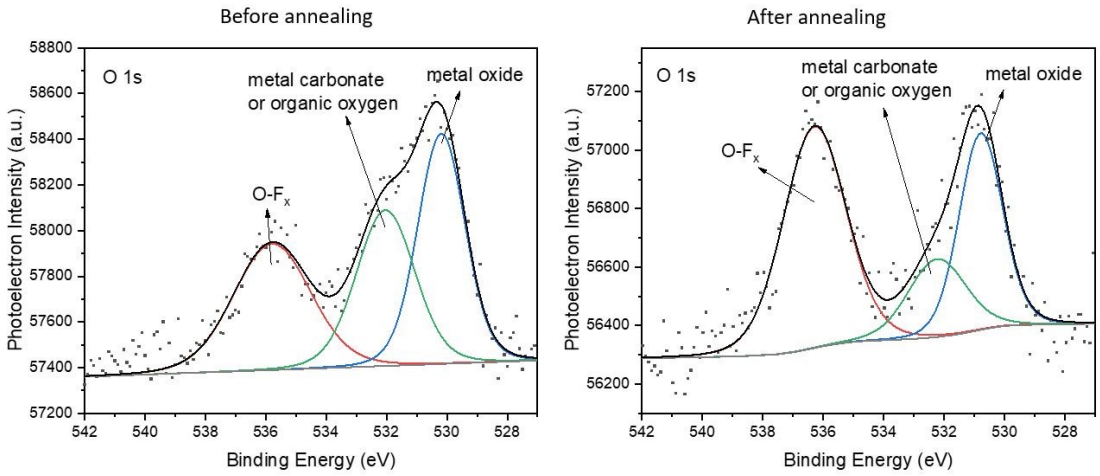

Figure 4.10 Peak fitting of O 1s XPS for ZrCu3O4-6 supported on HOPG before and after annealing.

Peak fitting for F 1s shows that metal fluoride was formed after cluster deposition at room temperature (Figure 4.9). Peak fitting for O 1s shows that fluorinated oxygen species increased significantly after annealing to 400 ^{o}C (Figure 4.10).

In order to remove residual fluorine contamination, prolonged baking at around 130 ^{o}C was applied. During the baking process, the RGA intensity for all the organofluoride species went up but not for m/z 19. m/z 19 is believed to be F^{+}, which might be mainly from HF (Figure 4.11).

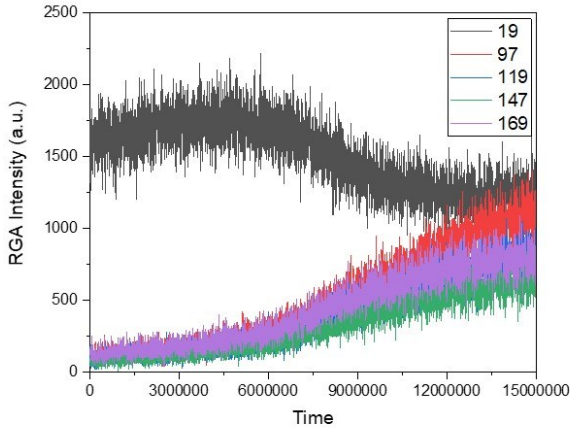

Figure 4.11 Prolong baking with RGA monitoring m/z 19 (F^{+}), 97 ($C_2F_3O^{+}$), 119 ($C_2F_5^{+}$), 147 ($C_3F_5O^{+}$), 169 ($C_3F_7^{+}$)

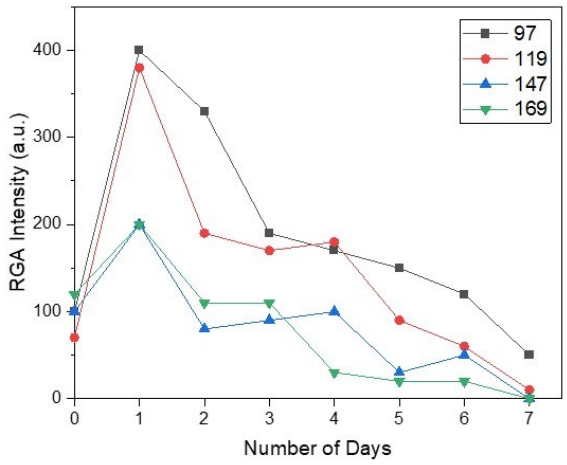

Figure 4.12 RGA intensities for organofluoride species.

Figure 4.12 shows that the RGA intensity for those organofluoride species increased significantly in the first day, dropped back down in the next two days, and gradually decreased to close to zero counts at the end. After a week of prolonged baking, it was believed that further baking could not provide considerable progress anymore.

Since baking was not very effective in cleaning out the X-ray source and fluorinated oligomers are X-ray sensitive, it was expected that more fluorine contamination species can be generated during the X-ray outgassing process.

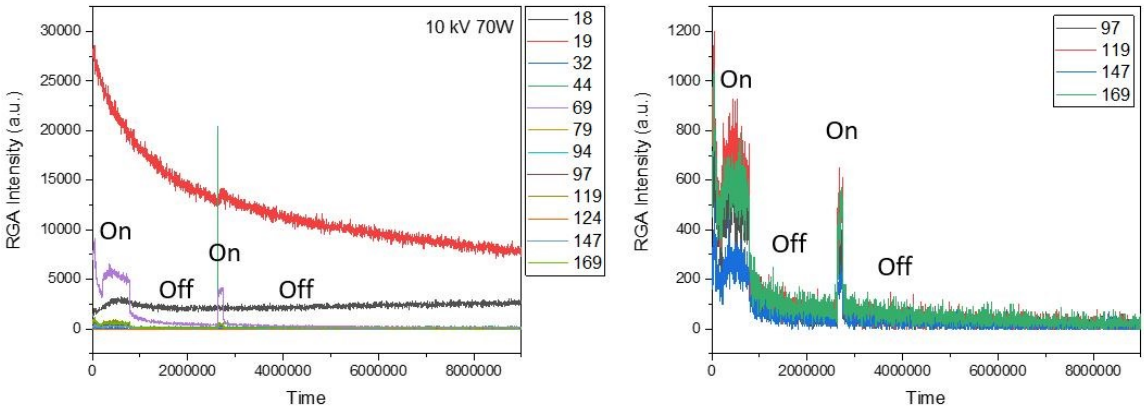

Figure 4.13 Degassing of the X-ray source at 10 kV 70W.

First, the filaments of the X-ray source were degassed from 3A up to 4.5A. Then, high voltage conditioning was applied to the anode from 10 kV to 15 kV. Finally, the power of the X-ray source was stepped up with the degassing pressure staying below 10^{-7} torr. As is shown in Figure 4.13 (left), degassing of the X-ray source to 10 kV and 70W caused m/z 19 and 69 to spike up. Figure 4.13 (right) shows that all the heavier organofluoride species went up when the X-ray source was on, and immediately went down then X-ray source was turned off.

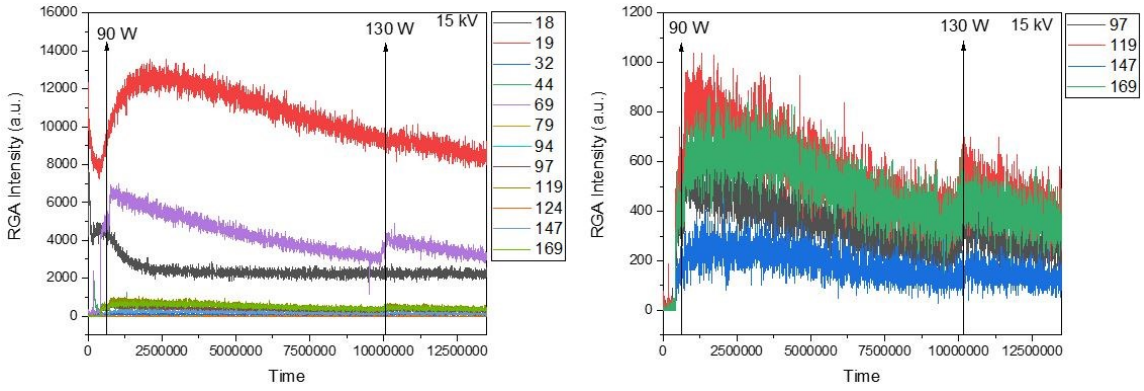

Figure 4.14 Degassing of the X-ray source from 15 kV 90W to 15 kV 130W.

X-ray Gun Degassing to 15 kV 90W and then 15 kV 130W caused m/z 19 and 69 to spike up and then slowly decrease as in shown in Figure 4.14 (left). The trend was the same for all the heavier organofluoride species as is shown in the zoomed in spectrum (Figure 4.14 right).

After the X-ray source was almost fully degassed, baking should be applied again to remove the fluorine contamination in the system. This time, hot Ar flushes were applied during baking. All three turbomolecular pumps for the UHV region were turned off, and 5-10 torr of Ar was dosed into the chamber via a leak valve with 60-70 psi of backing pressure. After 30 min, the chamber was pumped down by a scroll pump to low vacuum. This Ar flush process was repeated several times before the chamber was pumped down to UHV. Ar flushes were cycled with X-ray source degassing, RGA degassing and TSP cycles. All these efforts helped to lower the level of fluorine contamination even more.

To increase the collision energies between argon and the chamber wall, argon glow discharge was carried out. A glow discharge plasma is formed when the voltage applied on a low-pressure gas exceeds its breakdown voltage and causes its ionization.[146] Mild plasma cleaning of metal surfaces was shown to be effective in removing organic contaminants.[147-148]

In practice, a copper electrode was installed onto the copper lead on the sample holder, as is shown in Figure 4.15. The physics of argon glow discharge is similar to magnetron sputtering. The metal target in the magnetron source is like the chamber wall in the argon glow discharge cleaning process. Therefore, the power supply for the magnetron sputtering source was used for argon glow discharge. The positive voltage applied to the copper wire hanging in the center of the chamber was tuned up gradually until a purple plasma occured (Figure 4.16). The glow discharge was maintained with ~+300 V with a constant flow of Ar maintaining at about 6.5×10^{-2} Torr. The discharge current was stabilized at around 55 mA.

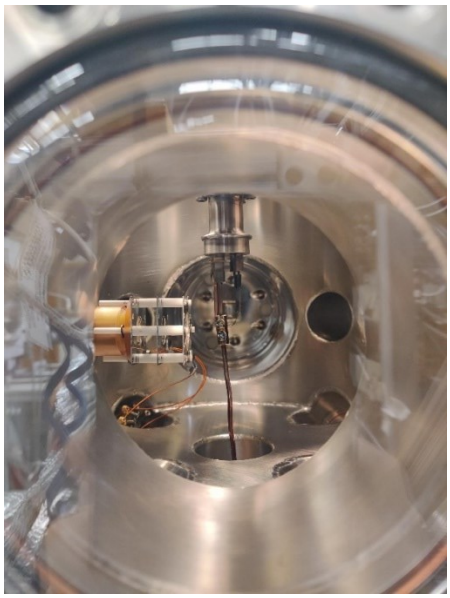

Figure 4.15 Copper electrode installed onto the copper lead on the sample holder.

Figure 4.16 Argon glow discharge plasma.

Argon glow discharge seemed to be a more effective way of removing organofluoride species from the system. After several sessions of argon glow discharge for a few hours followed by baking the whole system routinely as well as degassing the RGA, there was almost no organofluoride species being detected by the RGA except for a few thousands counts for m/z 19. However, after each baking cycle, the X-ray source needed to be degassed again, and a small amount of m/z 19 as well as organofluoride species were still outgassed by the X-ray source.

4.5 Methods to Make Heterometallic Oxide clusters

Interactions between metals and oxides are key factors to determine the performance of metal/oxide heterojunctions.[149] A systematic rationalization of the field is lacking due to the great diversity in catalysts, reactions and modification strategies.[150] Cluster deposition methods, through which the coverage and stoichiometry of the clusters are highly controllable, offer another route to study interactions between metals and oxides within the smallest unit with less than twenty atoms. In order to study heterometallic oxide clusters, a few strategies have been explored for making them in the magnetron sputtering source.

Half-Moon Sputtering Target

The most straightforward way to make mixed metal oxide clusters is to use half-round, semicircular targets for the two metals of interest. Figure 4.17 shows the copper molybdenum half-moon magnetron sputtering target, which were used to make $Mo_xCu_yO_z$ clusters. Since the half-round target is made from a full target, there is always a gap between the two pieces, a metal sheet should be placed behind the gap to avoid sputtering of the magnet cover. In this case, a copper or a molybdenum sheet should be placed behind the gap.

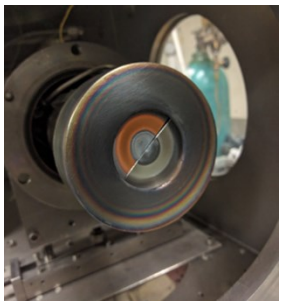

Figure 4.17 The copper molybdenum half-moon magnetron sputtering target.

Figure 4.18 shows a comparison between mass spectra (acquired on the old apparatus) for magnetron sputtering of a single molybdenum target and a copper molybdenum half-moon target. For $(MoO_3)_n^-$, for $n < 4$, each size of the molybdenum oxide clusters can be completely separated from each other. However, since copper has a smaller atomic mass and mixed metal oxide clusters have more complex compositions, the magnetic sector failed to completely resolve a certain size of clusters even for the smallest mixed metal oxide clusters ($CuMoO_4$).

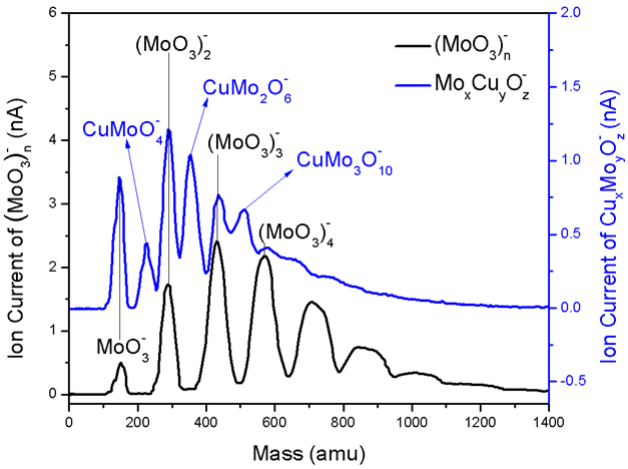

Figure 4.18 Mass spectra of magnetron sputtering single molybdenum target and copper molybdenum half-moon target.

Pressed Powder

A pressed powder method was tried for expensive metals such as gold. As is shown in Figure 4.19 right, sixteen 1.2 mm diameter holes were drilled along the trough of the sputtering racetrack on a niobium target. Those holes were press-filled with gold powder at 0.5-0.8 micron. The gold powder was greyish brown before being pressed. It turned a shiny gold color once press-filled into the holes on the niobium target.

Using this method can only generate very weak signal for $AuNb_yO_z^-$. The number of holes was doubled and then quadrupled, which still could not increase the absolute intensity for $AuNb_yO_z^-$ to be high enough for deposition experiments. At the biggening of the sputtering process, it was very likely that most of the gold powder got sputtered away very quickly. Therefore, the intensity for $AuNb_yO_z^-$ could not be maintained over a period of several hours.

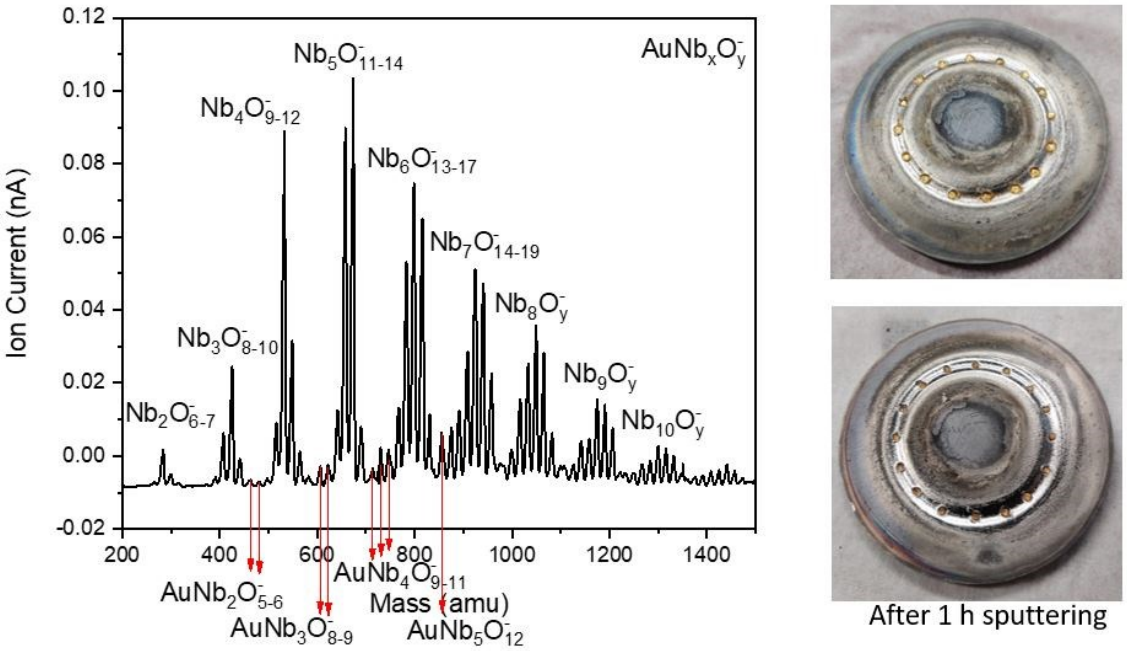

Figure 4.19 mass spectrum of $Au_xNb_yO_z^-$ and niobium target with 16 holes press-filled with gold powder.

Spot Welding of Metal Strips

The weldability for platinum with a lot of early transition metals such as Mo, Nb, Zr, Ti, V, Ta, and W is decent. Therefore, platinum strips were spot welded onto those metal sputtering targets (Figure 4.20) in order to make PtM_xO_y clusters.

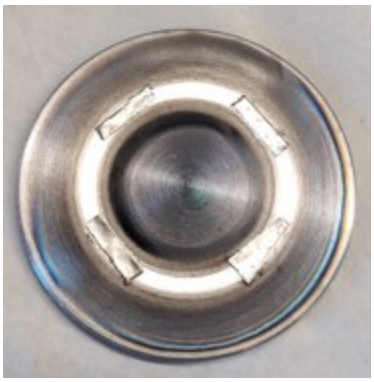

Figure 4.20 Zirconium target with 4 platinum stripes spot welded onto it.

While sputtering a metal (M) target spot welded with several platinum strips in the magnetron sputtering source, $M_xO_y^-$, $Pt_xO_y^-$, and $PtM_xO_y^-$ can be generated at the same time. In order to select pure heterometallic oxide clusters, it is desired that the peaks for $PtM_xO_y^-$ can sit between the peaks for $M_xO_y^-$. The transition metals in the fifth period such as Mo, Nb and Zr can fulfill this requirement.

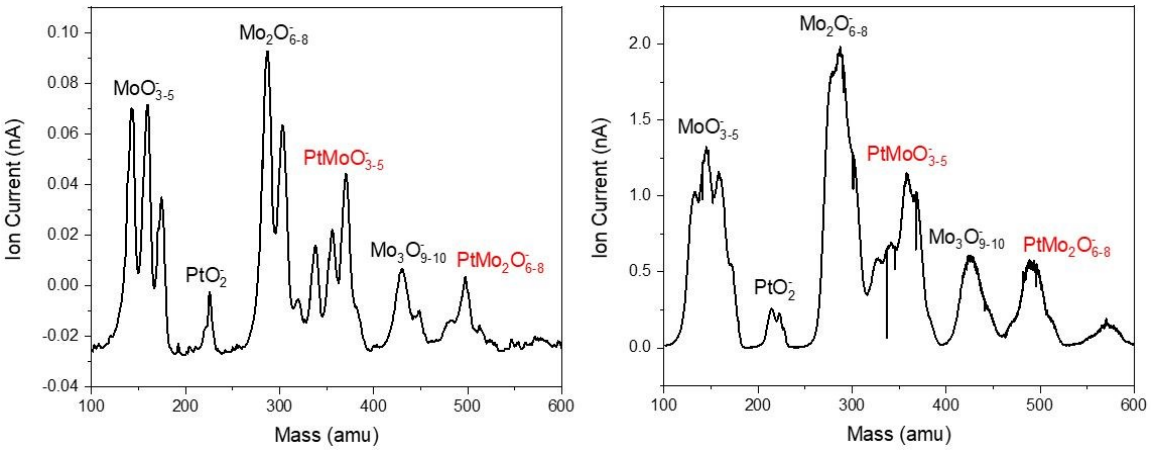

Figure 4.21 Mass spectra of $PtMo_xO_y^-$ under high resolution (left) and low resolution (right).

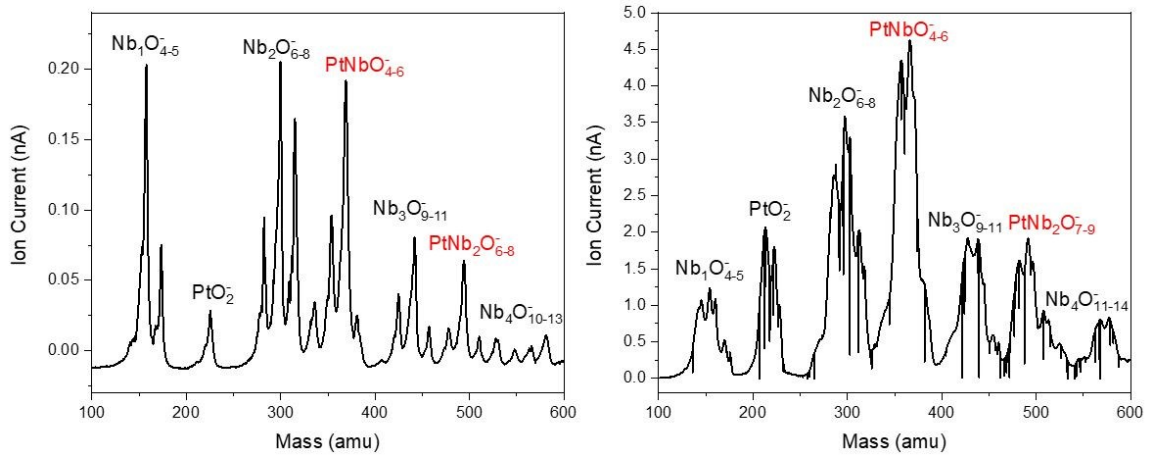

Figure 4.22 Mass spectra of $PtNb_xO_y^-$ under high resolution (left) and low resolution (right).

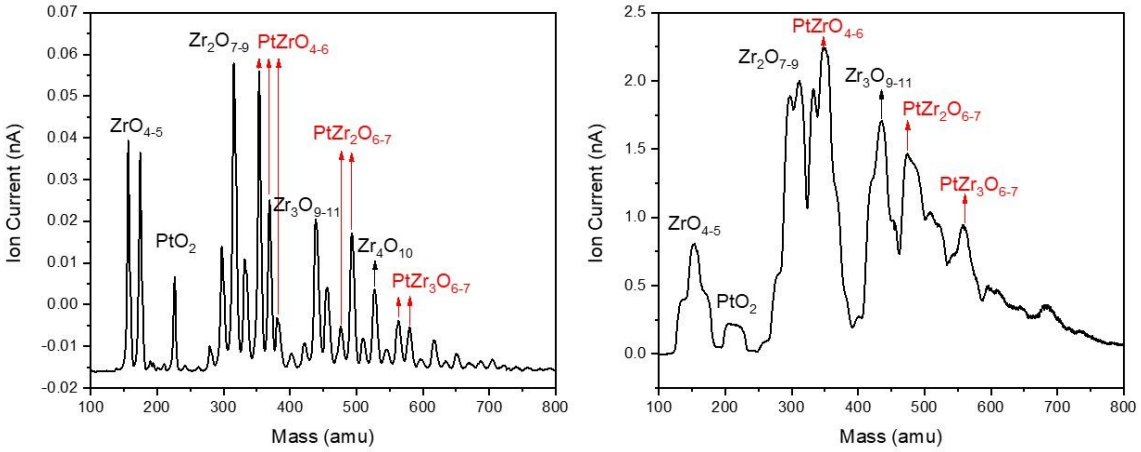

Figure 4.23 Mass spectra of $PtZr_xO_y^-$ under high resolution (left) and low resolution (right).

Figure 4.22, Figure 4.23, and Figure 4.23 show the mass spectra of $PtMo_xO_y^-$, $PtNb_xO_y^-$, and $PtZr_xO_y^-$, respectively. The spectra on the left are of high resolution when the number of oxygen atoms within the clusters are resolved. The spectra on the right are of low resolution with higher overall cluster ion intensity. Under mid-to-low resolution, $PtM_xO_y^-$ can be selected with known x value, two or three y values, and high enough ion intensity for deposition.

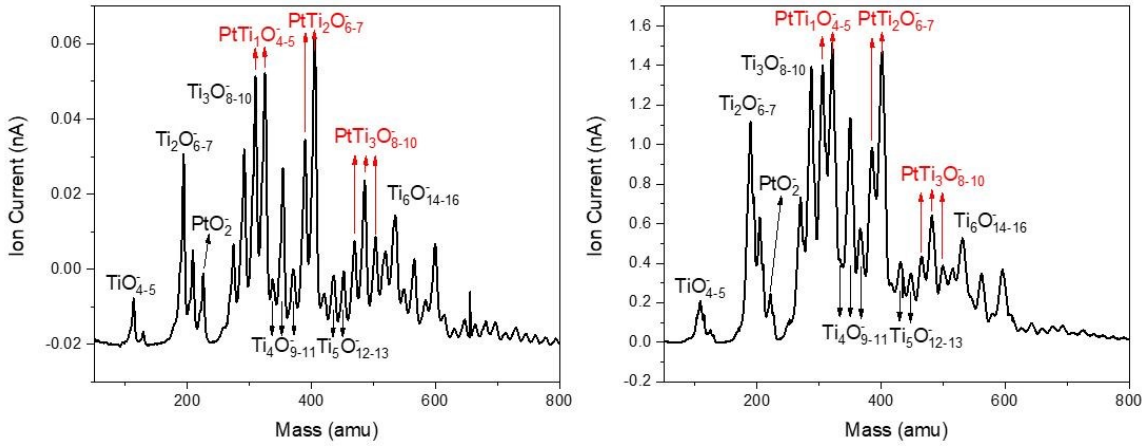

Figure 4.24 Mass spectra of $PtTi_xO_y^-$ under high resolution (left) and low resolution (right).

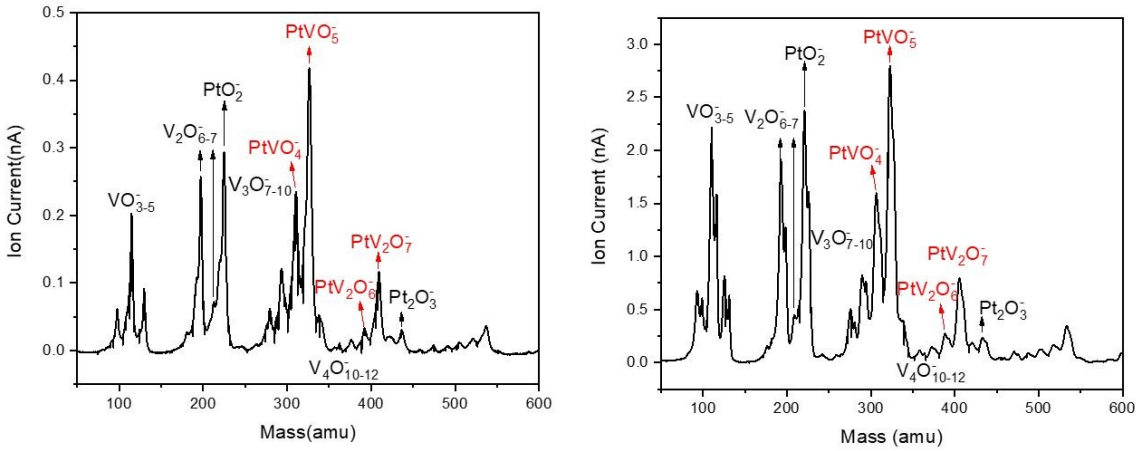

Figure 4.25 Mass spectra of $PtV_xO_y^-$ under high resolution (left) and low resolution (right).

For transition metals in the fourth period such as Ti and V, $PtM_xO_y^-$ have more overlaps with $M_xO_y^-$ in the mass spectra as is shown in Figure 4.25 and Figure 4.25. Both $PtTi_xO_y^-$ and $PtV_xO_y^-$ have decent cluster ion intensities under mid-to-low resolution. Therefore, $PtM_xO_y^-$ clusters mixed with a small amount of $M_xO_y^-$ clusters can be selected for deposition experiments.

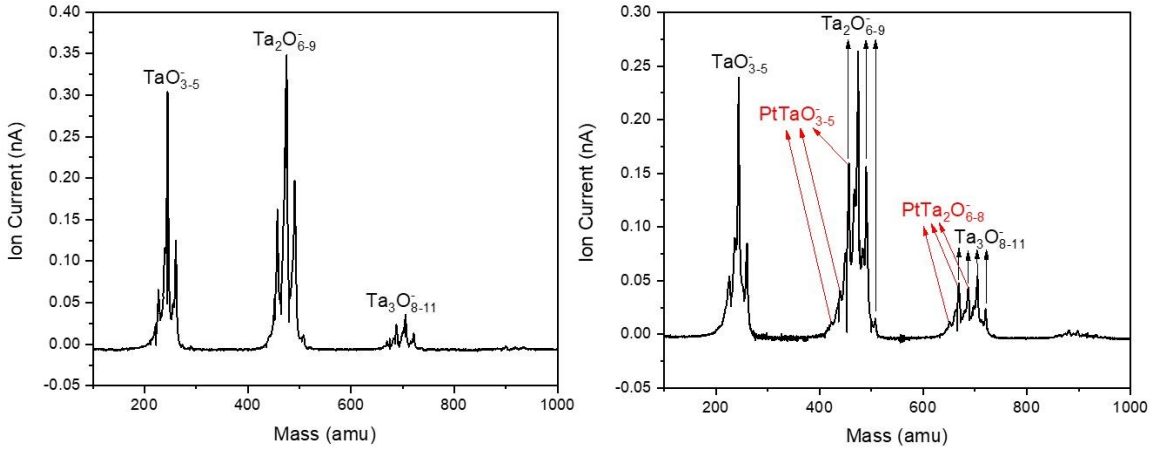

Figure 4.26 Mass spectra of $Ta_xO_y^-$ (left) and $PtTa_xO_y^-$ (right).

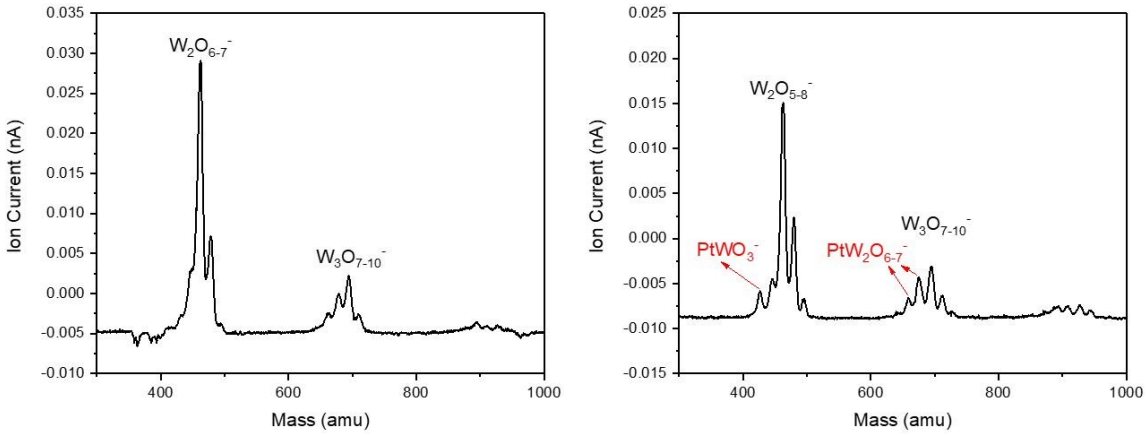

Figure 4.27 Mass spectra of $W_xO_y^-$ (left) and $PtW_xO_y^-$ (right).

For transition metals in the sixth period such as Ta and W, $PtM_xO_y^-$ are heavily overlapped with $M_xO_y^-$ in the mass spectra as is shown in Figure 4.27 and Figure 4.27. The mass spectrum for $PtM_xO_y^-$ needs to be compared to that for pure $M_xO_y^-$ in order to assign the peaks for $PtM_xO_y^-$. The clusters ion intensity for $PtM_xO_y^-$ is generally much lower than that for $M_xO_y^-$, thus making the deposition experiments for $PtTa_xO_y^-$ and $PtW_xO_y^-$ to be not very practical.

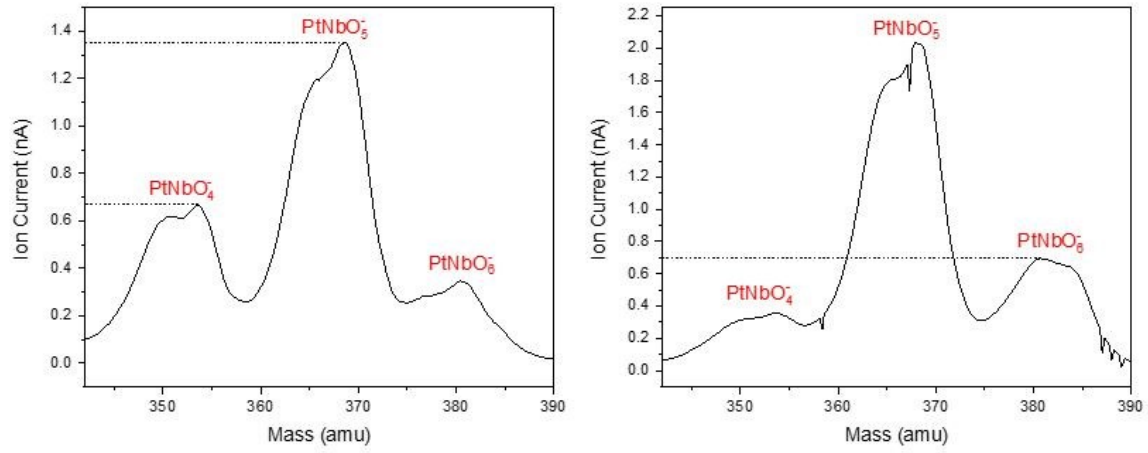

Figure 4.28 Mass spectra for $PtNbO_n^-$ (n=4, 5, and 6) with relatively lower (left) and higher (right) oxygen content in the magnetron sputtering source.

In short, Mo, Nb, Zr, Ti, and V are good candidates for M in PtM_xO_y clusters deposition experiments. Among those candidates, Nb stands out with superior cluster ion intensity for

$PtNb_xO_y^-$, so that the number of oxygens can be resolved for cluster deposition. By tuning the oxygen amount in the magnetron sputtering source, $PtNbO_n^-$ (n=4, 5, and 6) can be selected respectively with decent cluster ion intensities for deposition experiments. (Figure 4.28)

4.6 Preliminary results on the new apparatus: formic acid decomposition

4.6.1 Background of formic acid decomposition

Hydrogen, an environmentally friendly energy carrier, has been considered as one of the most promising candidates as the fuel for the future. There has been sustained interest in searching for a safe manner to transport and store hydrogen. Currently, using a proper chemical as the hydrogen carrier is one of those potential approaches.[151] Among all the hydrogen storage chemicals investigated recently, formic acid has drawn a lot of attention.[151-154]

There are two competing pathways for formic acid decomposition.[155-156] One is dehydration, which generates CO and H_2O; the other is dehydrogenation, which generates CO_2 and H_2. Apparently, the second pathway is desired for the production of H_2. For the first pathway, CO is not only toxic, but also can be poisonous for the catalysts, such as Pt and Pd. Therefore, developing an efficient catalyst that can preferentially decompose formic acid into CO_2 and H_2 is very crucial. There have been a lot of supported noble metal catalysts being explored for selective dehydrogenation of formic acid.[155, 157-159]

Formic acid decomposition has also been investigated under UHV conditions. Different single metal crystal surfaces serve as the model systems to unveil the adsorption and decomposition mechanism.[160-161] For Pd(111), formic acid was found to decompose into all four possible products, namely CO, CO_2, H_2 and H_2O.[160] A second element has also been introduced into the system by doping[162] or adding a substrate[163] for a Pd thin film to grow on, both of which have been used to achieve a higher selectivity for formic acid dehydrogenation. Very recently, Marcinkowski et.al.

conducted a comparison experiment on Pt-Cu single-atom alloy under UHV and solution phase environment.[30] They found that the Pt single atom is what makes the Pt-Cu single-atom alloy surface exhibit such high selectivity, however, this conclusion doesn't apply to the solution phase counterpart, which is a Pt-Cu single-atom alloy nanoparticle.[30] Even so, this work still indicates a great potential for developing better model systems for fundamental surface science studies on the catalytic properties of Pt single atom catalysts.

4.6.2 Experimental

HOPG was freshly peeled before transferred into the UHV chamber. It was then annealed at 500 ºC for 30 minutes. After that, it was cooled down to ~-175 ºC for clusters deposition. 4×10^{13} clusters were deposited for a typical TPD experiment. Several freeze-pump-thaw cycles with acetone dry ice bath was applied to formic acid (⩾95% Sigma-Aldrich) in order to degas it and pump away the residual water. Formic acid was dosed into the chamber at low 10^{-9} torr for 100 seconds. The dosing amount is monitored by RGA with m/z 46 at around 20000 counts. The sample was then heated to -50 ºC for 5 minutes to remove the physi-adsorbed formic acid. After the physisorption process, the sample was allowed to cool back down to cryogenic temperature. Finally, the sample was ramped up to 500 ºC at 1 ºC/s in front of the RGA to record a TPD spectrum.

4.6.3 Preliminary TPD results

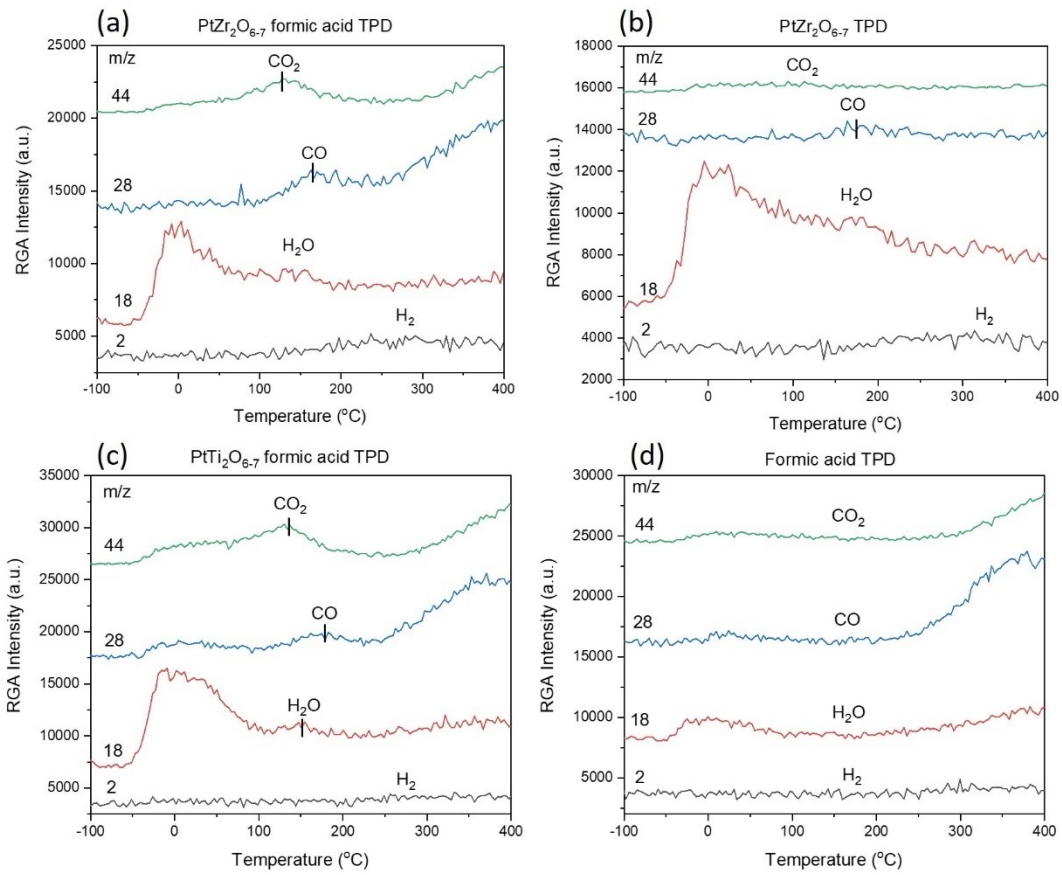

Figure 4.29 Formic acid TPD spectra: (a) $PtZr_2O_{6-7}$ formic acid TPD; (b) $PtZr_2O_{6-7}$ TPD without formic acid; (c) $PtTi_2O_{6-7}$ formic acid TPD; (d) formic acid TPD.

Figure 4.29 shows the TPD results of formic acid decomposition on size-selected clusters with their control experiment. By comparing Figure 4.29 (a) to (b), it is reasonable to conclude that the desorption of CO_2 and CO in temperature range of 100-200 ºC in Figure 4.29 (a) is mostly due to formic acid decomposition on $PtZr_2O_{6-7}$ clusters. By comparing Figure 4.29 (a) to (d), the rising background for CO2 and CO above 300 ºC are very likely due to the HOPG or the sample holder. Figure 4.29 (a) and (c) shows that $PtZr_2O_{6-7}$ and $PtTi_2O_{6-7}$ have similar peak positions for CO_2 and CO, indicating the metal oxide support for Pt single atom may not have much effect on the reaction.

It is not clear why no obvious H_2 desorption can be detected. Water desorption that is due to formic acid decomposition will required isotopic labeling experiments.

Formic acid TPD experiments have been repeated several times and the results are consistent, indicating the fluorine contamination should have much less effect on the results compared to the situation before the decontamination process.

References

1. Cox, D. M.; Eberhardt, W.; Fayet, P.; Fu, Z.; Kessler, B.; Sherwood, R. D.; Sondericker, D.; Kaldor, A., Electronic-Structure of Deposited Monosized Metal-Clusters. *Z Phys D Atom Mol Cl* **1991,** *20* (1-4), 385-386.

2. Roberts, F. S.; Kane, M. D.; Baxter, E. T.; Anderson, S. L., Oxygen activation and CO oxidation over size-selected Pt-n/alumina/Re(0001) model catalysts: correlations with valence electronic structure, physical structure, and binding sites. *Phys Chem Chem Phys* **2014,** *16* (48), 26443-26457.

3. von Weber, A.; Baxter, E. T.; Proch, S.; Kane, M. D.; Rosenfelder, M.; White, H. S.; Anderson, S. L., Size-dependent electronic structure controls activity for ethanol electro-oxidation at Pt-n/indium tin oxide (n=1 to 14). *Phys Chem Chem Phys* **2015,** *17* (27), 17601-17610.

4. Baxter, E. T.; Ha, M. A.; Cass, A. C.; Alexandrova, A. N.; Anderson, S. L., Ethylene Dehydrogenation on Pt-4,Pt-7,Pt-8 Clusters on Al2O3: Strong Cluster Size Dependence Linked to Preferred Catalyst Morphologies. *Acs Catalysis* **2017,** *7* (5), 3322-3335.

5. von Weber, A.; Baxter, E. T.; White, H. S.; Anderson, S. L., Cluster Size Controls Branching between Water and Hydrogen Peroxide Production in Electrochemical Oxygen Reduction at Pt-n/ITO. *J Phys Chem C* **2015,** *119* (20), 11160-11170.

6. Worz, A. S.; Judai, K.; Abbet, S.; Heiz, U., Cluster size-dependent mechanisms of the CO + NO reaction on small Pd-n (n <= 30) clusters on oxide surfaces. *J Am Chem Soc* **2003,** *125* (26), 7964-7970.

7. Kwon, G.; Ferguson, G. A.; Heard, C. J.; Tyo, E. C.; Yin, C. R.; DeBartolo, J.; Seifert, S.; Winans, R. E.; Kropf, A. J.; Greeley, J.; Johnston, R. L.; Curtiss, L. A.; Pellin, M. J.; Vajda, S., Size-Dependent Subnanometer Pd Cluster (Pd-4, Pd-6, and Pd-17) Water Oxidation Electrocatalysis. *Acs Nano* **2013,** *7* (7), 5808-5817.

8. Lee, S. S.; Fan, C. Y.; Wu, T. P.; Anderson, S. L., CO oxidation on Au-n/TiO2 catalysts produced by size-selected cluster deposition. *J Am Chem Soc* **2004,** *126* (18), 5682-5683.

9. Lee, S.; Molina, L. M.; Lopez, M. J.; Alonso, J. A.; Hammer, B.; Lee, B.; Seifert, S.; Winans, R. E.; Elam, J. W.; Pellin, M. J.; Vajda, S., Selective Propene Epoxidation on Immobilized Au6-10 Clusters: The Effect of Hydrogen and Water on Activity and Selectivity. *Angew Chem Int Edit* **2009,** *48* (8), 1467-1471.

10. Kaden, W. E.; Kunkel, W. A.; Kane, M. D.; Roberts, F. S.; Anderson, S. L., Size-Dependent Oxygen Activation Efficiency over Pd-n/TiO2(110) for the CO Oxidation Reaction. *J Am Chem Soc* **2010,** *132* (38), 13097-13099.

11. Bonanni, S.; Ait-Mansour, K.; Harbich, W.; Brune, H., Reaction-Induced Cluster Ripening and Initial Size-Dependent Reaction Rates for CO Oxidation on Pt-n/TiO2(110)-(1x1). *J Am Chem Soc* **2014,** *136* (24), 8702-8707.

12. Kane, M. D.; Roberts, F. S.; Anderson, S. L., Mass-selected supported cluster catalysts: Size effects on CO oxidation activity, electronic structure, and thermal stability of Pd-n/alumina (n <= 30) model catalysts. *Int J Mass Spectrom* **2014,** *370*, 1-15.

13. Tang, X.; Schneider, J.; Dollinger, A.; Luo, Y.; Worz, A. S.; Judai, K.; Abbet, S.; Kim, Y. D.; Gantefor, G. F.; Fairbrother, D. H.; Heiz, U.; Bowen, K. H.; Proch, S., Very small "window of opportunity" for generating CO oxidation-active Au-n on TiO2. *Phys Chem Chem Phys* **2014,** *16* (14), 6735-6742.

14. Kane, M. D.; Roberts, F. S.; Anderson, S. L., Effects of Alumina Thickness on CO Oxidation Activity over Pd-20/Alumina/Re(0001): Correlated Effects of Alumina Electronic Properties and Pd-20 Geometry on Activity. *J Phys Chem C* **2015,** *119* (3), 1359-1375.

15. Ha, M. A.; Baxter, E. T.; Cass, A. C.; Anderson, S. L.; Alexandrova, A. N., Boron Switch for Selectivity of Catalytic Dehydrogenation on Size Selected Pt Clusters on Al2O3. *J Am Chem Soc* **2017,** *139* (33), 11568-11575.

16. Liu, C.; Yang, B.; Tyo, E.; Seifert, S.; DeBartolo, J.; von Issendorff, B.; Zapol, P.; Vajda, S.; Curtiss, L. A., Carbon Dioxide Conversion to Methanol over Size-Selected Cu-4 Clusters at Low Pressures. *J Am Chem Soc* **2015,** *137* (27), 8676-8679.

17. Miller, J.; Siddiqui, H.; Gates, S.; Russell Jr, J.; Yates Jr, J.; Tully, J.; Cardillo, M., Extraction of kinetic parameters in temperature programmed desorption: A comparison of methods. *The Journal of chemical physics* **1987,** *87* (11), 6725-6732.

18. Falconer, J. L.; Schwarz, J. A., Temperature-programmed desorption and reaction: applications to supported catalysts. *Catalysis Reviews Science and Engineering* **1983,** *25* (2), 141-227.

19. Cvetanović, R.; Amenomiya, Y., Application of a temperature-programmed desorption technique to catalyst studies. In *Advances in Catalysis*, Elsevier: 1967; Vol. 17, pp 103-149.

20. Akhter, S.; White, J. M., A Static Sims Tpd Study of the Kinetics of Methoxy Formation and Decomposition on O/Pt(111). *Surf Sci* **1986,** *167* (1), 101-126.

21. Pan, Q.; Liu, B. H.; McBriarty, M. E.; Martynova, Y.; Groot, I. M. N.; Wang, S.; Bedzyk, M. J.; Shaikhutdinov, S.; Freund, H. J., Reactivity of Ultra-Thin ZnO Films Supported by Ag(111) and Cu(111): A Comparison to ZnO/Pt(111). *Catal Lett* **2014,** *144* (4), 648-655.

22. Zhou, X.; Shen, Q.; Yuan, K. D.; Yang, W. S.; Chen, Q. W.; Geng, Z. H.; Zhang, J. L.; Shao, X.; Chen, W.; Xu, G. Q.; Yang, X. M.; Wu, K., Unraveling Charge State of Supported Au Single-Atoms during CO Oxidation. *J Am Chem Soc* **2018,** *140* (2), 554-557.

23. Xi, M.; Bent, B. E., Iodobenzene on Cu(111) - Formation and Coupling of Adsorbed Phenyl Groups. *Surf Sci* **1992,** *278* (1-2), 19-32.

24. Wang, L. J.; Blando, N.; Hicks, Z.; Denchy, M.; Tang, X.; Bleuel, H.; Zhang, M. S.; Gantefor, G.; Bowen, K. H., Combined TPD and XPS Study of Ligation and Decomposition of 1,6-Hexanedithiol on Size-Selected Copper Clusters Supported on HOPG. *J Phys Chem C* **2018,** *122* (4), 2173-2183.

25. Xu, C.; Koel, B. E., Probing the Modifier Precursor State - Adsorption of Co on Sn/Pt(111) Surface Alloys. *Surf Sci* **1994,** *304* (3), L505-L511.

26. Iwamoto, M.; Yoda, Y.; Egashira, M.; Seiyama, T., Study of metal oxide catalysts by temperature programmed desorption. 1. Chemisorption of oxygen on nickel oxide. *The Journal of Physical Chemistry* **1976,** *80* (18), 1989-1994.

27. Kahler, K.; Holz, M. C.; Rohe, M.; Strunk, J.; Muhler, M., Probing the Reactivity of ZnO and Au/ZnO Nanoparticles by Methanol Adsorption: A TPD and DRIFTS Study. *Chemphyschem* **2010,** *11* (12), 2521-2529.

28. Badlani, M.; Wachs, I. E., Methanol: a "smart" chemical probe molecule. *Catal Lett* **2001,** *75* (3-4), 137-149.

29. Walenta, C. A.; Xu, F.; Tesvara, C.; O'Connor, C. R.; Sautet, P.; Friend, C. M., Facile Decomposition of Organophosphonates by Dual Lewis Sites on a Fe3O4(111) Film. *J Phys Chem C* **2020,** *124* (23), 12432-12441.

30. Marcinkowski, M. D.; Liu, J. L.; Murphy, C. J.; Liriano, M. L.; Wasio, N. A.; Lucci, F. R.; Flytzani-Stephanopoulos, M.; Sykes, E. C. H., Selective Formic Acid Dehydrogenation on Pt-Cu Single-Atom Alloys. *Acs Catalysis* **2017,** *7* (1), 413-420.

31. Moulder, J. F. S., W. F.; Sobol, P. E.; Bomben, K. D.;, Handbook of X-ray Photoelectron Spectroscopy, J. Chastain (Ed.) Perkin-Elmer Corporation, Eden Prairie, Minnesota,. **1992**.

32. Wu, Y. T.; Garfunkel, E.; Madey, T. E., Initial stages of Cu growth on ordered Al2O3 ultrathin films. *J Vac Sci Technol A* **1996,** *14* (3), 1662-1667.

33. Yang, D. Q.; Sacher, E., Initial- and final-state effects on metal cluster/substrate interactions, as determined by XPS: copper clusters on Dow Cyclotene and highly oriented pyrolytic graphite. *Appl Surf Sci* **2002,** *195* (1-4), 187-195.

34. Dinardo, S.; Lozzi, L.; Passacantando, M.; Picozzi, P.; Santucci, S.; Decrescenzi, M., Ups and Xps Studies of Cu Clusters on Graphite. *Surf Sci* **1994,** *307*, 922-926.

35. Spitzer, A.; Luth, H., An Xps Study of the Water-Adsorption on Cu(110). *Surf Sci* **1985,** *160* (2), 353-361.

36. Russell, J. N.; Gates, S. M.; Yates, J. T., Reaction of Methanol with Cu(111) and Cu(111) + O(Ads). *Surf Sci* **1985,** *163* (2-3), 516-540.

37. Mcintyre, N. S.; Cook, M. G., X-Ray Photoelectron Studies on Some Oxides and Hydroxides of Cobalt, Nickel, and Copper. *Anal Chem* **1975,** *47* (13), 2208-2213.

38. Biesinger, M. C.; Lau, L. W. M.; Gerson, A. R.; Smart, R. S. C., Resolving surface chemical states in XPS analysis of first row transition metals, oxides and hydroxides: Sc, Ti, V, Cu and Zn. *Appl Surf Sci* **2010,** *257* (3), 887-898.

39. Wang, L.; Denchy, M.; Blando, N.; Hansen, L.; Bilik, B.; Tang, X.; Hicks, Z.; Bowen, K. H., Thermal Decomposition of Dimethyl Methylphosphonate on Size-Selected Clusters: A Comparative Study between Copper Metal and Cupric Oxide Clusters. *The Journal of Physical Chemistry C* **2021,** *125* (21), 11348-11358.

40. Tang, X.; Hicks, Z.; Wang, L. J.; Gantefor, G.; Bowen, K. H.; Tsyshevsky, R.; Sun, J. W.; Kuklja, M. M., Adsorption and decomposition of dimethyl methylphosphonate on size-selected (MoO3)(3) clusters. *Phys Chem Chem Phys* **2018,** *20* (7), 4840-4850.

41. Vajda, S.; White, M. G., Catalysis Applications of Size-Selected Cluster Deposition. *Acs Catalysis* **2015,** *5* (12), 7152-7176.

42. Vajda, S.; Lee, S.; Sell, K.; Barke, I.; Kleibert, A.; von Oeynhausen, V.; Meiwes-Broer, K. H.; Rodriguez, A. F.; Elam, J. W.; Pellin, M. M.; Lee, B.; Seifert, S.; Winans, R. E., Combined

temperature-programmed reaction and in situ x-ray scattering studies of size-selected silver clusters under realistic reaction conditions in the epoxidation of propene. *J Chem Phys* **2009,** *131* (12).

43. Vajda, S.; Pellin, M. J.; Greeley, J. P.; Marshall, C. L.; Curtiss, L. A.; Ballentine, G. A.; Elam, J. W.; Catillon-Mucherie, S.; Redfern, P. C.; Mehmood, F.; Zapol, P., Subnanometre platinum clusters as highly active and selective catalysts for the oxidative dehydrogenation of propane. *Nature materials* **2009,** *8* (3), 213-216.

44. Ford, T. A., Matrix isolation infrared spectroscopy - Comparison of theory with experiment. *Can J Anal Sci Spect* **1998,** *43* (4), 113-121.

45. Kudoh, S.; Onoda, K.; Takayanagi, M.; Nakata, M., N2O clusters in a supersonic jet studied by matrix-isolation infrared spectroscopy and density functional theory calculation. *J Mol Struct* **2000,** *524*, 61-68.

46. Goldberg, N.; Almond, M. J.; Ogden, J. S.; Cannady, J. P.; Walsh, R.; Becerra, R., The gas-phase reactions Of SiCl4 and Si2Cl6 with CH3OH and C2H5OH: An investigation by mass spectrometry and matrix-isolation infrared spectroscopy. *Phys Chem Chem Phys* **2004,** *6* (13), 3264-3270.

47. Teng, Y. L.; Xu, Q., Reactions of Group 14 Metal Atoms with Acetylene: A Matrix Isolation Infrared Spectroscopic and Theoretical Study. *J Phys Chem A* **2009,** *113* (44), 12163-12170.

48. Teng, Y. L.; Xu, Q. A., Reactions of Yttrium and Scandium Atoms with Acetylene: A Matrix Isolation Infrared Spectroscopic and Theoretical Study. *J Phys Chem A* **2010,** *114* (34), 9069-9073.

49. Wang, G. J.; Zhuang, J.; Zhou, M. F., Matrix Isolation Infrared Spectroscopic and Theoretical Study of the Reactions of Tantalum Oxide Molecules with Methanol. *J Phys Chem A* **2011,** *115* (31), 8623-8629.

50. Li, Z. J.; Fang, Z. T.; Kelley, M. S.; Kay, B. D.; Rousseau, R.; Dohnalek, Z.; Dixon, D. A., Ethanol Conversion on Cyclic (MO3)(3) (M = Mo, W) Clusters. *J Phys Chem C* **2014,** *118* (9), 4869-4877.

51. Hicks, Z. A. Design and Construction of a Molecular Beamline for Cluster Catalysis Studies. Johns Hopkins University, 2019.

52. Bonanni, S.; Ait-Mansour, K.; Harbich, W.; Brune, H., Effect of the TiO2 Reduction State on the Catalytic CO Oxidation on Deposited Size-Selected Pt Clusters. *J Am Chem Soc* **2012,** *134* (7), 3445-3450.

53. Wang, B.; Yoon, B.; Konig, M.; Fukamori, Y.; Esch, F.; Heiz, U.; Landman, U., Size-Selected Monodisperse Nanoclusters on Supported Graphene: Bonding, Isomerism, and Mobility. *Nano Lett* **2012,** *12* (11), 5907-5912.

54. Lei, Y.; Mehmood, F.; Lee, S.; Greeley, J.; Lee, B.; Seifert, S.; Winans, R. E.; Elam, J. W.; Meyer, R. J.; Redfern, P. C.; Teschner, D.; Schlogl, R.; Pellin, M. J.; Curtiss, L. A.; Vajda, S., Increased silver activity for direct propylene epoxidation via subnanometer size effects. *Science* **2010,** *328* (5975), 224-8.

55. Molina, L. M.; Lee, S.; Sell, K.; Barcaro, G.; Fortunelli, A.; Lee, B.; Seifert, S.; Winans, R. E.; Elam, J. W.; Pellin, M. J.; Barke, I.; von Oeynhausen, V.; Lei, Y.; Meyer, R. J.; Alonso, J. A.; Rodriguez, A. F.; Kleibert, A.; Giorgio, S.; Henry, C. R.; Meiwes-Broer, K. H.; Vajda, S., Size-dependent selectivity and activity of silver nanoclusters in the partial oxidation of propylene to propylene oxide and acrolein: A joint experimental and theoretical study. *Catal Today* **2011,** *160* (1), 116-130.

56. Tong, X.; Benz, L.; Kemper, P.; Metiu, H.; Bowers, M. T.; Buratto, S. K., Intact size-selected Au-n clusters on a TiO2(110)-(1 x 1) surface at room temperature. *J Am Chem Soc* **2005,** *127* (39), 13516-13518.

57. Kiskinova, M.; Goodman, D. W., Modification of Chemisorption Properties by Electronegative Adatoms - H-2 and Co on Chlorided, Sulfided, and Phosphided Ni(100). *Surf Sci* **1981,** *108* (1), 64-76.

58. Moon, D. W.; Bernasek, S. L.; Lu, J. P.; Gland, J. L.; Dwyer, D. J., Activation of Carbon-Monoxide on Clean and Sulfur Modified Fe(100). *Surf Sci* **1987,** *184* (1-2), 90-108.

59. Kiskinova, M. P., Electronegative Additives and Poisoning in Catalysis. *Surf Sci Rep* **1988,** *8* (8), 359-402.

60. Sexton, B. A.; Nyberg, G. L., A Vibrational and Tds Study of Sulfur Adsorbates on Cu(100) - Evidence for Ch3s Species. *Surf Sci* **1986,** *165* (1), 251-267.

61. Mullins, D. R.; Lyman, P. F., Adsorption and Reaction of Methanethiol on W(001). *J Phys Chem-Us* **1993,** *97* (36), 9226-9232.

62. Mullins, D. R.; Lyman, P. F., Adsorption and reaction of methanethiol on ruthenium(0001). *The Journal of Physical Chemistry* **1993,** *97* (46), 12008-12013.

63. Donev, S.; Brack, N.; Paris, N. J.; Pigram, P. J.; Singh, N. K.; Usher, B. F., Surface reactions of 1-propanethiol on GaAs(100). *Langmuir* **2005,** *21* (5), 1866-1874.

64. Kariapper, M. S.; Grom, G. F.; Jackson, G. J.; McConville, C. F.; Woodruff, D. P., Characterization of thiolate species formation on Cu(111) using soft x-ray photoelectron spectroscopy. *J Phys-Condens Mat* **1998,** *10* (39), 8661-8670.

65. Lai, Y. H.; Yeh, C. T.; Cheng, S. H.; Liao, P.; Hung, W. H., Adsorption and thermal decomposition of alkanethiols on Cu(110). *J Phys Chem B* **2002,** *106* (21), 5438-5446.

66. Carley, A. F.; Davies, P. R.; Jones, R. V.; Harikumar, K. R.; Roberts, M. W.; Welsby, C. J., A combined XPS/STM and TPD study of the chemisorption and reactions of methyl mercaptan at a Cu(110) surface. *Top Catal* **2003,** *22* (3-4), 161-172.

67. Prince, N. P.; Seymour, D. L.; Woodruff, D. P.; Jones, R. G.; Walter, W., The Structure of Mercaptide on Cu(111) - a Case of Molecular Adsorbate-Induced Substrate Reconstruction. *Surf Sci* **1989,** *215* (3), 566-576.

68. Anderson, S. E.; Nyberg, G. L., Ups of Thiols and Disulfides Adsorbed on Cu(410) - Ch3sh, C2h5sh, C3h7sh, (Ch3s)2, (C2h5s)2, (C3h7s)2. *J Electron Spectrosc* **1990,** *52*, 735-746.

69. Rieley, H.; Kendall, G. K.; Chan, A.; Jones, R. G.; Ludecke, J.; Woodruff, D. P.; Cowie, B. C. C., Surface adsorption structures in 1-octanethiol self-assembled on Cu(111). *Surf Sci* **1997,** *392* (1-3), 143-152.

70. Mott, D.; Yin, J.; Engelhard, M.; Loukrakpam, R.; Chang, P.; Miller, G.; Bae, I. T.; Das, N. C.; Wang, C. M.; Luo, J.; Zhong, C. J., From Ultrafine Thiolate-Capped Copper Nanoclusters toward Copper Sulfide Nanodiscs: A Thermally Activated Evolution Route. *Chem Mater* **2010,** *22* (1), 261-271.

71. Her, J.; Cho, D.; Lee, C. S., Synthesis of Conductive Nano Ink Using 1-Octanethiol Coated Copper Nano Powders in 1-Octanol for Low Temperature Sintering Process. *Mater Trans* **2013,** *54* (4), 599-602.

72. Huertos, M. A.; Cano, I.; Bandeira, N. A. G.; Benet-Buchholz, J.; Bo, C.; van Leeuwen, P. W. N. M., Phosphinothiolates as Ligands for Polyhydrido Copper Nanoclusters. *Chem-Eur J* **2014,** *20* (49), 16121-16127.

73. Dong, T. Y.; Wu, H. H.; Lin, M. C., Superlattice of octanethiol-protected copper nanoparticles. *Langmuir* **2006,** *22* (16), 6754-6756.

74. Wang, Y. W.; Im, J. S.; Soares, J. W.; Steeves, D. M.; Whitten, J. E., Thiol Adsorption on and Reduction of Copper Oxide Particles and Surfaces. *Langmuir* **2016,** *32* (16), 3848-3857.

75. Barnes, A. J., Molecular-Complexes of the Hydrogen Halides Studied by Matrix-Isolation Infrared-Spectroscopy. *J Mol Struct* **1983,** *100* (Jul), 259-280.

76. Tsao, M. L.; Zhu, Z. D.; Platz, M. S., Matrix and time-resolved infrared spectroscopy of chloro-p-nitrophenylcarbene and related species. *J Phys Chem A* **2001,** *105* (37), 8413-8416.

77. Gong, Y.; Andrews, L.; Chen, M. Y.; Dixon, D. A., Reactions of Late Lanthanide Metal Atoms and Methanol in Solid Argon: A Matrix Isolation Infrared Spectroscopic and Theoretical Study. *J Phys Chem A* **2011,** *115* (51), 14581-14592.

78. Zhao, Y. Y., C-Cl Activation by Group IV Metal Oxides in Solid Argon Matrixes: Matrix Isolation Infrared Spectroscopy and Theoretical Investigations of the Reactions of MOx (M = Ti, Zr; x=1, 2) with CH3Cl. *J Phys Chem A* **2013,** *117* (27), 5664-5674.

79. Tang, X.; Li, X.; Wang, Y.; Wepasnick, K.; Lim, A.; Fairbrother, D. H.; Bowen, K. H.; Mangler, T.; Noessner, S.; Wolke, C.; Grossmann, M.; Koop, A.; Gantefoer, G.; Kiran, B.; Kandalam, A. K., Size Selected Clusters on Surfaces. *J Phys Conf Ser* **2013,** *438*.

80. Smith, K. L.; Black, K. M., Characterization of the Treated Surfaces of Silicon Alloyed Pyrolytic Carbon and Sic. *J Vac Sci Technol A* **1984,** *2* (2), 744-747.

81. Muller, T.; Flynn, G. W.; Mathauser, A. T.; Teplyakov, A. V., Temperature-programmed desorption studies of n-alkane derivatives on graphite: Desorption energetics and the influence of functional groups on adsorbate self-assembly. *Langmuir* **2003,** *19* (7), 2812-2821.

82. Tang, X.; Bumueller, D.; Lim, A.; Schneider, J.; Heiz, U.; Gantefor, G.; Fairbrother, D. H.; Bowen, K. H., Catalytic Dehydration of 2-Propanol by Size-Selected (WO3) and (MoO3)(n) Metal Oxide Clusters. *J Phys Chem C* **2014,** *118* (50), 29278-29286.

83. Doronin, M.; Bertin, M.; Michaut, X.; Philippe, L.; Fillion, J. H., Adsorption energies and prefactor determination for CH3OH adsorption on graphite. *J Chem Phys* **2015,** *143* (8).

84. Arce, F. T.; Vela, M. E.; Salvarezza, R. C.; Arvia, A. J., Comparative study of thiol films on C(0001) and Au(111) surfaces by scanning probe microscopy. *Surf Rev Lett* **1997,** *4* (4), 637-649.

85. Floro, J. A.; Chason, E.; Cammarata, R. C.; Srolovitz, D. J., Physical origins of intrinsic stresses in Volmer-Weber thin films. *Mrs Bull* **2002,** *27* (1), 19-25.

86. Kwon, S.; Russell, J.; Zhao, X. C.; Vidic, R. D.; Johnson, J. K.; Borguet, E., Combined experimental and theoretical investigation of polar organic adsorption/desorption from model carbonaceous surfaces: Acetone on graphite. *Langmuir* **2002,** *18* (7), 2595-2600.

87. Lee, S. Y.; Mettlach, N.; Nguyen, N.; Sun, Y. M.; White, J. M., Copper oxide reduction through vacuum annealing. *Appl Surf Sci* **2003,** *206* (1-4), 102-109.

88. Alemozafar, A. R.; Guo, X. C.; Madix, R. J., Adsorption and reaction of sulfur dioxide with Cu(110) and Cu(110)-p(2x1)-O. *J Chem Phys* **2002,** *116* (11), 4698-4706.

89. Dugan, N.; Erkoc, S., Structural properties of copper nanoparticles: Modified diffusion Monte Carlo simulations. *Int J Mod Phys C* **2006,** *17* (8), 1171-1177.

90. McGrath, J. W.; Chin, J. P.; Quinn, J. P., Organophosphonates revealed: new insights into the microbial metabolism of ancient molecules. *Nat Rev Microbiol* **2013,** *11* (6), 412-419.

91. Kim, K.; Tsay, O. G.; Atwood, D. A.; Churchill, D. G., Destruction and Detection of Chemical Warfare Agents. *Chem Rev* **2011,** *111* (9), 5345-5403.

92. Li, Y. X.; Klabunde, K. J., Nanoscale Metal-Oxide Particles as Chemical Reagents - Destructive Adsorption of a Chemical-Agent Simulant, Dimethyl Methylphosphonate, on Heat-Treated Magnesium-Oxide. *Langmuir* **1991,** *7* (7), 1388-1393.

93. Ekerdt, J. G.; Klabunde, K. J.; Shapley, J. R.; White, J. M.; Yates, J. T., Surface-Chemistry of Organo-Phosphorus Compounds. *J Phys Chem-Us* **1988,** *92* (22), 6182-6188.

94. Henych, J.; Janos, P.; Kormunda, M.; Tolasz, J.; Stengl, V., Reactive adsorption of toxic organophosphates parathion methyl and DMMP on nanostructured Ti/Ce oxides and their composites. *Arab J Chem* **2019,** *12* (8), 4258-4269.

95. Jaiswal, M.; Chauhan, D.; Sankararamakrishnan, N., Copper chitosan nanocomposite: synthesis, characterization, and application in removal of organophosphorous pesticide from agricultural runoff. *Environ Sci Pollut R* **2012,** *19* (6), 2055-2062.

96. Kaur, P.; Bansal, P.; Sud, D., Heterostructured Nanophotocatalysts for Degradation of Organophosphate Pesticides from Aqueous Streams. *J Korean Chem Soc* **2013,** *57* (3), 382-388.

97. Rani, M.; Shanker, U., Degradation of traditional and new emerging pesticides in water by nanomaterials: recent trends and future recommendations. *Int J Environ Sci Te* **2018,** *15* (6), 1347-1380.

98. Mitchell, M. B.; Sheinker, V. N.; Mintz, E. A., Adsorption and decomposition of dimethyl methylphosphonate on metal oxides. *J Phys Chem B* **1997,** *101* (51), 11192-11203.

99. Bermudez, V. M., Effect of Humidity on the Interaction of Dimethyl Methylphosphonate (DMMP) Vapor with SiO2 and Al2O3 Surfaces, Studied Using Infrared Attenuated Total Reflection Spectroscopy. *Langmuir* **2010,** *26* (23), 18144-18154.

100. Templeton, M. K.; Weinberg, W. H., Decomposition of Phosphonate Esters Adsorbed on Aluminum-Oxide. *J Am Chem Soc* **1985,** *107* (4), 774-779.

101. Sheinker, V. N.; Mitchell, M. B., Quantitative study of the decomposition of dimethyl methylphosphonate (DMMP) on metal oxides at room temperature and above. *Chem Mater* **2002,** *14* (3), 1257-1268.

102. Wilmsmeyer, A. R.; Uzarski, J.; Barrie, P. J.; Morris, J. R., Interactions and Binding Energies of Dimethyl Methylphosphonate and Dimethyl Chlorophosphate with Amorphous Silica. *Langmuir* **2012,** *28* (30), 10962-10967.

103. Kanan, S. M.; Tripp, C. P., An infrared study of adsorbed organophosphonates on silica: A prefiltering strategy for the detection of nerve agents on metal oxide sensors. *Langmuir* **2001,** *17* (7), 2213-2218.

104. Taylor, D. E.; Runge, K.; Cory, M. G.; Burns, D. S.; Vasey, J. L.; Hearn, J. D.; Griffith, K.; Henley, M. V., Surface Binding of Organophosphates on Silica: Comparing Experiment and Theory. *J Phys Chem C* **2013,** *117* (6), 2699-2708.

105. Aurianblajeni, B.; Boucher, M. M., Interaction of Dimethyl Methylphosphonate with Metal-Oxides. *Langmuir* **1989,** *5* (1), 170-174.

106. Moss, J. A.; Szczepankiewicz, S. H.; Park, E.; Hoffmann, M. R., Adsorption and photodegradation of dimethyl methylphosphonate vapor at TiO2 surfaces. *J Phys Chem B* **2005,** *109* (42), 19779-19785.

107. Trubitsyn, D. A.; Vorontsov, A. V., Experimental study of dimethyl methylphosphonate decomposition over anatase TiO2. *J Phys Chem B* **2005,** *109* (46), 21884-21892.

108. Kim, C. S.; Lad, R. J.; Tripp, C. P., Interaction of organophosphorous compounds with TiO2 and WO3 surfaces probed by vibrational spectroscopy. *Sensor Actuat B-Chem* **2001,** *76* (1-3), 442-448.

109. Rusu, C. N.; Yates, J. T., Photooxidation of dimethyl methylphosphonate on TiO2 powder. *J Phys Chem B* **2000,** *104* (51), 12299-12305.

110. Panayotov, D. A.; Morris, J. R., Uptake of a Chemical Warfare Agent Simulant (DMMP) on TiO2: Reactive Adsorption and Active Site Poisoning. *Langmuir* **2009,** *25* (6), 3652-3658.

111. Panayotov, D. A.; Morris, J. R., Thermal Decomposition of a Chemical Warfare Agent Simulant (DMMP) on TiO2: Adsorbate Reactions with Lattice Oxygen as Studied by Infrared Spectroscopy. *J Phys Chem C* **2009,** *113* (35), 15684-15691.

112. Rusu, C. N.; Yates, J. T., Adsorption and decomposition of dimethyl methylphosphonate on TiO2. *J Phys Chem B* **2000,** *104* (51), 12292-12298.

113. Mitchell, M. B.; Sheinker, V. N.; Tesfamichael, A. B.; Gatimu, E. N.; Nunley, M., Decomposition of dimethyl methylphosphonate (DMMP) on supported cerium and iron co-impregnated oxides at room temperature. *J Phys Chem B* **2003,** *107* (2), 580-586.

114. Mitchell, M. B.; Sheinker, V. N.; Cox, W. W.; Gatimu, E. N.; Tesfamichael, A. B., The room temperature decomposition mechanism of dimethyl methylphosphonate (DMMP) on alumina-supported cerium oxide - Participation of nano-sized cerium oxide domains. *J Phys Chem B* **2004,** *108* (5), 1634-1645.

115. Chen, D. A.; Ratliff, J. S.; Hu, X. F.; Gordon, W. O.; Senanayake, S. D.; Mullins, D. R., Dimethyl methylphosphonate decomposition on fully oxidized and partially reduced ceria thin films. *Surf Sci* **2010,** *604* (5-6), 574-587.

116. Tang, X.; Hicks, Z.; Gantefor, G.; Eichhorn, B. W.; Bowen, K. H., Adsorption and Decomposition of DMMP on Size-Selected (WO3)(3) Clusters. *Chemistryselect* **2018,** *3* (13), 3718-3721.

117. Head, A. R.; Tsyshevsky, R.; Trotochaud, L.; Yu, Y.; Karslioglu, O.; Eichhorn, B.; Kuklja, M. M.; Bluhm, H., Dimethyl methylphosphonate adsorption and decomposition on MoO2 as studied by ambient pressure x-ray photoelectron spectroscopy and DFT calculations. *J Phys-Condens Mat* **2018,** *30* (13).

118. Head, A. R.; Tsyshevsky, R.; Trotochaud, L.; Yu, Y.; Kyhl, L.; Karslioglu, O.; Kuklja, M. M.; Bluhm, H., Adsorption of Dimethyl Methylphosphonate on MoO3: The Role of Oxygen Vacancies. *J Phys Chem C* **2016,** *120* (51), 29077-29088.

119. Head, A. R.; Tang, X.; Hicks, Z.; Wang, L. J.; Bleuel, H.; Holdren, S.; Trotochaud, L.; Yu, Y.; Kyhl, L.; Karslioglu, O.; Fears, K.; Owrutsky, J.; Zachariah, M.; Bowen, K. H.; Bluhm, H., Thermal desorption of dimethyl methylphosphonate from MoO3. *Catal Struct React* **2017,** *3* (1-2), 112-118.

120. Trotochaud, L.; Tsyshevsky, R.; Holdren, S.; Fears, K.; Head, A. R.; Yu, Y.; Karslioglu, O.; Pletincx, S.; Eichhorn, B.; Owrutsky, J.; Long, J.; Zachariah, M.; Kuklja, M. M.; Bluhm, H., Spectroscopic and Computational Investigation of Room-Temperature Decomposition of a Chemical Warfare Agent Simulant on Polycrystalline Cupric Oxide. *Chem Mater* **2017,** *29* (17), 7483-7496.

121. Trotochaud, L.; Head, A. R.; Buchner, C.; Yu, Y.; Karslioglu, O.; Tsyshevsky, R.; Holdren, S.; Eichhorn, B.; Kuklja, M. M.; Bluhm, H., Room temperature decomposition of dimethyl methylphosphonate on cuprous oxide yields atomic phosphorus. *Surf Sci* **2019,** *680*, 75-87.

122. Guo, X.; Yoshinobu, J.; Yates, J. T., Decomposition of an Organophosphonate Compound (Dimethyl Methylphosphonate) on the Ni(111) and Pd(111) Surfaces. *J Phys Chem-Us* **1990,** *94* (17), 6839-6842.

123. Henderson, M. A.; White, J. M., Adsorption and Decomposition of Dimethyl Methylphosphonate on Platinum(111). *J Am Chem Soc* **1988,** *110* (21), 6939-6947.

124. Hegde, R. I.; Greenlief, C. M.; White, J. M., Surface-Chemistry of Dimethyl Methylphosphonate on Rh(100). *J Phys Chem-Us* **1985,** *89* (13), 2886-2891.

125. Smentkowski, V. S.; Hagans, P.; Yates, J., J T, Study of the catalytic destruction of dimethyl methylphosphonate: oxidation over Mo(110). *J. Phys. Chem.; (United States)* **1988**, Medium: X; Size: Pages: 6351-6357.

126. Ma, S.; Zhou, J.; Kang, Y. C.; Reddic, J. E.; Chen, D. A., Dimethyl methylphosphonate decomposition on Cu surfaces: Supported Cu nanoclusters and films on TiO2(110). *Langmuir* **2004,** *20* (22), 9686-9694.

127. McEntee, M.; Gordon, W. O.; Balboa, A.; Delia, D. J.; Pitman, C. L.; Pennington, A. M.; Rolison, D. R.; Pietron, J. J.; DeSario, P. A., Mesoporous Copper Nanoparticle/TiO2 Aerogels for Room-Temperature Hydrolytic Decomposition of the Chemical Warfare Simulant Dimethyl Methylphosphonate. *ACS Applied Nano Materials* **2020,** *3* (4), 3503-3512.

128. Estradeszwarckopf, H.; Rousseau, B.; Jupille, J., Cesium Surface Atoms - Xps Comparison between Gic Surfaces and Thin-Layers Deposited on Graphite. *Mater Sci Forum* **1992**, 703-708.

129. Lai, Y. H.; Yeh, C. T.; Lin, H. J.; Chen, C. T.; Hung, W. H., Thermal reaction of trimethylphosphine and triethylphosphine on Cu(110). *J Phys Chem B* **2002,** *106* (7), 1722-1727.

130. Gu, Z.; Hohn, K. L., Catalytic oxidation of methanol on nanoscale copper oxide and nickel oxide. *Ind Eng Chem Res* **2004,** *43* (1), 30-35.

131. Zhou, L.; Gunther, S.; Moszynski, D.; Imbihl, R., Reactivity of oxidized copper surfaces in methanol oxidation. *J Catal* **2005,** *235* (2), 359-367.

132. Zhou, J.; Ma, S.; Kang, Y. C.; Chen, D. A., Dimethyl methylphosphonate decomposition on titania-supported Ni clusters and films: A comparison of chemical activity on different ni surfaces. *J Phys Chem B* **2004,** *108* (31), 11633-11644.

133. Ratliff, J. S.; Tenney, S. A.; Hu, X. F.; Conner, S. F.; Ma, S. G.; Chen, D. A., Decomposition of Dimethyl Methylphosphonate on Pt, Au, and Au-Pt Clusters Supported on. TiO2(110). *Langmuir* **2009,** *25* (1), 216-225.

134. Ryberg, R., The Oxidation of Methanol on Cu(100). *J Chem Phys* **1985,** *82* (1), 567-573.

135. Ammon, C.; Bayer, A.; Held, G.; Richter, B.; Schmidt, T.; Steinruck, H. P., Dissociation and oxidation of methanol on Cu(110). *Surf Sci* **2002,** *507*, 845-850.

136. Sakong, S.; Sendner, C.; Gross, A., Partial oxidation of methanol on Cu(110): Energetics and kinetics. *J Mol Struc-Theochem* **2006,** *771* (1-3), 117-122.

137. Zandkarimi, B.; Alexandrova, A. N., Surface-supported cluster catalysis: Ensembles of metastable states run the show. *Wires Comput Mol Sci* **2019,** *9* (6).

138. Zhang, Z. S.; Zandkarimi, B.; Alexandrova, A. N., Ensembles of Metastable States Govern Heterogeneous Catalysis on Dynamic Interfaces. *Accounts Chem Res* **2020,** *53* (2), 447-458.

139. Heiz, U.; Vanolli, F.; Trento, L.; Schneider, W. D., Chemical reactivity of size-selected supported clusters: An experimental setup. *Rev Sci Instrum* **1997,** *68* (5), 1986-1994.

140. Jones, R. M.; Anderson, S. L., Simplified radio-frequency generator for driving ion guides, traps, and other capacitive loads. *Rev Sci Instrum* **2000,** *71* (11), 4335-4337.

141. Pedder, R.; Schaeffer, R., Optimizing Quadrupole Performance When Coupled With High Voltage Ion Sources. *LOTUS INTERNATIONAL* **1996**, 1154-1154.

142. Harris, K. L.; Pitenis, A. A.; Sawyer, W. G.; Krick, B. A.; Blackman, G. S.; Kasprzak, D. J.; Junk, C. P., PTFE Tribology and the Role of Mechanochemistry in the Development of Protective Surface Films. *Macromolecules* **2015,** *48* (11), 3739-3745.

143. Milintchouk, A.; VanEesbeek, M.; Levadou, F.; Harper, T., Influence of X-ray solar flare radiation on degradation of Teflon(R) in space. *J Spacecraft Rockets* **1997,** *34* (4), 542-548.

144. Jones Jr, W. R., Properties of perfluoropolyethers for space applications. *Tribology transactions* **1995,** *38* (3), 557-564.

145. Yoshihara, K.; Tanaka, A., Interlaboratory study on the degradation of poly(vinyl chloride), nitrocellulose and poly(tetrafluoroethylene) by x-rays in XPS. *Surf Interface Anal* **2002,** *33* (3), 252-258.

146. Li, Z.; Aik Khor, K., Preparation and Properties of Coatings and Thin Films on Metal Implants. In *Encyclopedia of Biomedical Engineering*, Narayan, R., Ed. Elsevier: Oxford, 2019; pp 203-212.

147. Okane, D. F.; Mittal, K. L., Plasma Cleaning of Metal-Surfaces. *J Vac Sci Technol* **1974,** *11* (3), 567-569.

148. Baker, M. A., Plasma Cleaning and the Removal of Carbon from Metal-Surfaces. *Thin Solid Films* **1980,** *69* (3), 359-368.

149. Fu, Q.; Wagner, T., Interaction of nanostructured metal overlayers with oxide surfaces. *Surf Sci Rep* **2007,** *62* (11), 431-498.

150. van Deelen, T. W.; Mejia, C. H.; de Jong, K. P., Control of metal-support interactions in heterogeneous catalysts to enhance activity and selectivity. *Nat Catal* **2019,** *2* (11), 955-970.

151. Zhu, Q. L.; Xu, Q., Liquid organic and inorganic chemical hydrides for high-capacity hydrogen storage. *Energ Environ Sci* **2015,** *8* (2), 478-512.

152. Enthaler, S.; von Langermann, J.; Schmidt, T., Carbon dioxide and formic acid-the couple for environmental-friendly hydrogen storage? *Energ Environ Sci* **2010,** *3* (9), 1207-1217.

153. Grasemann, M.; Laurenczy, G., Formic acid as a hydrogen source - recent developments and future trends. *Energ Environ Sci* **2012,** *5* (8), 8171-8181.

154. Loges, B.; Boddien, A.; Gartner, F.; Junge, H.; Beller, M., Catalytic Generation of Hydrogen from Formic acid and its Derivatives: Useful Hydrogen Storage Materials. *Top Catal* **2010,** *53* (13-14), 902-914.

155. Bi, Q. Y.; Du, X. L.; Liu, Y. M.; Cao, Y.; He, H. Y.; Fan, K. N., Efficient Subnanometric Gold-Catalyzed Hydrogen Generation via Formic Acid Decomposition under Ambient Conditions. *J Am Chem Soc* **2012,** *134* (21), 8926-8933.

156. Boddien, A.; Junge, H., CATALYSIS Acidic ideas for hydrogen storage. *Nat Nanotechnol* **2011,** *6* (5), 265-266.

157. Solymosi, F.; Koos, A.; Liliom, N.; Ugrai, I., Production of CO-free H-2 from formic acid. A comparative study of the catalytic behavior of Pt metals on a carbon support. *J Catal* **2011,** *279* (1), 213-219.

158. Yi, N.; Saltsburg, H.; Flytzani-Stephanopoulos, M., Hydrogen Production by Dehydrogenation of Formic Acid on Atomically Dispersed Gold on Ceria. *Chemsuschem* **2013,** *6* (5), 816-819.

159. Czaun, M.; Goeppert, A.; May, R.; Haiges, R.; Prakash, G. K. S.; Olah, G. A., Hydrogen Generation from Formic Acid Decomposition by Ruthenium Carbonyl Complexes. Tetraruthenium Dodecacarbonyl Tetrahydride as an Active Intermediate. *Chemsuschem* **2011,** *4* (9), 1241-1248.

160. Aas, N.; Li, Y. X.; Bowker, M., The Adsorption and Decomposition of Formic-Acid on Clean and Oxygen-Dosed Pd(110). *J Phys-Condens Mat* **1991,** *3*, S281-S286.

161. Bowker, M.; Madix, R. J., Xps, Ups and Thermal-Desorption Studies of the Reactions of Formaldehyde and Formic-Acid with the Cu(110) Surface. *Surf Sci* **1981,** *102* (2-3), 542-565.

162. Jeroro, E.; Vohs, J. M., Reaction of Formic Acid on Zn-Modified Pd(111). *Catal Lett* **2009,** *130* (3-4), 271-277.

163. Xu, C.; Goodman, D. W., Adsorption and reaction of formic acid on a pseudomorphic palladium monolayer on Mo(110). *J Phys Chem-Us* **1996,** *100* (1), 245-252.